PhD-FSTM-2025-016

The Faculty of Science, Technology and Medicine

DISSERTATION

Defence held on 14/01/2025 in Luxembourg

to obtain the degree of

DOCTEUR DE L'UNIVERSITE DU LUXEMBOURG
EN INFORMATIQUE

by

Michael Ninma DAZHI
Born on 14 July 1984 in Idah, Nigeria

MODELING, OPTIMIZATION AND RECONFIGURATION OF HYBRID SATELLITE NETWORKS FOR INTEGRATED SERVICE DELIVERY

Dissertation defense committee

Dr. Bhavani Shankar, Dissertation Supervisor
Assistant Professor, University of Luxembourg

Dr. Miguel Angel Olivarez Mendez, Chairman
Associate Professor, University of Luxembourg

Dr. Symeon Chatzinotas, Vice Chairman
Professor, University of Luxembourg

Dr. Muhammad Imran, Member
Professor, University of Glasgow

Dr. Joel Grotz, Member
Senior Manager, SES S.A., Luxembourg

Modeling, Optimization and Reconfiguration of Hybrid Satellite Networks for Integrated Service Delivery

Michael Ninma DAZHI

Abstract

This dissertation examines integrated service delivery within multi-tier Non-Terrestrial Networks (NTNs) comprising Low Earth Orbit (LEO), Medium Earth Orbit (MEO), and Geostationary Earth Orbit (GEO) satellite constellations. Its objective is to develop models, architectural designs, and resource management algorithms aimed at minimizing ground resource usage while optimizing coverage, beam patterns, power, and bandwidth. The goal is to enable effective resource allocation that meets the dynamic traffic demands and service-level agreement (SLA) requirements of subscribers. In Chapter 1, an overview of multi-tier NTNs is provided, covering research motivations and methodology. In Chapter 2, the impact of orbital variations on Doppler shift and packet arrival time is evaluated. A resource management technique utilizing dual connectivity (DC) between MEO and GEO satellites is developed to optimize capacity. Similarly, Chapter 3 presents a study on user equipment (UE) RF design for integrated service delivery in NTNs and examines multi-connectivity (MC) as a resource optimization strategy, where UEs can connect to multiple satellites to achieve higher peak throughput. Originally developed by the 3rd Generation Partnership Project (3GPP) for terrestrial communications in 4G and 5G, MC has shown significant gains in the terrestrial domain; this chapter investigates its potential in satellite communications. Although MC can increase throughput, it is limited by the UE's RF configuration. To address this, a terminal-aware multi-connectivity (TAMC) scheduling algorithm was developed, using available radio resources and propagation data to define an adaptive resource allocation pattern that optimizes uplink data rates while minimizing UE energy consumption. The algorithm operates with a multi-layer NTN resource scheduling architecture, incorporating a softwarized network-layer dispatcher that classifies and differentiates packets based on terminal types, such as IoT and VSAT, and outperforms benchmark algorithms.

Further, Chapter 4 extends this study to uplink transmissions, analyzing UE traffic demands across different traffic classes, including eMBB, URLLC, and mMTC. This chapter

also considers user service classifications to enable network dimensioning that meets quality of service (QoS) requirements. A resource management architecture is proposed for multi-tier NTNs, adapted to the 3GPP protocol stack. To enhance energy efficiency in uplink communications, an energy-efficient service-aware multi-connectivity (EE-SAMC) scheduling algorithm was developed. EE-SAMC uses available radio resources and propagation data to intelligently define a dynamic resource allocation pattern that reduces UE energy consumption while maximizing QoS. The algorithm is based on a non-convex combinatorial problem solved through two approaches: an optimization solution and a heuristic approach. In the optimization approach, the problem is divided into two subproblems—(i) joint route and power allocation and (ii) path matching—solved using the interior point algorithm and the Hungarian algorithm, respectively.

Multi-tier NTNs are expected to be a key enabler for 6th-generation (6G) systems, providing ubiquitous coverage. However, effectively managing heterogeneous networks to meet dynamic traffic demands in time-varying environments remains a challenge. Chapter 5 addresses this by exploring dynamic beam and resource allocation techniques to improve the capacity of multi-tier NTNs over stochastic channels in the down-link, meeting the diverse service level agreements (SLAs) of users. Here, a non-convex combinatorial optimization problem with inequality constraints is formulated, which is then separated into two subproblems: (a) dynamic beam allocation and (b) joint power and bandwidth allocation. The dynamic beam allocation subproblem is solved using an iterative algorithm, while joint power and bandwidth allocation employs a multi-agent deep reinforcement learning (MADRL)-aided resource allocation algorithm. This solution leverages MC to maximize capacity and operates within a network architecture with a hybrid gateway station (HGS) that manages satellites and supports various waveforms, including 5G New Radio (NR) and DVB-S2X. The algorithm determines resource allocation patterns based on channel quality indicators (CQI) and traffic classes, such as URLLC, HDTV, and eMBB.

To address the issue on efficient utilization of spectrum resources, operators are in search of innovative ways to dimension network resources and prevent resource under utilization, especially in a mult-tier NTN. Chapter 6 introduces a novel service delivery model where infrastructure providers (InPs) lease NTN resources as slices to mobile virtual service operators (MVSOs). These MVSOs then offer the leased resources to subscribers, facilitating efficient use of NTN resources within the telecommunications ecosystem. The model incorporates

an NTN slicing architecture with multi-layer satellites, including LEO, MEO and GEO constellations, featuring a HGS tailored to the virtualization architecture specified by 3GPP. In this context, a multi-objective optimization problem (MOOP) is formulated, comprising two combinatorial objectives for InPs and MVSOs aimed at maximizing revenue. The proposed algorithm addresses joint network slicing and admission control (AC) using techniques such as the non-dominated sorting genetic algorithm II (NSGA-II), multi-objective reinforcement learning (MORL), and a heuristic approach. It further enhances the AC mechanism by leveraging an LSTM-based deep learning model to predict traffic demand for URLLC and eMBB users, preventing SLA violations. Finally, Chapter 7 outlines conclusions and directions for future research.

Preface

This Ph.D. thesis was conducted between August 2021 and September 2024 at the Interdisciplinary Centre for Security, Reliability, and Trust (SnT) at the University of Luxembourg. The research was supervised by Prof. Bhavani Shankar at SnT, with co-supervision provided by Prof. Symeon Chatzinotas, Chief Scientist I and head of the SIGCOM research group at SnT, University of Luxembourg. Additionally, the thesis was undertaken in partnership with Société Européenne des Satellites (SES) in Luxembourg, represented by Dr. Hira Muzammil and Dr. Joel Grotz.

Support of the Thesis

This Ph.D. thesis has received support from the Luxembourg National Research Fund (FNR) through the Industrial Partnership Block Grant (IPBG) with reference number 14016225, for the project titled INSTRUCT: INtegrated Satellite–TeRrestrial Systems for Ubiquitous Beyond 5G CommunicaTions Networks. The significant support provided by SIGCOM is also acknowledged with gratitude.

Acknowledgments

I would like to begin by expressing my heartfelt appreciation to my supervisor, Prof. Bhavani Shankar, for his exceptional guidance and for providing countless opportunities for my professional growth. Completing this thesis would not have been possible without his unwavering support and continuous supervision. I am also deeply thankful to my co-supervisor, Prof. Symeon Chatzinotas, for his excellent technical advice and timely feedback on my research.

Additionally, I am grateful to Dr. Hayder Al-Hraishawi for his valuable guidance throughout my research. I would also like to extend my sincere gratitude to Dr. Joel Grotz from SES for his insightful technical guidance and for supplying the dataset used in this research. I am further grateful to Prof. Bjorn Ottersten for his constructive suggestions, which contributed to enhancing the quality of my research.

Lastly, I wish to thank Prof. Muhammad Imran from James Watt School of Engineering, University of Glasgow, United Kingdom, for kindly agreeing to be a member of the dissertation committee. I am also appreciative of Prof. Miguel Angel Olivarez Mendez for accepting to serve as the Chairman of the defense.

Dedication

I would like to dedicate this thesis to my son **Michael Cinwonsoko Dazhi**, who was born in the course of this research. You will achieve and accomplish greater things in your journey of life.

Michael Ninma Dazhi

Luxembourg, 11 Dec. 2024

Contents

List of Figures

List of Tables

Abbreviations

2DQN	Double DQN
3DQN	Dueling Double DQN
3GPP	Third Generation Partnership Project
4G	Four Generation of Mobile Communications
5G	Fifth Generation of Mobile Communications
5G NR	Fifth Generation New Radio
6G	Six Generation of Mobile Communications
AC	Admission Control
AI	Artificial Intelligence
API	Application Programming Interface
BH	Beam Hopping
BMF	Bottleneck Max Fairness
BPTT	Back Propagation Through Time
BSS	Broadcast Satellite Service
CA	Carrier Aggregation
CAPEX	Capital Expenses
CC	Component Carrier
CN	Core Network
CO2	Carbon Dioxide
CoB	Center of Beam
CQI	Channel Quality Indicator
CS	Clear Sky
CU	Centralized Unit
DC	Dual Connectivity
DL	Deep Learning

DQN	Deep Q Network
DU	Distributed Unit
DVB-S2X	Digital Video Broadcasting - Second Generation Satellite Extensions
DyBM-RA	Dynamic Beam Management Resource Allocation
E2E	End-to-End
EE	Energy Efficiency
EE-SAMC	Energy Efficiency Service Aware Multi-Connectivity
EIRP	Equivalent Isotropic Radiated Power
eMBB	Enhanced Mobile Broadband
ESA	European Space Agency
FSL	Free Space Loss
FSS	Fixed Satellite Service
GA	Genetic Algorithm
GBR	Guaranteed Bit Rate
GEO	Geostationary Earth Orbit
HAPS	High Altitude Platform Stations
HDTV	High Definition Television
HEO	High Elliptical Orbit
HGS	Hybrid Gateway Station
HPBW	Half Power Beam Width
HTS	High Throughput Satellite
IaaS	Infrastructure as a Service
IMT	International Mobile Telecommunication
InP	Infrastructure Provider
IoT	Internet of Things
IPA	Interior Point Algorithm
ISL	Inter-Satellite Link
KKT	Karush Kuhn Tucker
KPI	Key Performance Indicator
LEO	Low Earth Orbit
LoS	Line of Sight
LSTM	Long Short Term Memory

LTE	Long Term Evolution
LTE-A	LTE - Advanced
LTE-M	LTE for Machine Type Communication
MA2DQN	Multi-Agent 2DQN
MA3DQN	Multi-Agent 3DQN
MAC	Medium Access Control
MADQN	Multi-Agent DQN
MADRL	Multi-Agent Deep Reinforcement Learning
MAE	Mean Absolute Error
Max-Min	Maximum Minimum
MC	Multi-Connectivity
MDP	Markov Decision Process
MEO	Medium Earth Orbit
MIMO	Multiple Input Multiple Output
MINLP	Mixed Integer Non-Linear Programming
mMTC	Massive Machine-Type Communication
MODCOD	Modulation and Coding
MO-MDP	Multi-Objective MDP
MOOP	Multi-Objective Optimization Problem
MORL	Multi-Objective Reinforcement Learning
MSS	Mobile Satellite Service
MVSO	Mobile Virtual Service Operator
NAC-Rev-Max	Network Admission Control Revenue Maximization
NAS	Non-Access Stratum
NE	Network Element
NFV	Network Function Virtualization
NGSO	Non-Geostationary Orbit
NIaaS	NTN Infrastructure as a Service
NLoS	Non LoS
NOC	Network Operation Center
NPaaS	NTN Platform as a Service
NSaaS	NTN Software as a Service

NSGA	Non-dominated Sorting Genetic Algorithm
NSGA-II	Non-dominated Sorting Genetic Algorithm II
NTN	Non-terrestrial Network
OPEX	Operational Expenses
ORAN	Open RAN
OSI	Open System Interconnect
PDCP	Packet Data Convergence Protocol
PDU	Packet Data Unit
PF	Proportional Fairness
PL	Path Loss
PWMT	Path Weight Matching Technique
QoE	Quality of Experience
QoS	Quality of Service
RA	Resource Allocation
RAN	Radio Access Network
RB	Resource Block
Rev-Max	Revenue Maximization
RF	Radio Frequency
RFD	Rain Fading
RIC	Radio Intelligent Controller
RL	Reinforcement Learning
RLC	Radio Link Controller
RR	Round Robin
RRC	Radio Resource Control
RS	Resource Scheduler
RU	Radio Unit
SDAP	Service Data Adaptation Protocol
SID	Service Identification
SLA	Service Level Agreement
SNR	Signal to Noise Ratio
SR	Slice Request
SSU	Service Segmentation Unit

SUL	Supplementary Uplink
TAMC	Terminal Aware Multi-Connectivity
TB	Transport Block
TWTA	Traveling Wave Tube Amplifiers
UAS	Unmanned Aerial System
UAV	Unmanned Aerial Vehicle
UE	User Equipment
URLLC	Ultra-Reliable Low-Latency Communication
VHTS	Very High Throughput Satellite
VSAT	Very Small Aperture Terminal

Notations

$\log_x(a)$	The logarithm of a in base x.
$\ln(a)$	The natural logarithm of a.
e^a	The exponential function of a.
$\mathcal{L}(a)$	The Lagrange function of a.
$\mathbb{E}[\cdot]$	Expected value.
$[K]$	dB value of K.
$\boldsymbol{L}^\dagger$	Complex conjugate transpose (Hermitian) of vector $\boldsymbol{L}$.
$\text{diag}(\boldsymbol{v})$	Diagonal matrix with vector $\boldsymbol{v}$ on the main diagonal.
$\lvert\boldsymbol{h}\rvert$	The magnitude (absolute value) of vector $\boldsymbol{h}$.
max	Maximum operation.
min	Minimum operation.
$b \in \mathcal{B}$	Element b belongs to set $\mathcal{B}$.
$\boldsymbol{A} \odot \boldsymbol{B}$	The Hadamard product of matrices $\boldsymbol{A}$ and $\boldsymbol{B}$.

Chapter 1

Introduction

This chapter introduces the innovative concept of Multi-Orbital Non-Terrestrial Networks (NTNs), which harnesses the potential of satellites operating across Low Earth Orbit (LEO), Medium Earth Orbit (MEO), and Geostationary Earth Orbit (GEO) to provide services within a diverse traffic ecosystem. The network architecture is characterized by Hybrid Gateway Stations (HGS), strategically positioned to manage the satellite constellations effectively. These HGS incorporate both Distributed Units (DUs) responsible for antenna management across different orbital planes and a Centralized Unit (CU) for signal processing and modulation, ensuring seamless communication within and between orbits. Leveraging the 3rd Generation Partnership Project (3GPP) protocol stack, the network enables efficient resource management across all layers, optimizing resource allocation in response to dynamic traffic demands. Various techniques for efficient resource utilization are explored, offering insights into the effective operation of multi-orbital NTNs. Through comprehensive use-case analyses, the potential applications of multi-orbital NTNs in dynamic service delivery scenarios are examined, highlighting their versatility and adaptability in meeting evolving communication needs.

The next section presents an overview of a satellite communication system. Additionally, it discusses the motivation, methodology, scope, and contributions of this thesis.

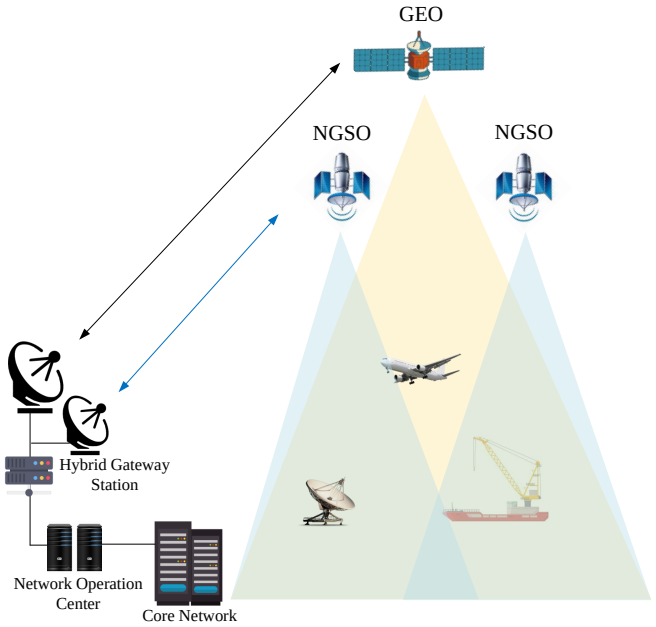

Figure 1.1: Multi-orbital NTN Network Topology.

1.1 Overview of Multi-Orbital NTN for Integrated Service Delivery

The topology of the multi-orbital NTN is shown in Fig. 1.1. This topology involves the radio access network (RAN) connected to the core network (CN). The RAN includes the orbital satellites in Low Earth Orbit (LEO), Medium Earth Orbit (MEO), and Geostationary Orbit (GEO), which are managed by a hybrid gateway station [1]. Various user terminals access the network through the air-interface to the satellites, which can be either DVB-S2X or 5G NR. These terminals differ in their radio frequency (RF) requirements and have dynamic traffic demands for different services. The distinguishing RF terminal characteristics include antenna gain, frequency band, transmit power, and antenna polarization [2].

1.1.1 NTN Layers

There are different types of NTN orbital layers with varying properties, as outlined in Table 1.1. These NTN layers include LEO, MEO, GEO, and high elliptical orbit (HEO), which satellites can operate in. In addition, radio access provided by unmanned aerial systems (UAS), including high altitude platform stations (HAPS), is considered NTN access nodes

with reduced Doppler and delay. The layers have different altitudes, beam diameters, and other properties [3].

Table 1.1: Types of NTN Layers with Properties [3]

NTN Layers	Altitude (Km)	Beam diameter (Km)	Orbit
LEO	300 - 1,500	100 - 1,000	Circular
MEO	7,000 - 25,000	100 - 1,000	Circular
GEO	35,786	200 - 3,500	Circular
HEO	400 - 50,000	200 - 3,500	Elliptical
UAS (including HAPS)	8 – 50 (HAPS is 20)	5 - 200	-

1.1.2 Hybrid Gateway Station

This HGS functions as a collocated station where the three orbital access networks can be managed simultaneously. This strategy optimizes space requirements and further minimizes capital expenses (CAPEX), including operational expenses (OPEX) [1, 4]. The HGS is adapted to the open RAN (ORAN) framework, where each of the orbital feeders has different distributed units (DUs) with antenna ports and is connected to a centralized unit (CU). The resource allocation policy and algorithm operate with software-defined network and network function virtualized elements.

1.1.3 User Terminals

User Equipment (UE) in multi-layer NTNs is a critical component designed to operate seamlessly across various layers of satellites and aerial platforms [5]. These devices, ranging from smartphones to specialized IoT sensors, require advanced capabilities to efficiently handover between different network layers while maintaining uninterrupted service. Given the dynamic and often challenging environments in which NTNs operate, UE in these networks requires sophisticated antenna systems for reliable signal acquisition and tracking, adaptive modulation and coding schemes to optimize data throughput and error rates, and enhanced power efficiency to support prolonged operation [6]. Furthermore, these devices must incorporate advanced mobility management protocols to facilitate seamless handovers between NTN nodes, ensuring continuous service even in remote or underserved areas. As NTNs evolve to support emerging applications like autonomous vehicles, IoT deployments, and real-time industrial control, the design and performance of UE will play a pivotal role in realizing the full potential of these advanced communication networks.

In this direction, the collaboration between the satellite industry and the 3GPP to integrate satellite networks into the 5G ecosystem has resulted in handheld users being served by LEO and GEO satellites in the S-band, utilizing appropriate satellite beam layouts [7]. Additionally, UE with high transmit and receive antenna gains, such as VSATs and phased array antennas, can be served by LEO and GEO satellites in both the S-band and Ka-band [3]. This integration requires that 5G functionalities address the challenges of long propagation delays, significant Doppler shifts, and moving cells in NTNs, as well as improve timing and frequency synchronization. The characteristics of this EU are detailed in the 3GPP specifications [3]. In the context of satellite 5G-NR, several types of UE are considered to operate effectively within NTNs as outlined in the Table below. Specifically, Table provides an overview of the different types of UE in satellite 5G-NR, along with their descriptions, frequency bands, and typical applications.

Table 1.2: Types of User Terminals

Type of UE	Description	Frequency Bands	Applications
Handheld Devices	Equipped with omnidirectional antennas (e.g., dipole antennas)	S-band	General consumer use, broad coverage
VSAT	Directional antennas (phased array, circular polarization, 60 cm aperture)	S-band, Ka-band	High-throughput applications, stable connections
Phased Array Antenna Systems	High transmit/receive gains, dynamic beam steering	S-band, Ka-band	Multiple connections, LEO/GEO communications
IoT Devices	Low-power, wide-area network connectivity, compact antennas	Specific bands	Environmental monitoring, asset tracking
Fixed Broadband Terminals	Large, stationary antennas	Ka-band	Broadband internet in remote/underserved areas
Mobile Broadband Terminals	Antennas for moving platforms (ships, airplanes, trains), adaptive beam steering	Ka-band	High-speed internet access on the move
Mission-Critical Communication Devices	Ruggedized, highly reliable devices	Various bands	Emergency services, disaster response
Automotive and Autonomous Vehicle Terminals	Integrated into vehicles, continuous connectivity, advanced antennas for seamless handover	Various bands	Navigation, autonomous driving communication

To effectively meet the diverse demands of future communication networks, the following aspects highlight the complexity and advanced technological requirements of UE in multi-layer NTNs:

- **Antenna Design and Technology**: The antenna systems of UEs in NTNs need to be highly adaptable. They must support various beamforming and beam-steering capabilities to maintain a stable link with fast-moving satellites or aerial platforms. These antennas should also be capable of handling multiple frequency bands to facilitate

carrier aggregation and dual/multi-connectivity.

- **Power Efficiency**: Given the extended communication distances and the dynamic nature of NTNs, power efficiency is a critical aspect for UE design. Efficient power management techniques are essential to extend battery life, particularly for handheld and IoT devices operating in remote or inaccessible locations.

- **Doppler Shift Compensation**: NTNs are characterized by Doppler shifts due to the high velocities of satellites and aerial platforms. UEs must incorporate advanced algorithms for delay and Doppler shift compensation to maintain the integrity and performance of the communication links.

- **Interoperability**: UEs in NTNs should be capable of interoperating with various communication standards and technologies. This interoperability ensures seamless communication across different network types and facilitates the integration of NTNs with existing terrestrial networks and upcoming technologies like 6G.

- **Software-Defined Functionality**: Modern UEs are increasingly adopting software-defined functionality, allowing for remote updates and reconfiguration of communication protocols, frequency bands, and other operational parameters. This adaptability is crucial for maintaining compatibility and performance as NTNs evolve.

- **Security and Privacy**: Due to the broad coverage and potential vulnerabilities of NTNs, UEs must incorporate robust security measures to protect data transmission against eavesdropping, jamming, and other cyber threats. Privacy protocols are also essential to safeguard user data in compliance with regulatory standards.

The ongoing advancements in UE design, including improved mobility management, adaptive antennas, and robust power efficiency, will support this vision by ensuring that devices are capable of harnessing the full potential of integrated NTN and terrestrial networks. This synergy will foster a new era of connectivity, where users experience unparalleled service continuity, high performance, and enhanced access, driving forward innovations and applications previously thought unattainable.

One of the most interesting prospects is the emergence of direct-to-cell technology. This innovation allows UEs to establish direct communication links with satellites, bypassing traditional terrestrial network infrastructure. Such direct connectivity can dramatically enhance

network resilience, reduce latency, and provide seamless service even in the most challenging environments. As direct-to-cell technology becomes more refined, it will enable users to access high-speed internet and communication services from anywhere on the globe, ensuring that no location is left underserved.

1.1.4 Resource Management

The resource management is a very important aspect of the multi-orbital NTN system, as this defines the policies that will be implemented as algorithms for the intelligent routing of traffic and optimization of capacity for enhanced QoS, particularly data rate and delay [1].

Carrier Aggregation

Carrier aggregation (CA) technique was introduced to terrestrial networks in the Long Term Evolution-Advanced (LTE-A) standard, allowing multiple component carriers across available spectrum bands to be flexibly combined, thereby supporting wider transmission bandwidth and increasing overall system capacity [8]. In terrestrial networks, CA has significantly enhanced performance by maximizing spectrum utilization and meeting extremely high throughput requirements [9]. This technique not only efficiently exploits the available spectrum but also maintains user QoS through effective interference management and avoidance capabilities [10]. Therefore, multiple research efforts have been undertaken to integrate CA n with satellite system architectures, aiming to harness multiplexing gains by dynamically distributing traffic over multiple carriers [11–13].

In the context of multi-layered NTNs, CA presents a promising solution to the inherent challenges of satellite communication systems, such as limited bandwidth and high latency. By leveraging CA , NTNs can enhance their spectral efficiency and provide higher data rates, thereby improving the overall user experience [14]. This is particularly beneficial in multi-layered NTNs, where the integration of various NTN layers and satellite orbits, such as GEO, MEO, and LEO, requires sophisticated coordination to optimize the use of the available spectrum. Furthermore, CA can offer customized bandwidth configurations tailored to specific user needs, providing a high degree of flexibility in resource allocation. In particular, the flexible management of aggregated carriers enables NTNs to adapt to varying traffic demands and maintain consistent QoS for users, thereby supporting diverse applications ranging from broadband internet to critical communication services. Through

effective CA, traffic can be dynamically allocated across different NTN layers, ensuring more balanced load distribution and reduced congestion.

Furthermore, multi-layered NTNs offer a promising solution for backhauling 5G and 6G services. Compared to traditional backhaul options, they provide several advantages: wider coverage, increased capacity, greater flexibility, and enhanced reliability. This enables a seamless, robust, and ubiquitous connectivity experience, forming a critical foundation for the next generation of wireless communication technologies. However, a potential bottleneck exists in the backhaul links connecting the various system elements, as these links can become overwhelmed by high data traffic. This is where CA comes into play. By combining multiple backhaul carriers, CA significantly increases the overall capacity of the network. This allows for more efficient data transfer between various network elements, ensuring smooth operation even under high-demand conditions. This enhancement is crucial for supporting the advanced applications and services that 5G and 6G technologies promise, such as IoT, augmented reality, and autonomous vehicles.

Moreover, CA in NTNs can significantly boost the robustness and reliability of satellite communication links. The ability to aggregate carriers from different frequency bands allows NTNs to mitigate the impact of adverse conditions such as atmospheric attenuation, rain fade, and other environmental interferences. This capability ensures that the communication links maintain high performance and resilience, even in challenging conditions. Similarly, CA can improve the reliability and resilience of NTN backhaul links. By distributing traffic across multiple carriers, NTNs can maintain service continuity even if individual carriers experience interference or degradation. This redundancy is crucial for supporting the high reliability standards of 5G and 6G services, particularly for critical applications requiring consistent and dependable connectivity. Thus, CA not only boosts the capacity of NTNs but also fortifies their role as a dependable backhaul solution for future wireless networks.

As NTNs continue to evolve, the integration of CA will be crucial in meeting the increasing demand for high-capacity and reliable satellite communication services. By dynamically managing and allocating spectral resources, CA helps mitigate the limitations of traditional satellite systems, paving the way for more robust and adaptive network architectures capable of supporting a diverse array of applications and services.

Dual-Connectivity and Multi-Connectivity

In the evolving landscape of multi-beam satellite architectures, dual connectivity (DC) allows users to be simultaneously served by different systems and frequency bands. Introduced by the 3GPP in Release 12 for 5G-NR, DC aims to maximize spectrum utilization and prevent traffic overload. This approach enables a single user equipment (UE) to connect to both terrestrial base stations and non-terrestrial platforms, providing improved coverage and reliability. By leveraging the wider coverage of non-terrestrial nodes while maintaining reliable connections with terrestrial networks, DC is particularly valuable in areas with limited terrestrial infrastructure or challenging propagation environments [2]. Additionally, DC enhances load balancing and resource utilization, mitigating network congestion by offloading data traffic between the two connections. However, DC introduces additional complexity in signaling overhead and resource management to maintain seamless operations between connected nodes.

To fully leverage the flexibility and scalability of emerging multi-layered NTN architectures and integrated space-aerial-terrestrial networks, extending DC to multi-connectivity (MC) is essential [2]. MC takes connectivity further by allowing UEs to connect to multiple NTN nodes simultaneously, such as different satellites within the same orbit or across different orbits. MC offers superior coverage and seamless handovers by enabling connections to multiple terrestrial base stations, HAPs, UAVs, or LEO satellite, guaranteeing near-ubiquitous coverage and uninterrupted connectivity for applications like autonomous vehicles or real-time industrial control. Additionally, MC enhances network capacity and resource allocation by distributing traffic across multiple nodes, maximizing network capacity and minimizing congestion. This approach not only achieves higher per-user data rates but also provides mobility robustness, improving the resilience of wireless communications.

Employing MC in multi-layered NTNs helps meet the asymmetry and heterogeneity of traffic demands, ensuring consistent and reliable connectivity despite diversified and randomly distributed data traffic [4]. Furthermore, MC can play a role in integrating legacy communication systems into the ever-evolving network landscape. UEs equipped with MC could potentially connect to both a modern 5G/6G network and an older communication system, ensuring continued functionality for devices that might not be readily compatible with the latest standards. However, MC poses daunting challenges in control signaling overhead and managing complex interactions between multiple NTN nodes. The increased hardware

complexity required for UEs to handle multiple connections also needs careful consideration.

Both DC and MC offer exciting possibilities for unlocking the full potential of multi-layered NTNs. The choice of approach depends on specific network requirements and deployment scenarios. As research and development progress, advancements in control signaling techniques, resource management algorithms, and hardware capabilities will be crucial for realizing the full potential of these technologies, ushering in a new era of robust and ubiquitous connectivity.

Supplementary Uplink

Supplementary Uplink (SUL) is a feature introduced in 5G-NR designed to enhance uplink performance, particularly in scenarios where the primary uplink spectrum faces limitations due to coverage or capacity constraints. By utilizing lower frequency bands, which offer better propagation characteristics compared to higher frequency bands, SUL provides improved uplink coverage [15]. Integrating SUL within multi-layered NTNs can significantly enhance performance and reliability, ensuring robust and ubiquitous connectivity [16]. This is especially useful in challenging environments, such as deep rural areas, mountainous regions, or dense urban settings, where maintaining a reliable connection can be difficult.

SUL's ability to dynamically supplement the primary uplink channel with additional lower frequency bands enhances spectrum efficiency in multi-layered NTNs. This dynamic allocation allows the network to adapt to varying user demands and environmental conditions, optimizing spectrum use and reducing congestion. Additionally, the redundancy provided by SUL increases NTN reliability. If the primary uplink band faces interference or congestion, SUL can maintain the communication link, ensuring continuous and dependable service. This is crucial for mission-critical applications such as emergency services, remote healthcare, and disaster response.

However, integrating SUL within multi-layered NTNs requires careful planning and resource allocation strategies [17]. Network coordination is essential to determine which uplink channel (main or SUL) is best suited for each user equipment based on real-time signal strength, location, and network load. This dynamic approach leverages the strengths of both SUL and the main uplink carrier, optimizing uplink performance and user experience within the NTN architecture [18].

The integration of SUL in multi-layered NTNs supports a wide range of applications. In

maritime and aeronautical communications, where continuous and reliable connectivity is essential, SUL ensures robust uplink performance, supporting real-time monitoring, navigation, and communication. In massive IoT deployments, especially in remote industrial operations such as mining or oil and gas exploration, SUL provides consistent uplink connectivity, enabling effective data transmission from sensors and devices scattered over vast areas. This integration not only addresses the challenges of connectivity in remote and underserved areas but also enhances the role of NTNs in supporting upcoming 6G services and applications.

1.1.5 Use cases, Service Models for Multi-orbital NTN and Applications

The multi-orbital NTN has various use cases applicable to real-life situations, which are discussed extensively. Service models are also outlined with examples from the industry.

5G use cases for Multi-orbital NTN

These use cases are referenced to the ITU-R 5G defined categories for International Mobile Telecommunications (IMT) for 2020 and beyond, which include enhanced mobile broadband (eMBB), ultra-reliable low-latency communications (URLLC), and massive machine-type communications (mMTC) with applications in multi-orbital NTN [19].

NTN use cases for eMBB

The 5G use cases for eMBB in relation to NTN are outlined below, as described in [20, 21].

- **Backhauling and tower feed**: In this use case, NTN is employed to provide high-speed traffic backhauling for 5G to edge networks. This includes broadcasting and multicasting capabilities over a wide coverage area at the network edge.

- **Communications on the move**: Here, NTN provides 5G connectivity to moving platforms such as trains, airplanes, and maritime vessels.

- **Hybrid multiplay**: This use case integrates NTN with terrestrial networks to deliver 5G services to premises (homes and offices) in underserved areas.

- **Trunking and head-end feed**: In this scenario, NTN facilitates high-speed trunking and feeding of 5G connections to remote centralized terrestrial sites or base stations, which are then distributed terrestrially to other local base stations.

NTN use cases for mMTC

The mMTC use cases involve IoT services that utilize low-power devices (sensors) requiring minimal traffic transmissions, which can be densely distributed over a wide area. Applications of mMTC in NTN include asset tracking, oil infrastructure surveillance, and agricultural management.

NTN use cases for URLLC

The URLLC use case involves services that are delay intolerant. Most of these services are provided by 5G terrestrial networks to meet the required delay standards. In NTN, LEO satellites offer the lowest delay metrics. Consequently, LEO satellites are used to provide low-latency services, with delays typically around 30 ms [2]. In some cases, they also complement terrestrial networks to enhance performance for low-latency applications.

Location based use cases for multi-orbital NTN

This section focuses on the demand for the utilization of multi-orbital NTN across different locations, including urban, suburban, rural, and remote areas, as illustrated in Figure 1.2.

- **Urban Areas**: In urban areas, the demand is primarily for high-capacity, low-latency services. This demand arises from the predominant activities, which include large-scale metropolitan mobility, corporate and government office operations, healthcare centers, and shopping complexes. Consequently, the NTN services required in these areas include emergency response connectivity, land mobile connectivity, cloud services, connected cars, and terrestrial back-hauling.

- **Sub-urban Areas**: In suburban areas, which are mainly characterized by manufacturing, industrial, and processing plant activities, the primary services required include Internet of Things (IoT) applications, public safety, and Industry 4.0 solutions.

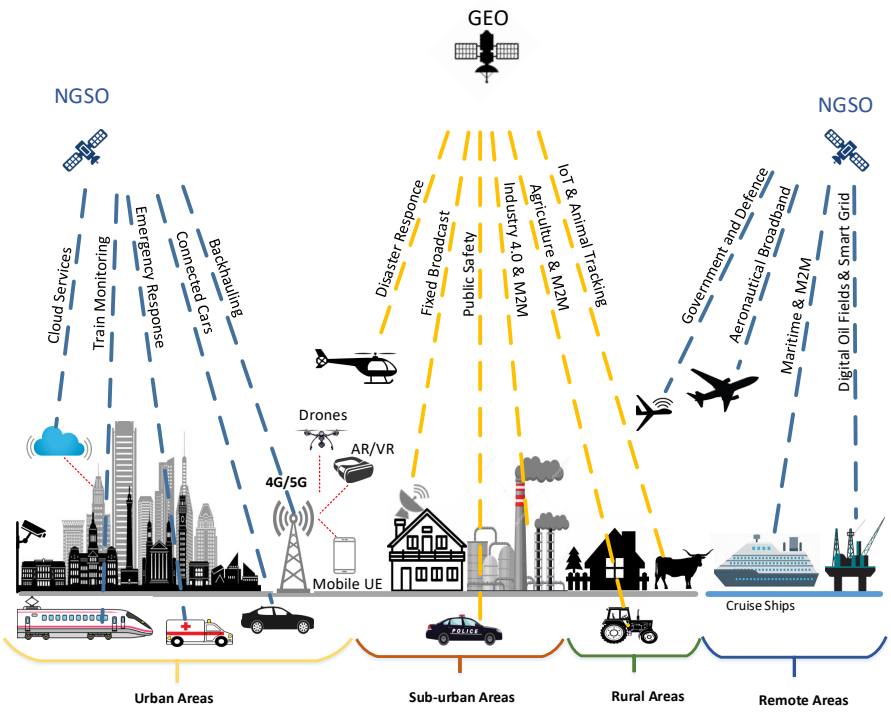

Figure 1.2: Schematic of the Use-Cases in Multi-Tier NTN with respect to location [20].

- **Rural Areas**: Rural areas are typically focused on agriculture and industrial processing. The connectivity services needed here include asset monitoring, IoT, machine-to-machine communications, and Industry 4.0 solutions.

- **Remote Areas**: Remote areas encompass high-altitude regions where aeronautical broadband and navigation services are necessary. Additionally, remote areas can include deep-sea environments, where required services include cruise ship broadband, maritime navigation, oil rig data management, and IoT.

Service Models for multi-orbital NTN

- **NTN aided Infrastructure as a service (NIaaS)**: The NIaaS model involves providing infrastructure enabled by NTN (Non-Terrestrial Networks) for various service offerings. This infrastructure includes the allocation of physical resources such as bandwidth, transponders, satellite access networks, satellite core networks, and gateway stations. Potential services offered under this model include backhauling for terrestrial

networks, content broadcasting, access networks for IoT, UAV, mobile communications, and fixed satellite services; as well as gateway stations for data center access and telemetry, tracking, and control services. In this model, the customer does not have the privilege to manage or control the infrastructure directly; rather, they only have control over the deployed services. The infrastructure provider bills the NIaaS customer based on the amount of resources allocated and consumed. An example is OneWeb providing satellite backhauling services to British Telecom (BT) for rural or remote telecommunications coverage in the UK [22].

- **NTN aided Platform as a Service**: The NPaaS model involves the design, development, and execution of underlying software and hardware systems by the NTN operator to establish platforms for customers. The operator provides an environment where application developers can set up their application services. Services available on these platforms include cloud data storage, database administration, web servers, web hosting, development tools, simulators, and multimedia content hosting. Application developers run and manage their applications on the platform created by the NTN operators, without interfering with the underlying network configurations. Operators bill developers based on application runtime requirements and service complexity. An example is the Spire cloud-based satellite constellation platform, which offers a web application programming interface (API) for subscribed developers to create and manage their applications on the platform [23].

- **NTN aided Software as a Service**: NSaaS is a model where the satellite provider develops applications that run over their network to offer various services to customers. The operators manage the infrastructure and platform that support these applications, which are essentially developed by the operators themselves. Customers access these services through monthly or periodic subscription plans. The applications available in this model include online gaming, email, voice communication, instant messaging, surveillance, and office tools such as word processing and spreadsheets. An example of this is the SES Common Operational Picture (COP) platform, known as Hydra. Designed for government use, Hydra is a web-based control and monitoring system

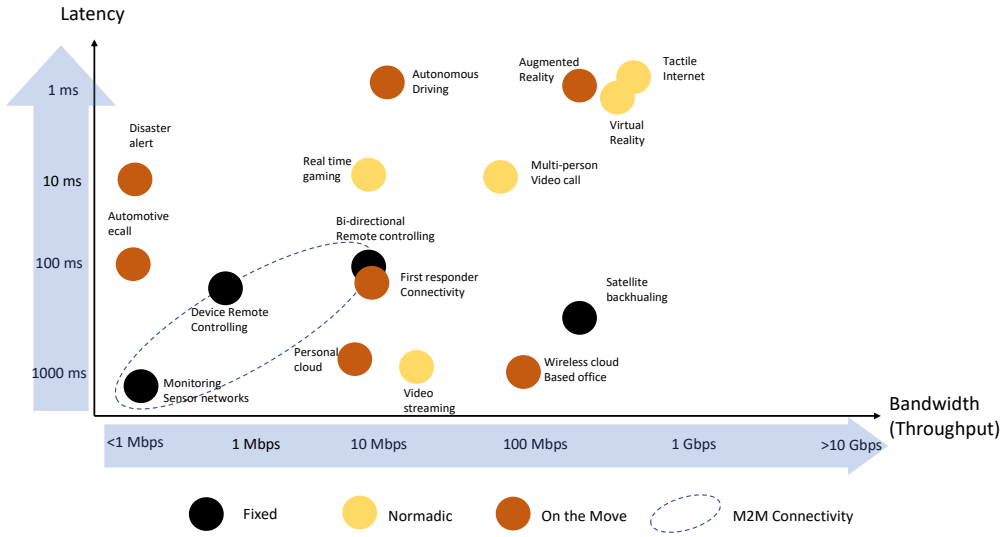

Figure 1.3: Reference Metric of Some Use-Cases. [25]

that provides end-to-end situational awareness through a unified network platform. It is built on the SES Government Network [24].

Performance Metric for the Use Cases

The estimated performance metric for the services of the use cases in terms of rate and latency is shown in Fig. 1.3.

1.2 Research Motivation

The number of mobile and internet users, along with network traffic, is experiencing exponential growth. Specifically, the global number of internet users is projected to increase by 1.1 billion from 2024 to 2029, representing a 16.92% rise and bringing the estimated total to 7.3 billion by 2029 [26].

Similarly, the number of global Internet of Things (IoT) connections is expected to grow from 15.7 billion in 2023 to 38.8 billion by 2029, at a compound annual growth rate (CAGR) of 16% [27].

Satellite communication, in conjunction with terrestrial networks, will play a crucial role in meeting this rising demand. In 2024, the satellite communications market is valued at approximately 193.30 billion USD, with projections to reach 297.25 billion USD by 2029, reflecting a CAGR of 8.99% [28].

However, for satellite communication to serve as an effective solution within this expanding telecommunications ecosystem, the following factors are essential:

- **Dynamic traffic demand:** Conventional satellites face limitations in handling dynamic traffic, particularly those with single layers or orbits. Today's traffic demand is both dynamic and heterogeneous, necessitating flexibility in satellite networks for efficient service delivery. For example, service and traffic demands for satellite networks may include asset monitoring (IoT), broadcasting (radio, TV, and HDTV), positioning/navigation (GPS), remote sensing, broadband (video streaming), and mobile communication (packet and voice services). Additionally, there are various satellite services, such as fixed satellite service (FSS), mobile satellite service (MSS), and broadcast satellite service (BSS). Examples of these services include backhauling for FSS, aviation and maritime communication for MSS, and direct-to-home (DTH) services for BSS. Similarly, the 3GPP is integrating non-terrestrial networks (NTN) into 5G, where different 5G use cases, such as ultra-reliable low-latency communication (URLLC), enhanced mobile broadband (eMBB), and massive machine-type communication (mMTC), will require distinct network technologies to meet the required quality of service (QoS). This underscores the heterogeneous nature of demand. Therefore, the next-generation satellite network should be a multi-orbital NTN, equipped with advanced algorithms to enable the efficient delivery of services, accommodate dynamic traffic demands, and fulfill diverse use cases.

- **Multi-orbital Constellations with Advanced Gateways:** Several satellite operators, such as SES, operate MEO/GEO constellations, and many are adopting multi-orbital networks [29]. Additionally, some operators are merging their businesses to offer a broader portfolio of services [30]. This trend is encouraging industry players to adopt heterogeneous networks to meet dynamic network demands. Traditionally, gateway design has involved deploying a single gateway to manage a single orbital constellation. However, in a multi-orbital NTN constellation, a more robust and efficient gateway design is necessary.

- **User Equipment Design:** The industry is increasingly focused on innovating user equipment (UE) with multi-orbital and multi-band capabilities [31]. This advancement will enable seamless connectivity and handover across different orbits and satellites

with different frequency bands within a single terminal, thereby reducing the number of terminal components needed to connect to a multi-orbital NTN.

- **Flexible Resource management:** Conventional satellite networks typically operate with uniform and static resource allocation mechanisms for beams and power, as well as fixed bandwidth dimensioning. This initial resource allocation architecture makes conventional satellites unsuitable for meeting the dynamic traffic demands and diverse use cases of today. This static allocation approach often results in both over-allocation and under-dimensioning of resources, leading to inefficient resource management and unmet service demands. To address these challenges, next-generation satellite networks must adopt robust architectures and satellites equipped with adaptive digital payloads, as well as advanced and flexible resource allocation algorithms capable of meeting dynamic traffic demands. Additionally, strategies such as software-defined networking (SDN) and optical inter-satellite links (ISLs) can be employed to enhance the capacity and QoS provided.

- **Spectral Efficiency:** The growing deployment of thousands of satellites, particularly NGSO constellations, is placing significant pressure on the already scarce spectrum [32]. Consequently, satellite operators are compelled to use their allocated spectrum efficiently to achieve optimal economic value while satisfying subscriber SLAs and meeting QoS requirements.

- **Energy Consumption:** One of the major challenges in satellite communication is power and energy limitations, particularly in the uplink [33]. Therefore, innovative techniques are needed to optimize power consumption and improve energy efficiency.

- **Intelligent Management of Large Network:** In a network with a large and fluctuating number of users with dynamic traffic demands and varying use cases, operating across a heterogeneous network of multiple satellites in different constellations with changing stochastic channel conditions, effective management becomes essential. Such a dynamic and complex network requires intelligent solutions for resource management, orchestration, billing/subscription management, reconfiguration, and optimization. Artificial intelligence and machine learning methods can be leveraged to develop innovative and efficient management strategies.

1.3 Research Questions

Building on the research motivation outlined in this work, which focuses on resource management in multi-tier NTNs involving LEO, MEO, and GEO constellations, several challenges have been identified in this area. This thesis aims to address the following research questions to develop novel models, strategies, algorithms, and architectures for effective resource management in multi-orbital NTNs.

Question 1: How can multiple orbits be utilized simultaneously for resource allocation in a multi-orbital NTN radio environment, while accounting for the dynamic properties of the orbits?

In this context, MEO and GEO are investigated based on their differing orbital properties, including Doppler effects, altitude, and packet arrival time. This thesis evaluates how dual connectivity (DC) can be established by UEs with dynamic orbital satellites and the benefits it brings to resource management for users. Furthermore, DC is analyzed with a focus on resource management within the DVB-S2X protocol stack.

Question 2: How can terminals be designed to operate effectively in a multi-orbital NTN radio environment, with the objective of satisfying dynamic user demands while ensuring minimal power consumption?

In this context, various classes of terminals are investigated and designed based on their radio frequency characteristics to meet user traffic demands while ensuring reduced power consumption. Accordingly, this thesis explores resource management techniques utilizing these different classes of terminals and examines their performance. A major technique analyzed is multi-connectivity (MC), which enables a single UE to connect to multiple satellites, optimizing capacity. Furthermore, a link budget analysis is conducted for each terminal class to evaluate the impact of the waveform on the transmission channel.

Question 3: How can seamless global coverage be ensured with minimal use of ground resources for three orbital constellations: LEO, MEO, and GEO, in order to optimize CAPEX?

In this area, an effort is made to design a novel teleport and gateway architecture that optimizes space and reduces OPEX and CAPEX requirements. Network virtualization

and softwarization are evaluated in the proposed design for the gateway stations to minimize equipment space. Additionally, an Open RAN architecture that includes radio units, decentralized units, and centralized units is investigated and incorporated into the design of the optimized gateway station. This approach aims to co-locate the feeder functions for LEO, MEO, and GEO orbits while centrally managing all orbits using a decentralized antenna architecture.

Question 4: How can an energy-efficient resource scheduler be designed for a multi-orbital NTN to meet the dynamic traffic SLAs of URLLC, mMTC, and eMBB, taking reverse transmission into account?

Several methods for achieving uplink transmission is investigated, particularly focusing on user scheduling methods. Three classes of 3GPP traffic use cases are considered: URLLC, mMTC, and eMBB, within the context of multi-orbital NTN capacity involving LEO, MEO, and GEO satellites. The problem is formulated as a combinatorial optimization challenge, aiming to identify an optimal combination of resource variables, including resource blocks, component carriers, and satellites, from the available radio capacity under defined constraints. The investigation encompasses two key areas: orbital path assignment and resource (power) allocation. A robust energy-efficient metric is derived to capture energy consumption at the UE. This thesis evaluates nonlinear programming and heuristic methods to solve the constrained optimization problem. Additionally, for the orbital path assignment aspect of the problem—ensuring SLA satisfaction, a combinatorial optimization algorithm designed to solve assignment problems in polynomial time by finding the minimum-cost matching in a bipartite graph is explored.

Question 5: How can we satisfy constantly changing, geographically distributed, time-varying traffic demands while ensuring spectral efficiency and SLA compliance in a large scale network?

To address this query, a dynamic beam allocation method is proposed that incorporates a beamforming network (BFN) within the network architecture of multi-orbital LEO, MEO, and GEO constellations, enabling dynamic geographically distributed beam positioning. In this context, a resource allocation optimization problem is formulated, taking into account a stochastic Rician channel model in the presence of interference.

Users with dynamic traffic demands are further examined under two channel conditions using channel quality indicators (CQI), allowing for the evaluation of user performance under various weather-affected channel conditions. Given the time-varying nature of the problem, which involves the dynamic allocation of power, beam gain, and bandwidth in diverse radio environments, a multi-agent reinforcement learning approach is proposed to solve the problem.

Question 6: In a multi-orbital NTN with divergent capacity distributed across space and on the ground, how can resources be effectively dimensioned to meet dynamic demands and enhance revenue?

In this context, a strategy is explored to enable the simultaneous dimensioning and allocation of bulk capacity composed of ground and space resources. This involves investigating network slicing and suitable service models to facilitate continuous demand and provision of network capacity, either directly or indirectly from users. Consequently, multiple interconnected optimization problems are formulated and solved using genetic algorithms, machine learning, and heuristic approaches. Additionally, various admission control algorithms are evaluated alongside intelligent deep learning traffic prediction algorithms to ensure SLA compliance across different traffic classes. Revenue evaluation, along with other metrics, is conducted to assess the effectiveness of the solution from both scientific and commercial perspectives.

1.4 Research Methodologies

The methodology for this research is outlined as follows. The research begins with a review of the state of the art in related areas, identifying gaps and noting limitations. Next, a system and network model is developed that serves as a framework for formulating the identified research gap problems. Subsequently, novel research problems are formulated based on these gaps. These problems are then solved through detailed analysis, and the corresponding performance is compared with benchmark methods. Finally, conclusions are drawn as the last step of the research process.

Summary of Research Methodology Strategy:

- **Algorithm**: This research explores various algorithms, including genetic algorithms, ML and AI methods, and heuristic algorithms.

- **Modeling**: The system and network modeling was developed by occasionally adopting standardized models from organizations such as 3GPP, ITU, and ETSI, as well as other published models from top-tier IEEE journals, ensuring adherence to the principles of a practical communication model.
- **Simulation**: Simulations were conducted using sophisticated and robust tools such as STK, MATLAB, Python, and Microsoft Excel.
- **Dataset**: In instances where a dataset was used in the research, live traffic data from the SES satellite operator was adopted for machine learning analysis.
- **Research Validation**: The proposed problems and solutions were subjected to rigorous scrutiny through submissions to and acceptances by top-tier IEEE conferences and journals, which served as a validation chamber for the research.

1.5 Contributions and Related Publications

This section outlines the primary contributions of the thesis. Furthermore, the research has led to the publication or submission of several papers in peer-reviewed journals, book chapters, and conference proceedings. These publications are categorized as follows: with **J representing journals, B for book chapters, and C for conferences**.

Chapter 1

In this chapter, an overview of multi-orbital NTNs and their associated services, including various use cases, is discussed. The motivation for the thesis is also presented, along with the research methodology.

Related publication:

[B1] **M. N. Dazhi**, H. Al-Hraishawi, M. R. B. Shankar, S. Chatzinotas, B. Ottersten and H. Muzammil, "Multi-Orbital Non-Terrestrial Networks for Heterogeneous Service Delivery: Architecture, Resource Management, and Use-Cases," *in Muhammad Zeeshan Shakir, Aryan Kaushik*, Non-Terrestrial Networks. London: Elsevier, pp. 1-15, Jan. 2025. (Under review)

Chapter 2

In this chapter, MEO and GEO are analyzed to explore how both can be used simultaneously for resource allocation and management, while accounting for their differing orbital

properties, particularly Doppler effects and packet arrival rates, addressing the problem outlined in **Question 1**. An NTN system is designed with satellites operating in two distinct orbits, supported by algorithms that manage the complexities of varying Doppler effects and propagation delay spreads across the orbits. Additionally, the chapter investigates potential gains from strategic traffic routing across these orbits to optimize network capacity.

Related publication:

[C1] **M. N. Dazhi**, H. Al-Hraishawi, M. R. B. Shankar and S. Chatzinotas, "Uplink Capacity Optimization for High Throughput Satellites using SDN and Multi-Orbital Dual Connectivity," *in 2022 IEEE International Conference on Communications Workshops* (ICC), Seoul, Korea, Republic of, 2022, pp. 544-549, doi: 10.1109/ICCWorkshops53468.2022.9814707.

Chapter 3

In this chapter, different classes of terminals are investigated and designed with reference to the 3GPP Release 15 specifications regarding radio frequency characteristics, addressing the problem indicated in **Question 2**. A resource scheduling architecture is developed that includes a softwarized dispatcher, which identifies and differentiates packet data units (PDUs) based on the unique RF characteristics of either IoT or VSAT devices. This approach facilitates the implementation of scheduling policies that permit allocation restrictions on satellites and optimize capacity using multi-connectivity (MC) across multiple orbital satellites.

The problem, which aims to maximize uplink capacity while reducing energy consumption, is solved using the proposed Terminal-Aware Multi-Connectivity (TAMC) algorithm. This algorithm employs link budget analysis to determine the required Eb/No (C/N) that satisfies the respective LEO, MEO, and GEO links to achieve an acceptable bit error rate for either VSAT or IoT UEs. It then implements a resource allocation policy that allows all UEs to utilize all orbital links, with the exception of IoT devices, which are restricted from using the GEO link due to the high power required to maintain the connection.

This algorithm is implemented through simulations and demonstrates superior performance compared to benchmark approaches in terms of peak data rate, peak delay, and energy efficiency.

Related publications:

[C2] **M. N. Dazhi**, H. Al-Hraishawi, M. R. B. Shankar and S. Chatzinotas, "Terminal-

Aware Multi-Connectivity Scheduler for Uplink Multi-Layer Non-Terrestrial Networks," *2022 IEEE Globecom Workshops (GC Wkshps)*, 2022, pp. 1133-1139, doi: 10.1109/GCWkshps56602.2022.10008521.

Chapter 4

In this chapter, we propose a novel architectural model that addresses **Question 3**, along with a resource allocation approach that tackles **Question 4**. To provide a solution for **Question 3**, we design and implement an architectural model that adopts the Open RAN framework, incorporating radio units, decentralized units, and a centralized unit for the spatial optimization of the gateway, referred to as the Hybrid Gateway Station (HGS). This is achieved by co-locating the feeder functions for LEO, MEO, and GEO orbits under a centralized management system that utilizes a decentralized antenna architecture. Similarly, **Question 4** is approached by considering uplink resource allocation methods that operate for UEs across the categories of URLLC, mMTC, and eMBB, all of which have dynamic QoS and traffic demands. This leads to a non-convex combinatorial problem, which involves maximizing variables such as power and resource allocation indicators. The problem is decoupled into two sub-problems, with the first sub-problem being converted to a convex form and solved using the interior point algorithm. Subsequently, the second sub-problem is addressed using the Hungarian algorithm for path matching. The numerical analysis demonstrates that the proposed method outperforms other state-of-the-art algorithms in terms of uplink capacity, energy efficiency, and delay.

Related publications:

[J1] **M. N. Dazhi**, H. Al-Hraishawi, M. R. B. Shankar, S. Chatzinotas and B. Ottersten, "Energy-Efficient Service-Aware Multi-Connectivity Scheduler for Uplink Multi-Layer Non-Terrestrial Networks," *in IEEE Transactions on Green Communications and Networking*,vol. 7, no. 3, pp. 1326-1341, Sept. 2023, doi: 10.1109/TGCN.2023.3269283.

Chapter 5

This chapter addresses the problem outlined in **Question 5**. In this context, we propose a dynamic beam and resource allocation management technique. A non-convex optimization problem is formulated for a downlink resource management system in a multi-orbital NTN, which involves users with diverse traffic classes, including URLLC, eMBB, and high-definition television (HDTV), all operating under varying channel conditions represented by

the Channel Quality Indicator (CQI). To solve the formulated problem, we decouple it into two sub-problems: (i) dynamic beam allocation and (ii) joint power and bandwidth allocation. The first sub-problem is resolved using an iterative algorithm, while the second sub-problem is addressed through a multi-agent deep reinforcement learning algorithm. Finally, simulation analysis demonstrates that the proposed approach outperforms other benchmark methods in terms of sum rate, spectral efficiency, energy efficiency, and peak delay.

Related publications:

[J2] **M. N. Dazhi**, H. Al-Hraishawi, D. D. Tran, M. R. B. Shankar and S. Chatzinotas, "Multi-Agent DRL-aided Dynamic Beam and Resource Allocation Management in Multi-Tier 6G NTN," *in IEEE Transaction in Wireless Communications*, pp. 1-13, 2024 (Under review).

[C3] **M. N. Dazhi**, H. Al-Hraishawi, M. R. B. Shankar and S. Chatzinotas, "MARL-aided Spectral Efficiency Maximization in Multi-Tier NTN Operating Multi-Connectivity with Different Waveforms for PAYG Service," *in 2024 IEEE 100th Vehicular Technology Conference (VTC2024-Fall), Washington, DC, USA, 2024, pp. 1-7, doi: 10.1109/VTC2024-Fall63153.2024.10757662.*

Chapter 6

In this chapter, the problem of efficiently dimensioning ground and space resources to meet dynamic traffic demands and enhance revenue, as outlined in **Question 6**, is addressed. A novel integrated service model is presented in which infrastructure providers (InPs) lease resources from multi-orbital NTNs as slices to mobile virtual service operators (MVSOs), who then offer these leased resources to subscribers. This model facilitates the efficient utilization of NTN resources within the telecommunications ecosystem. Additionally, a multi-objective optimization problem (MOOP) is formulated, involving two combinatorial objective functions for InPs and MVSOs, aimed at revenue maximization and QoS satisfaction. To solve the MOOP, an algorithm is proposed that addresses the joint requirements of network slicing and admission control (AC) by employing techniques such as the Non-Dominated Sorting Genetic Algorithm II (NSGA-II), multi-objective reinforcement learning (MORL), and a heuristic approach. This algorithm enhances the AC mechanism by leveraging a deep learning algorithm, specifically Long Short-Term Memory (LSTM), to intelligently predict the traffic demands of eMBB and URLLC UEs and thereby prevent SLA violations. The proposed

algorithm outperforms other state-of-the-art algorithms in terms of subscriber satisfaction, URLLC peak delay, and revenue for both MVSOs and InPs.

Related publications:

[J3] **M. N. Dazhi**, H. Al-Hraishawi, M. R. B. Shankar, S. Chatzinotas and J. Grotz, "Joint NTN Slicing and Admission Control for Infrastructure-as-a-Service: A Deep Learning Aided Multi-objective Optimization," *in IEEE Transactions on Cognitive Communications and Networking*, pp. 1-13, 2024, doi: 10.1109/TCCN.2024.3461673

Chapter 7

This chapter presents the main conclusions of the thesis and outlines potential directions for future research.

Chapter 2

Radio Resource Management in Multi-Orbital NTN: Exploiting Orbital Features for Optimization

Dual Connectivity is a key approach to achieving optimization of throughput and latency in heterogeneous networks. Originally a technique introduced by the 3rd Generation Partnership Project (3GPP) for terrestrial communications, it is not been widely explored in satellite systems. In this chapter, Dual Connectivity is implemented in a multi-orbital satellite network, where a network model is developed by employing the diversity gains from Dual Connectivity and Carrier Aggregation for the enhancement of satellite uplink capacity. An introduction of software defined network controller is performed at the network layer coupled with a carefully designed hybrid resource allocation algorithm which is implemented strategically. The algorithm performs optimum dynamic flow control and traffic steering by considering the availability of resources and the channel propagation information of the orbital links to arrive at a resource allocation pattern suitable in enhancing uplink system performance. Simulation results are shown to evaluate the achievable gains in throughput and latency; in addition we provide useful insight in the design of multi-orbital satellite networks with implementable scheduler design.

2.1 Introduction

The rapidly growing demand for high data rate and the accentuated resource scarcity in satellite systems require new paradigms to improve radio resource utilization. Of the many candidate techniques, dual connectivity is a promising solution to increase the achievable throughput of the users by utilizing the available resources in heterogeneous systems [34]. Dual connectivity (DC) can increase the per-user data rate without the need for additional bandwidth resources or substantial hardware complexities [35]. DC has been introduced by the 3rd Generation Partnership Project (3GPP) in terrestrial communication networks in Long Term Evolution- (LTE) specification Release 12 in order to enable two radio access networks to simultaneously serve a single user [36]. The technique of dual connectivity has succeeded to boost the performance of terrestrial networks through maximizing the spectrum utilization and satisfying the extremely high throughput requirements in certain circumstances [37].

The capability of satellite systems in providing ubiquitous coverage and extensive access to support various communication applications from diverse industries makes the traffic demands more heterogeneous and geographically distributed. Thus, it is critical for satellite systems to be flexible and adaptive to such spatio-temporal diversified traffic demands [38], and a resilience in allocating the limited satellite resources is essential to satisfy the uneven demands [39]. In this direction, several important contributions to develop flexible resource allocation methods and capacity enhancement approaches have been proposed. For instance, a dynamic capacity allocation scheme is investigated in [40] by utilizing smart gateway diversity structure to minimize system capacity losses and improve rate matching performance. Additionally, the concept of carrier aggregation (CA) for geostationary orbit (GEO) satellites is also studied in [41] but CA has limitations in the multi-orbit satellite structure. Specifically, in CA all component carriers belong to the same system/orbit but in dual connectivity the aggregated carriers can be from different gateways/orbits.

In this context, channel bonding a concept similar to CA was introduced to the satellite systems in the DVB-S2X standard [42]. Apparently, channel bonding standard has some intrinsic limitations that might restrict the required flexibility in resource allocation. For instance, channel bonding is mainly focusing on grouping carriers across transponders, where these carriers have to be intra-band contiguous. Whereas, dual connectivity allows combining

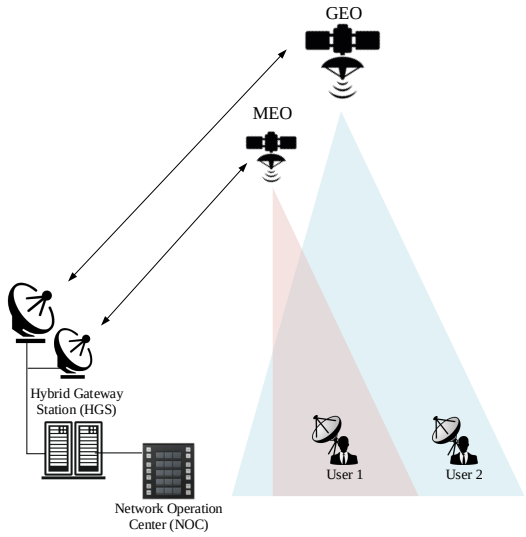

Figure 2.1: Schematic diagram of the considered network topology with inter-orbit dual connectivity.

multiple carriers from different systems in diverse spectrum bands [43]. Having been motivated by the flexibility offered by dual connectivity beyond the state of the art, this work is considering dual connectivity to circumvent these limitations and improve capacity and flexibility in heterogeneous inter-orbit satellite systems.

Furthermore, the uplink transmission from user equipment towards satellites faces significant challenges than downlink due to the transmit power limitation on the user terminals, which ultimately limits the achievable uplink data rate [44]. In particular, GEO satellites are orbiting constantly at a higher altitude than that of non-geostationary (NGSO) satellites, and thus, GEO uplink losses and latency due to signal propagation are both higher, which is detrimental for delay-sensitive applications. Hence dual connectivity would be useful for satellite operators with multi-orbital constellations such as SES.

Contributions: Our key technical contributions can be explicitly summarized as follows:

1. The design guidelines are stated for deploying a multi-orbital geo and medium earth orbit (MEO) satellite network with a hgs serving both GEO and MEO. This includes the introduction of a software defined network controller at the HGS and a software defined radio controller at the ut for the purpose of joint MEO and GEO controlling at the network layer. Focus is placed on MEO for ease of comprehension, this guidelines

can be extended to other NGOS like low earth orbit (LEO) constellation.

2. Hybrid resource allocation algorithm has been developed by taking into consideration the satellite channel conditions and the packet arrival rate of the two orbital satellite constellations to achieve an optimal resource allocation pattern, these resources include spectrum and power.

3. The hybrid network performance was evaluated with analyzed link budget results. The proposed hybrid algorithm was also evaluated with simulations in terms of achievable throughput and delay results that were compared with other state-of-the-art algorithms.

The rest of the chapter is structured as follows. In chapter 2.2, the network model and problem analysis are discussed extensively covering system architecture and the proposed hybrid algorithm. Following that in chapter 2.3, a performance review of the simulation is given, with the various achievable Key Performance Indicators (KPI). Finally in chapter 2.4, the conclusions are outlined with future work areas summarised.

2.2 Network Model and Problem Analysis

The objective of this chapter is to improve the user experience in a satellite communication system by addressing the problems of delay and capacity. In this context, the chapter considers the emerging system with dual connectivity of GEO and MEO, and further aims to offer a network service to minimize latency and maximize throughput.

2.2.1 Description of System Architecture

The system architecture consists of a MEO and GEO satellite connected to a HGS that controls and maintains the links. The HGS is configured with two concatenated antennas, each feeding one of the satellites, and the satellites provide beam coverage over the UT. At the HGS, a gsnjc is configured at the network layer to collect signalling messages on the control plane of both the MEO and GEO links; these messages include packet inter-arrival time, UT DC capability, link signal to noise ratio (SNR), Doppler effect of the satellites and location of the UT. This action is normally handled by a network hub at the gateway, but for the purpose of efficiency and flexibility, Software Defined Network (SDN) controller has been proposed in this architecture to perform these processes. This software controller is a

proposed state-of-the-art network control entity for future satellite architecture. Furthermore, GSNJC schedules UT to transmit the packets to the HGS over the MEO and GEO links as shown in Fig. 2.2.

From the uplink transmitting UT, the Protocol Data Units (PDU) are generated and prepared for transmission at the network layer. The PDU generator forwards the PDUs to the allocation procedure unit in the data link layer, which allocates the PDUs to MEO and GEO paths based on a pattern indicated by the allocation algorithm running in the Unified Software Defined Radio Controller (uSRC). The uSRC is connected to GSJNC over control plane logical link to exchange signalling and optimization information between the UT and the HGS. Whilst the PDU allocation is ongoing at the data link layer of the UT, the PDUs are encapsulated to Generic Stream Encapsulation (GSE) by the encapsulator and then forwarded for base-band framing; subsequently, the Base-band Frames (BBFrame) are transmitted over the satellite channel. At the HGS receiver, they are decapsulated into GSE packets and then reconstructed to PDUs in the data link layer on the MEO and GEO paths. The PDUs from both paths are then aggregated by the traffic merger at the network layer. The following procedure is the PDU integrity check and ordering that are performed with intelligence provided by the GSJNC, which has knowledge of the PDU original order.

The conditions for the hybrid allocation algorithm to be implemented includes:

1. The MEO and GEO satellites must have visibility to the HGS and the UT.
2. The link budget must be satisfied for both MEO and GEO with adequate link margin.
3. Network connectivity requirement in the service level agreement (SLA) must be for at least 24 hours and above.
4. The UT must support DC functionality.

2.2.2 Satellite Link and Channel Model

The satellite is designed with a link budget and air interface that has the capability of mitigating fading in a communication channel, by employing modulation and coding schemes to adapt to the signal-to-noise ratio of the channel. From the Friis equation as described in [45], the received power which is measured in dB, is composed of the summation of the transmitted power (P_T), gain of transmitting antenna (G_T), gain of receiving antenna (G_R)

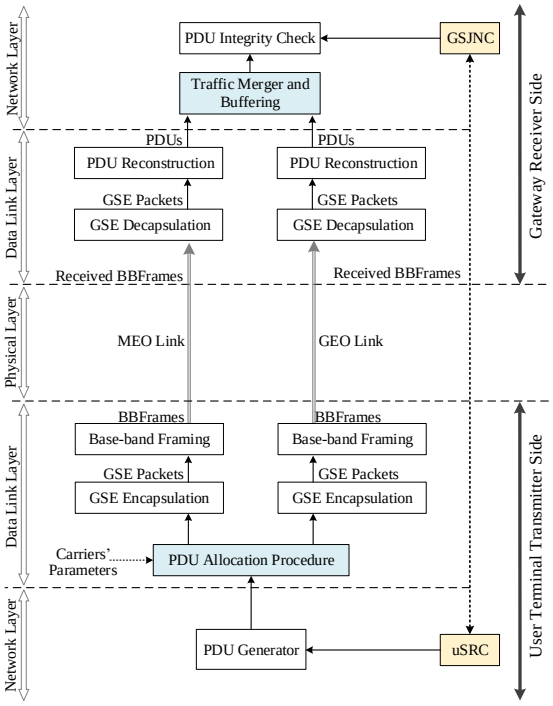

Figure 2.2: System Architecture

and the deductions comprising the free space loss (FSL), atmospheric absorption and other propagation loses. The FSL is presented below in (2.1).

$$FSL = 20\log(\frac{4\pi D}{\lambda}) \tag{2.1}$$

Where D is the propagation distance in meters and λ is the wavelength of the radio frequency also in unit of meters. The SNR at the receiver is obtained to understand the total power degradation in dB. The channel noise is impacted by the assigned channel bandwidth in addition to the antenna thermal noise and other losses. To estimate the communication signal quality and taking into consideration the Friis equation earlier discussed, the energy-per-bit-to-noise ratio (E_b/N_o) which is also SNR normalized to spectral efficiency, is expressed in (2.2).

$$E_b/N_o = EIRP + G_R - FSL - L_{oth} - N_o - 10\log(R_B) \tag{2.2}$$

Where EIRP represents computation of Effective Isotropic Radiated Power which comprises of P_T, and G_T, while L_{oth}, N_o and R_B represent other losses, noise spectral density and bit rate respectively [45]. The impairments in the channel greatly affects the demodulated data at the receiver, and this is seen in the increase of the E_b/N_o required to achieve a

given bit error rate (BER), typically considered around 10^{-6}. The E_b/N_o required to close the link budget with a good margin, is obtained from the air interface which comprises of combinations of modulation and coding schemes.

2.2.3 Problem Analysis

The problem of uplink delay and capacity can be solved by utilizing the two channel paths of GEO and MEO to simultaneously transmit the PDUs from the UT to the HGS. The Poisson arrival process is assumed at the HGS with PDU inter-arrival times of λ_M and λ_G for MEO and GEO respectively. The PDUs that arrive at the HGS through the MEO link were initially transmitted with a probability of P_M, while those over the GEO link were transmitted with a probability of P_G. Hence the corresponding PDU inter-arrival time over the MEO and GEO links is represented as $P_M\lambda_M$ and $P_G\lambda_G$ respectively. The average delay of the hybrid PDUs at HGS is expressed as stated in (3) below [46], with d_{G_i} and d_{M_i} representing delay on the GEO and MEO links respectively, for the i^{th} block of PDUs.

$$\mathbb{E}[d] = \sum_{i=1}^{n} P_{G_i} d_{G_i} + \sum_{i=1}^{n} P_{M_i} d_{M_i} \tag{2.3}$$

The GEO delay can be computed while considering a PDU processing time at the UT and HGS as β_G; similarly β_M is considered as the PDU processing time for MEO. The delay of MEO PDU is expressed as

$$d_{M_i} = \lambda_{M_i} + \beta_{M_i} \tag{2.4}$$

Similarly the delay on the GEO PDU can be given as

$$d_{G_i} = \lambda_{G_i} + \beta_{G_i} \tag{2.5}$$

The probability that a PDU will arrive through the GEO channel can be expressed as

$$P_{G_i} = \frac{\lambda_{M_i}}{\lambda_{G_i}} \tag{2.6}$$

Furthermore, the probability that a PDU will arrive through the MEO channel is

$$P_{M_i} = 1 - P_{G_i} = 1 - \frac{\lambda_{M_i}}{\lambda_{G_i}} \tag{2.7}$$

Substituting (2.4), (2.5), (2.6) and (2.7) into (2.3) will result in the average PDU delay

$$\mathbb{E}[d] = \sum_{i=1}^{n} [\frac{\lambda_{M_i}}{\lambda_{G_i}}[\lambda_{G_i} + \beta_{G_i}] + (1 - \frac{\lambda_{M_i}}{\lambda_{G_i}})[\lambda_{M_i} + \beta_{M_i}]] \tag{2.8}$$

Subject to:

$$\mathbb{C}_1 : 0 < \lambda_{M_i} < \lambda_{G_i} \ \forall i \in N, i = 1, ..., n$$

$$\mathbb{C}_2 : min(\lambda_{G_i}, \lambda_{M_i}) < \infty \ \ \forall i \in N, i = 1, ..., n$$

$$\mathbb{C}_3 : P_{G_i} = \frac{\lambda_{M_i}}{\lambda_{G_i}} > 0 \ \ \forall i \in N, i = 1, ..., n$$

$$\mathbb{C}_4 : P_{M_i} = 1 - \frac{\lambda_{M_i}}{\lambda_{G_i}} > 0 \ \forall i \in N, i = 1, ..., n$$

Following appropriate scheduling of the PDUs on the two channel paths at the UT, the MEO and GEO PDUs that arrive the HGS at the same time will be aggregated at the traffic merger, thereby optimizing throughput by increasing the bandwidths. Throughput at HGS can be expressed using the Shannon capacity for a noisy channel. The SNR will be obtained from the link budget, and then the combined capacity of the hybrid system for both MEO and GEO bandwidths can be expressed as an aggregated capacity (H_C). Here B_G, B_M, SNR_G and SNR_M are the GEO bandwidth (in MHz), MEO bandwidth (in MHz), GEO link SNR (dB) and MEO link SNR (dB) respectively.

$$\begin{aligned} H_C(Mbps) \ = \ & \sum_{i=1}^{n} P_{G_i}[B_G \log_2(1 + SNR_{G_i})]) \\ & + \sum_{i=1}^{n} P_{M_i}[B_M \log_2(1 + SNR_{M_i})] \end{aligned} \tag{2.9}$$

Subject to C_1, C_2, C_3, C_4 and C_5 for DC.

$$\mathbb{C}_5 : SNR_{M_i} \geq SNR_{G_i} \quad \forall i \in N, i = 1, ..., n,$$

2.2.4 Proposed Resource Allocation Algorithm

The hybrid resource allocation (HRA) algorithm is proposed in Algorithm 1 to optimize the GEO delay and throughput by activating DC with the addition of a MEO link that has a

limited visibility period due to the lower altitude. As discussed earlier, the GSNJC collects the signalling measurements of the MEO and GEO links, it evaluates if the conditions for DC are met and then instructs the uSRC to implement the uplink DC optimization with a defined pattern of the resource allocation in the hybrid algorithm 1. The objective of the algorithm is to connect the fixed UT to MEO and GEO links for uplink transmission and the algorithm is periodically executed to take into consideration the current values of the input variables. The inputs to the algorithm include PDU inter-arrival time, Doppler shift and SNR for intelligent decision making. The first phase of the algorithm is to generate the carrier allocation sequence for both GEO and MEO using (6) and (7) respectively. Once the allocation sequence is obtained, the vectors C_1 and C_2 are combined and saved as M, which allows for the aggregation of the PDUs over the dual connected links. The next phase in the algorithm is the decision process for the carrier allocation implementation; this phase utilizes the inputs mentioned earlier to effect the implementation decision. The algorithm considers the three variables to make a cascaded decision flow. If the MEO PDU inter-arrival time is less than that of GEO, and if the MEO SNR and Doppler shift are greater or equal to that of GEO, the decision is to implement DC with the M allocation sequence, else the algorithm will revert to a single carrier mode on C_1 (GEO).

2.3 Performance Evaluation

In this chapter, the simulation system is setup with defined parameters. The simulation results are also discussed to evaluate the performance of the system architecture and the proposed hybrid allocation algorithm.

2.3.1 System Simulation Setup

In Table 2.1, the link budget and parameters are shown for both MEO and GEO links, DVBS2X is used as the air interface. The GEO satellite is set at an altitude of 35,786 km, while MEO was simulated to operate at 8,000 km from the earth surface using STK 12.4. The results of the Eb/No in dB from the link budget can be seen in Fig 2.3. It is observed that MEO has 12 instances of link closure (with assumed 8 hours total link visibility time in a 24 hours period), while GEO has a steady link closure trend for a period of 24 hours. Based on the uniqueness of the MEO channel, which has a lower altitude from the earth surface compared to GEO, the satellite moves away and returns to the UT location with different

Algorithm 1: Hybrid Resource Allocation

Input: λ_M = MEO PDU Inter-arrival Time
λ_G = GEO PDU Inter-arrival Time
α = Total blocks of PDUs
D_M = MEO Doppler Shift
D_G = GEO Doppler Shift
SNR_G = GEO SNR
SNR_M = MEO SNR
$i = 1$

```
while i ≤ α do
    Generate Carrier Allocation Sequence
    **For GEO Carrier**
    C1 = λ_Mi / λ_Gi from (6)
    **For MEO Carrier**
    C2 = (1 − λ_Mi / λ_Gi) from (7)
    Combine both vectors and store Carrier Allocation Sequence in M
    M = [C1, C2]
    Implement Carrier Allocation
    if λ_M < λ_G then
        if SNR_M ≥ SNR_G then
            if D_M ≥ D_G then
                Implement DC with M = [C1,C2]
            else
                Activate Single Carrier mode on C1
            end
        else
            Activate Single Carrier mode on C1
        end
    else
        Activate Single Carrier mode on C1
    end
end
```

Doppler shift values. Hence the Doppler shift of the satellite in KHz is shown in Fig 2.4. Furthermore in Fig. 2.5, the PDU inter-arrival time for MEO and GEO is derived from the propagation delay of the STK simulation, it can be seen that MEO varies between 0.005s to 0.016s, while GEO is between 0.98s to 0.117s. Hence the (approximate) average PDU inter-arrival time for MEO and GEO is further obtained as 11ms and 108ms respectively.

Table 2.1: Link Parameters

Parameters	MEO	GEO
Satellite Altitude (Km)	8,000	35,786
UT Latitude (Degrees)	11.92	11.92
UT Longitude (Degrees)	77.69	77.69
Gateway Latitude (Degrees)	1.44	1.44
Gateway Longitude (Degrees)	38.43	38.43
Flux Density (dBW/m^2)	-106.86	-120.77
Carrier Frequency (GHz)	14	14
Waveform	DVBS2X	DVBS2X
Free Space Loss (dB)	184	205
Carrier Bandwidth (MHz)	50	50
EIRP (dBW)	33.73	39.73

2.3.2 System Performance Evaluation

In Fig. 2.6, the delay of the HRA is evaluated with comparison to the round robin (RR) scheduler, a load-balancing (LB) scheduler in [47] and the single GEO carrier. The delay result in ms is plotted against the number of transmitted PDUs. The HRA was implemented by defining the parameters in (2.8), including parameters like PDU inter-arrival time which was obtained from the average of the inter-arrival time of MEO (11 ms) and that of GEO (108 ms) as explained in chapter 2.3.1. Likewise the probability to transmit over either MEO or GEO was formulated as in (2.7) and (2.8) then inserted into the algorithm. The probability is a function of the inter-arrival time and for this simulation, P_G was 1/9 and P_M was 8/9; this indicates that during any transmission instance, 8 out of 9 PDUs will be transmitted over the MEO channel while the remaining PDU will be transmitted over the GEO channel using the HRA. The RR scheduler utilizes the PDU transmission allocation weighting of 50% PDUs transmitted over MEO and the remaining 50% will be sent over the GEO channel. For load-balancing scheduler, it allocates PDUs on a weighting factor of 67% on the carrier with the best SNR, and in this model that will be the MEO carrier, while the remaining 33% on the GEO carrier. In HRA, the weighting is defined so that 89% of the PDUs are transmitted using MEO and the remaining 11% over the GEO channel. By so doing, the algorithm

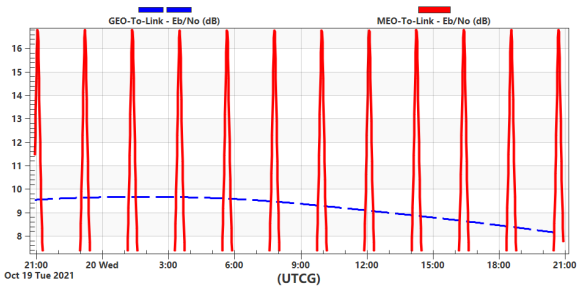

Figure 2.3: A comparison between Eb/No of MEO and GEO Links verses Time.

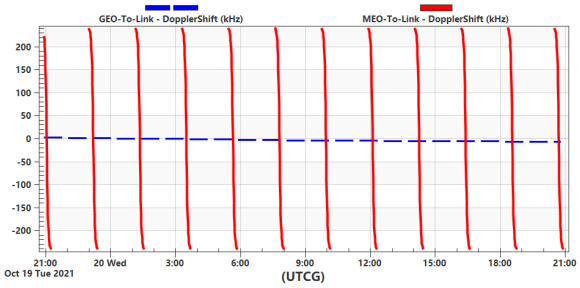

Figure 2.4: A comparison between Doppler Shift of MEO and GEO Links verses Time.

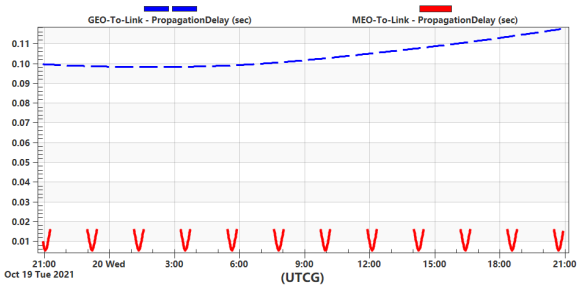

Figure 2.5: A comparison between PDU Inter-arrival Time (delay) of MEO and GEO Links verses Time.

leverages the lower delay on MEO over GEO to achieve a better performance compared to RR and LB. The result of transmitting 10,000 PDUs is that the delay on the single GEO carrier, RR and LB are 1,079 ms, 594 ms and 432 ms respectively, while the HRA yields a delay of 208 ms as shown in Fig. 2.6. This shows HRA has a delay performance gain that is 70%, 96% and 135% less than LB, RR and single GEO carrier respectively.

The peak data rate was obtained for the GEO and the aggregated carriers using (2.9). The carrier bandwidth used for both MEO and GEO was 50MHz, and the SNR was obtained from the link Eb/No simulations in chapter 2.3.1. In Fig. 2.7, the peak data rate is plotted against SNR, and it is observed that the achievable peak data rate for the RR, LB and HRA are 155 Mbps, 168 Mbps and 186 Mbps respectively. Again HRA shows an improvement of approximately 18% and 10% over RR and LB scheduler respectively. However at very low SNR values, LB and RR have better throughput performance than HRA.

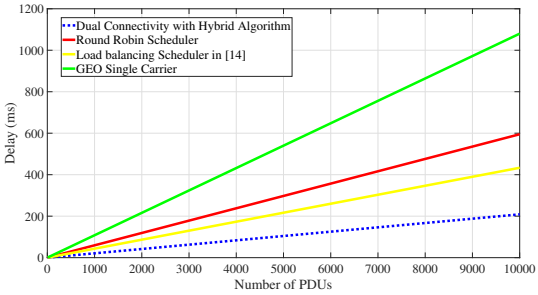

Figure 2.6: Delay verses number of PDUs.

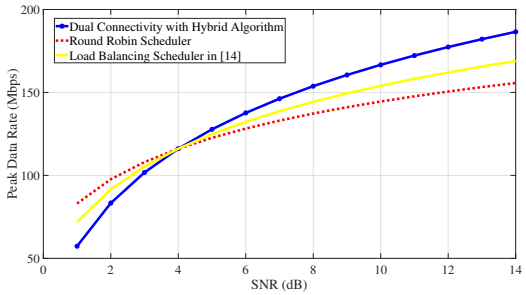

Figure 2.7: Uplink peak data rate verses SNR.

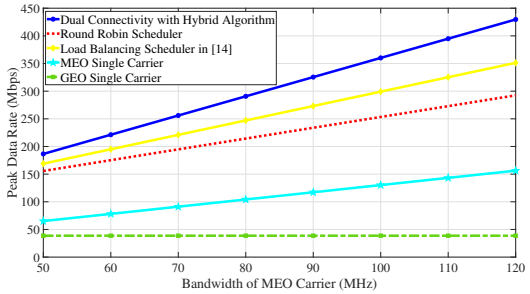

Figure 2.8: Uplink peak data rate verses MEO carrier bandwidth.

In Fig. 2.8, the achievable peak data rate is evaluated for the various schedulers and algorithms while increasing the bandwidth of the MEO carrier to a maximum of 120 MHz. The result obtained shows the RR, LB and HRA yielded 292 Mbps, 351 Mbps and 429 Mbps respectively in peak data rate. This reveals that HRA out performs RR and LB schedulers by 38% and 20% respectively; hence it is more superior in achieving higher KPI values.

2.4 Conclusions

In this chapter, the uplink throughput and delay of a satellite network is optimized using DC technique and aggregating the two carriers involved. A network architecture was designed for a multi-orbital satellite system, where the diversity gains of CA was employed at higher layers, with a software defined network controller at the network layer performing dynamic resource allocation. The hybrid resource allocation algorithm operates at the controller performing optimum dynamic flow control and traffic steering by considering the availability of

resources and the channel propagation information of the orbital links to define the resource allocation pattern in enhancing uplink system performance. The designed hybrid resource allocation algorithm outperformed the single GEO carrier, traditional RR scheduler and the LB scheduler by 135%, 96% and 70% respectively in the average delay performance. Similarly, the peak data rate achieved on the HRA showed improvements of 18% and 10% above RR and LB respectively, when both MEO and GEO carriers are configured with same bandwidth of 50 MHz. Even when the MEO carrier bandwidth was increased to 120 MHz, the HRA outperformed both RR and LB by 38% and 20% respectively. In addition, the proposed multi-orbital architecture showed through simulations improvement over a single GEO satellite network in delay and throughput KPIs.

A future research component that can be explored includes evaluating different service types with varying QoS requirements that is designed in a network slicing architecture with traffic routing algorithms to meet the dynamic service requirement. Another future research area is the design of an energy efficient scheduler, that will ensure energy conservation for the UT.

Chapter 3

User-Terminal-Centric Radio Resource Management Techniques in Multi-Orbital NTN

This chapter introduces the concept of multi-connectivity (MC) to the multi-orbit non-terrestrial networks (NTNs), where user terminals can be served by more than one satellite to achieve higher peak throughput. MC is a technique initially introduced by the 3rd Generation Partnership Project (3GPP) for terrestrial communications in 4G and 5G, it has shown much gain in the terrestrial domain and this chapter explores areas where this concept can benefit the satellite domain. MC can increase throughput, but this entails increased power consumption at user terminal for uplink transmissions. The energy efficiency of uplink communications can be improved by designing efficient scheduling schemes, and to this end, we developed a terminal aware multi-connectivity scheduling algorithm. This proposed algorithm uses the available radio resources and propagation information to intelligently define a dynamic resource allocation pattern, that optimally routes traffic so as to maximize uplink data rate while minimizing the energy consumption at the UT. The algorithm operates with the terminal differentiating multi-layer NTN resource scheduling architecture, which has a softwarized dispatcher at the network layer that classifies and differentiates the packets based on terminal type. The performance of the proposed algorithm was compared with round robin and joint carrier schedulers in terms of uplink data rate and energy efficiency. We also provide architectural design of implementable schedulers for multi-orbital satellite networks that can operate with different classes of terminals.

3.1 Introduction

Satellite communications industry is on the verge of a major transformation due to the paradigm shift brought about by several key technological advancements such as software-defined satellites, very high throughput satellites (VHTS), non-geostationary orbit (NGSO) systems, virtualization and service orchestration [48]. Specifically, the recent developments are primarily focusing on deploying reconfigurable satellite payloads in order to offer generic and software-based solutions as well as to provide high throughput transmissions [49]. In addition to the established satellite applications like aeronautical, maritime, mapping, weather forecasting, and broadcasting, the recent advances have unlocked the satellite potentials to convey and execute various innovative use cases and new services from space [50]. Accordingly, satellite traffic demand is currently growing rapidly for provisioning affordable, accessible, uninterrupted wireless connectivity especially to the underserved and unserved areas. However, satellite resources are still scarce and usually expensive particularly in terms of the radio frequency (RF) spectrum [51]. Therefore, it is crucial to devise unconventional techniques to improve resource utilization while satisfying the high data rate and low latency requirements.

In this direction, an intriguing concept has been recently studied within the multi-beam satellite architectures, that is dual connectivity (DC), which allows users to be simultaneously served with different systems and/or frequency bands [1]. Before that, the DC feature has been considered by the 3rd Generation Partnership Project (3GPP) in Release 12 for adoption to the fifth-generation (5G) New Radio (NR) specifications owing to its capability of maximizing the spectrum utilization and avoiding the traffic overload [36]. Likewise, the 3GPP group has been lately codifying the use of satellites and aerial platforms to construct multi-layer non-terrestrial networks (NTNs) in order to provide space-based 5G communication services and support future wireless ecosystems [52]. Thus, it is essential to extend the concept of DC to multi-connectivity (MC) to adapt to the flexibility and scalability offered by the emerging NTN architectures and the integrated space-aerial-terrestrial networks [53, 54].

The MC techniques are envisioned as an indispensable technology to significantly enhance the offered system capacity and improve the spectral efficiency in the heterogeneous networks. An important foreseeable application of MC is the interworking among various communication standards and architectures through allowing a smoother transition, e.g., between fourth

generation (4G) and 5G systems [55]. The MC solution achieves not only higher per-user data rate but also provides mobility robustness, and thus, it can improve the resilience of wireless communications [56]. Additionally, data traffic in NTNs is vastly diversified and randomly distributed in the serving areas, and coming from various users with different quality-of-service (QoS) requirements [57]. Thus, employing MC in NTNs would help satisfying the asymmetry and heterogeneity of the traffic demands. However, when MC user terminals utilize multiple aggregated carriers/systems that inevitably comes at the cost of higher power consumption [12]. Further, the energy efficiency in NTNs is one of the major challenges, especially for the uplink transmissions and for the battery-limited mobile terminals [58].

In the literature, some contributions have studied and evaluated the issue of energy efficiency for the uplink transmissions in satellite domain. For instance, the energy resource allocation problem in the uplink communications is investigated in [59] within the space-air-ground Internet of remote things networks, which aims at maximizing the system energy efficiency by jointly optimizing sub-channel selection and uplink transmission power control. In [60], a joint optimization model of spectrum efficiency and energy efficiency in a single-station multi-satellite MIMO system has been proposed based on a knee-point driven optimization algorithm. Further, a spatial group based optimal uplink power control scheme is proposed in [61] for enhancing the performance of random access in satellite networks. Additionally, two optimal power control schemes are proposed in [62] for maximizing both delay-limited capacity and outage capacity in cognitive satellite terrestrial networks, which are useful performance indicators for real-time applications. It is worth noting that the aforementioned works [59–62] do not consider concurrent aggregating multi-orbit scenarios in optimizing the uplink transmit power for satellite users.

Nevertheless, the MC promising performance enhancements in throughput and latency have motivated this work to further investigate the uplink energy efficiency issue from a user terminal standpoint. To the best of our knowledge, enhancement of the uplink transmit power has not been studied yet in the open literature within MC enabled multi-orbit NTNs.

Contributions: Our key technical contributions can be explicitly summarized as follows:

1. The design guidelines are outlined for the deployment of a multi-layer satellite network comprising of GEO, MEO and LEO satellites, which are all served by a multi-orbital hybrid gateway station (HGS) [1]. This gateway station functions with a softwarized

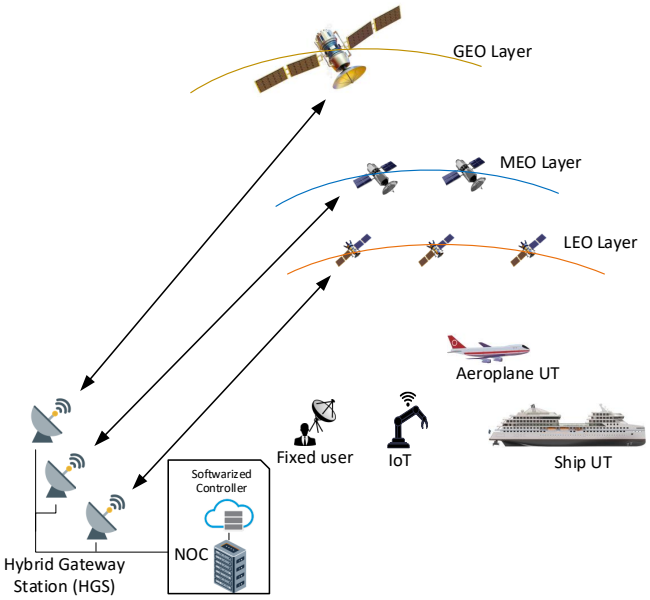

Figure 3.1: Schematic diagram of the considered network topology of the Multi-layer NTN.

controller at the network layer, which performs functions including the classification and dispatching of PDUs onto different queues based on the terminal type of the transmitting user.

2. A terminal aware multi-connectivity (TAMC) scheduling algorithm has been developed, it considers the some radio parameters such as carrier-to-noise ratio (C/N) and the energy-per-bit-to-noise ratio (E_b/N_o) of the three satellite links. These information are required so as to achieve a resource allocation ratio that will allow for optimal resource allocation involving power and spectrum leading to a high capacity transmission with energy efficiency in the uplink.

3. The terminal aware multi-connectivity scheduler was designed based on 3GPP specification along with link budget analysis. The proposed algorithm was then compared numerically with other state-of-the-art algorithms in terms of throughput and energy efficiency.

The rest of the chapter is structured as follows. In chapter 3.2, the network model and architecture is discussed extensively along with the problem analysis. Chapter 3.3 then focuses on the resource scheduling algorithms, while the simulation setup and performance evaluation are covered in chapter 3.4. Finally, the conclusion and future work are summarised

in chapter 3.5.

3.2 Network Model and System Architecture

3.2.1 Description of Topology and Architecture

The system topology consists of the three constellation of LEO, MEO and GEO satellites; a HGS controls the communication to these satellites through multiple inter-connected antenna ports, as shown in Fig. 3.1. The corresponding satellites then configure beams which provide coverage to different types of UTs, comprising fixed terrestrial, maritime, aeronautical, land-mobile and IoT type of UTs. The HGS is configured with a softwarized controller operating at the network layer, which performs the classification and dispatch of protocol data units (PDUs) onto different queues based on the user terminal type. This action allows the scheduling algorithm work efficiently and with high flexibility in optimizing the network KPIs.

The architecture of the radio scheduler (R/S) involves a queuing system which admits PDUs of UTs, each following a Markovian arrival process with arrival rate λ. The HGS will allocate various resource blocks (RBs) on different component carriers (CCs) of the three orbital satellites of LEO, MEO and GEO for uplink transmission, so that the UT can transmit the PDUs on the CCs. Figs. 3.2 and 3.3 show the architectures of the various types of schedulers that are considered in this chapter, details of which are deferred to Chapter 3.3. The scheduling algorithm is executed in the R/S unit, and it implements the resource allocation process based on input radio link parameters including C/N and the E_b/N_o along with the information of the type of uplink UT. For this chapter, the proposed uplink scheduling is achieved through the TAMC algorithm, and the types of terminals considered are the very small aperture terminal (VSAT) and internet of things (IoT) terminals as specified by 3GPP release 15 [52].

The conditions below have to be satisfied for the TAMC algorithm to perform the flexible resource allocation action.

- There must be sufficient E_b/N_o value to close the link budget for the LEO, MEO and GEO satellite links.
- The LEO, MEO and GEO satellites must have visibility at the HGS and at the con-

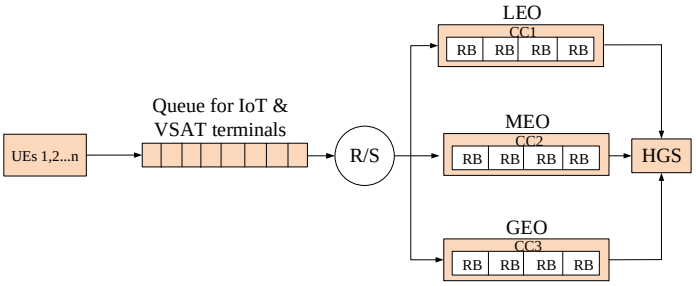

Figure 3.2: Joint multi-layer NTN resource scheduling architecture where JC scheduler will run in R/S

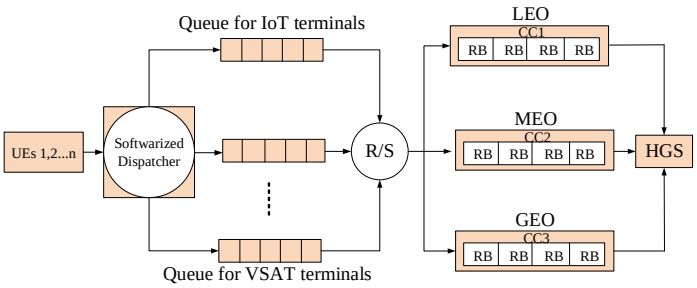

Figure 3.3: Terminal differentiating multi-layer NTN resource scheduling architecture where TAMC or RR schedulers will run in R/S

sidered UT. In addition, the UT should be capable of connecting to the three orbital constellations [63].

- The UT must be capable of providing the HGS with a unique terminal identifier, which will allow the softwarized dispatcher differentiate the UTs.

3.2.2 Uplink Transmission and Channel Model

The uplink transmission in a satellite network starts from the UT to the satellite in space through the radio channel, then down to the gateway station which connects to the network operation center (NOC) and the core network (CN). The satellite network is designed with a link budget and an air-interface that accounts for the power and gains required to achieve a successful transmission over a radio channel. The Free Space Loss (FSL) constitutes a significant reduction in power and takes the form,

$$FSL = 20\log(\frac{4\pi D}{\lambda}) \tag{3.1}$$

where λ is the wavelength of the radio frequency in meters and D is the propagation distance in meters. E_b/N_o is a figure of merit obtained at the receiver to ascertain the signal strength after transmission over a noisy channel and the impact of other contributing loss factors such as pointing and atmospheric losses. The radio air-interface is designed to be robust with sufficient E_b/N_o to mitigate losses in the satellite network, so as to achieve a low bit error rate (e.g. of the order of 10^{-6} and lower); this is done by employing advanced modulation and coding schemes. E_b/N_o is expressed in dB (3.2) [45] [64].

$$E_b/N_o = P_t + G_t + G_r - K - T_s - FSL - L_o - R \tag{3.2}$$

where P_t, G_t, G_r, L_o, T_s, K and R are transmit power, transmitter gain, receiver gain, other losses, receiver system noise temperature, Boltzmann constant and data rate in bits per second.

The E_b/N_o value can also be expressed as signal-to-noise ratio (SNR) normalised to spectral efficiency as shown in (3.3), where BW is bandwidth [64].

$$SNR = \frac{E_b}{N_o}\frac{R}{BW} \tag{3.3}$$

The radio channel is modelled as a Ricean distribution where the multipath fading has a dominant line of sight (LoS) along with some non-LoS components as indicated in [65], and (3.4) represents the probability density function of the Rician channel, with k being the $K-$factor of Rician distribution depicting the power ratio of the LoS and non-LoS components, Z being the signal power and I_0 denoting the Bessel function of the zeroth order.

$$P_{Rician}(Z) = k.e^{[-k(Z+1)]}I_0(2k\sqrt{Z}) \tag{3.4}$$

3.2.3 The Queuing Model

This system can be modelled as a $M/M/c$-PS queue with processor sharing (PS), where the first M represents the Markovian Poisson arrival and the second M stands for exponentially distributed service time, having c servers [66]. The UTs transmits the PDUs, which arrive the radio access network in a Markovian arrival process with arrival rate of λ, and the service time for PDU processing at the server is represented as μ. Hence the load of the system is given as $\rho = \frac{\lambda}{c.\mu}$ [67].

3.2.4 User Terminal

Two classes of terminals are considered in this chapter; the IoT and VSAT terminals which are specified by 3GPP with design parameters outlined in Tables 3.1. The network model, permits for a multi-orbital terminal device, that allows for a single UT to be able to establish multiple connections with satellites of different orbits. Nonetheless, the model also accommodates the installation of multiple antennas at the UT or premises especially for the VSAT scenario, in order to track multi-orbital satellites.

Table 3.1: Link Parameters Specified by 3GPP Release 15 and 16 [52] [68]

Parameters	LEO (VSAT)	LEO (IoT)	MEO (VSAT)	MEO (IoT)	GEO (VSAT)	GEO (IoT)
Satellite Altitude (Km)	1,500	1,500	10,000	10,000	35,786	35,786
Satellite G/T (dB/K)	13	1.1	20**	10**	28	19
UL Carrier Frequency (GHz)	30	2	30	2	30	2
Terminal speed (Km/hr)	upto 1,000km/hr	upto 1,000km/hr	upto 1,000km/hr	upto 1,000km/hr	upto 1,000km/hr	upto 1,000km/hr
One way propagation delay (ms)	25.83	25.83	95.19	95.19	272.37	272.37
UT Tx Gain (dBi)	43.2	8**	43.2	8**	43.2	8**
UT Transmit power (W)	2	6.2**	2	6.2**	2	6.2**
UT Transmit power (dBW)	3.01*	7.92*	3.01*	7.92*	3.01*	7.92*
Free Space Loss (dB)	185.51*	161.99*	201.99*	178.47*	213.06*	189.54*
Uplink C/N (dB)	23.31*	4.64*	13.82*	-2.94*	10.75*	-5.01*
Available EbNo (dB)	27.28*	8.64*	17.8*	1.04*	14.73*	-1.03*
* Derived **Assumed values						

3.2.5 Problem Analysis

The capacity enhancement is a non-convex linear optimization problem and a solution lies in the aggregation of the capacity (C) of the CCs of the LEO, MEO and GEO satellites, a technique known as MC.

$$C = BW \log_2(1 + SNR) \tag{3.5}$$

The average data rate can be expressed as

$$R = J.C \tag{3.6}$$

where J is the number of CCs.

In addition, the maximization of energy efficiency in the uplink for the UTs is also an important metric. The energy efficiency in bits-per-Joules (b/J) is given in (3.7) [69].

$$E = \frac{R}{P(R)} \tag{3.7}$$

where $P(R)$ is the transmission power needed to achieve a data rate of R.

3.3 Resource Scheduling Schemes

This Chapter discusses the three schedulers used in the chapter namely the joint carrier (JC), round robin (RR) and the TAMC schedulers. For the ease of presentation, one satellite is assumed per constellation.

3.3.1 Joint Carrier Scheduler

The joint carrier (JC) scheduler in [69] operates with the scheduling architecture illustrated in Fig. 3.2. PDUs for both IoT and VSAT terminals arrive at a single queue to the R/S unit successively, where the first PDU (irrespective of the terminal type) is allocated to the RB of the CCs of appropriate satellites on the three orbits simultaneously. Subsequently, the next PDU of another UT on queue is scheduled also on the RB of all three orbital satellite CCs at once.

3.3.2 Round Robin Allocation Scheduler

The round robin (RR) scheduler operates with the scheduling architecture illustrated in Fig. 3.3. The architecture operates first by implementing the classification and differentiation of PDUs based on terminal type at the softwarized dispatcher. The dispatcher accepts the PDUs as input along with the identity (ID) of the transmitting UT, either IoT or VSAT. It then classifies the PDUs as IoT or VSAT, and then dispatch them in different queues based on their transmitting terminal IDs. At the R/S, the RR scheduler functions by allocating three different PDUs of the IoT and VSAT terminals successively, on the RB of each of the CCs of the three orbital satellites using the RR mechanism in [1].

$$\alpha'_{TL} = \frac{\frac{C/N_{TL}}{C/N_{TL}+C/N_{TM}+C/N_{TG}}}{(\frac{C/N_{TL}}{C/N_{TL}+C/N_{TM}+C/N_{TG}}) + (\frac{C/N_{VL}}{C/N_{VL}+C/N_{VM}+C/N_{VG}})} \tag{3.8}$$

3.3.3 Terminal-Aware Multi-connectivity Scheduler

The TAMC scheduler functions with the scheduling architecture shown in Fig. 3.3. When the PDUs arrive the R/S unit on different queues for IoT and VSAT, they are scheduled using the TAMC scheduler shown in Algorithm 1. TAMC requires E_b/N_o values of the three orbital satellites LEO, MEO and GEO, including the C/N of terminals with serving

$$\alpha'_{VL} = \frac{\frac{C/N_{VL}}{C/N_{VL}+C/N_{VM}+C/N_{VG}}}{(\frac{C/N_{VL}}{C/N_{VL}+C/N_{VM}+C/N_{VG}}) + (\frac{C/N_{TL}}{C/N_{TL}+C/N_{TM}+C/N_{TG}})} \tag{3.9}$$

$$\alpha_{TL} = \frac{\alpha'_{TL}}{\alpha'_{TL} + \alpha'_{TM} + \alpha'_{TG} + \alpha'_{VL} + \alpha'_{VM} + \alpha'_{VG}} \tag{3.10}$$

$$\alpha_L = \{\alpha_{TL}, \alpha_{VL}\} \tag{3.11}$$

$$\alpha_M = \{\alpha_{TM}, \alpha_{VM}\} \tag{3.12}$$

$$\alpha_G = \{\alpha_{TG}, \alpha_{VG}\} \tag{3.13}$$

* It should be noted that $0 \leq \alpha_{ik} \leq 1$, where i represents the UT of IoT (T) or VSAT (V); k represents orbital satellite links of LEO (L), MEO (M) or GEO (G). The same notation applies to C/N_{ik}.

satellite links. The TAMC algorithm uses the C/N inputs to arrive at a proportionality factor α and it is derived in equations (8) to (13), with which the RBs and CCs of the serving orbital satellites are allocated for both IoT and VSAT terminals, in a heuristic way driven by maximizing uplink capacity as well as enhancing energy efficiency. Once the proportionality factors are obtained, the TAMC algorithm will store the resource allocation sequence in a vector w having the dimension of available resources i.e, CCs, RBs and satellites where an entry 1 indicates the allocation of that resource. Then it will check the E_b/N_o values of all the links for the different terminals with the serving satellites of LEO, MEO and GEO to ascertain these values are above the QoS threshold, so as to implement the multi-connectivity optimization. In the absence of a beneficial scenario, the TAMC algorithm will revert to DC or a single carrier mode on the favorable satellite link.

The considered approach to improving data rate and enhancing energy utilization can further be achieved by proportionality factors (α), with which the different satellite orbital CCs can be aggregated in a multi-connected transmission scenario. These weights are a function of the C/N of the respective transmitting VSAT or IoT terminals of the serving orbital satellite. In particular, α_{TL}, α_{TM}, α_{TG}, α_{VL}, α_{VM} and α_{VG} in equations (11) to (13) are weights for IoT on LEO carrier, IoT on MEO carrier, IoT on GEO carrier, VSAT on LEO carrier, VSAT on MEO carrier and VSAT on GEO carrier respectively. While C/N_{TL}, C/N_{TM}, C/N_{TG}, C/N_{VL}, C/N_{VM} and C/N_{VG} are the IoT C/N on LEO CC, IoT C/N on MEO CC, IoT C/N on GEO CC, VSAT C/N on LEO CC, VSAT C/N on MEO CC and VSAT C/N on GEO CC respectively. Furthermore, α_L, α_M and α_G represents weights of LEO, MEO and GEO carriers respectively as can be seen in (3.8) to (13). Accordingly, the

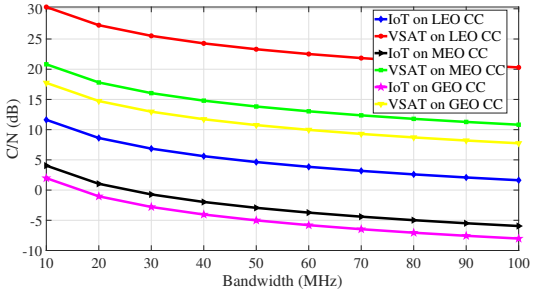

Figure 3.4: C/N verses Bandwidth.

scheduler aims at maximizing the below expression.

$$\sum_{i=1}^{I}(\alpha_{iL}R_{iL} + \alpha_{Mi}R_{iM} + \alpha_{iG}R_{iG}) \ \forall i \in I \tag{3.14}$$

R_{ik} is the data rate of i UT for k orbital satellite links of LEO (L), MEO (M), GEO (G) and (3.14) is subject to:

$$\mathbb{C}1 : min(E_b/N_{oL}, E_b/N_{oM}, E_b/N_{oG}) > \eta \ \ \forall i \in I$$

$$\mathbb{C}2 : E_i \geq \alpha_i \phi_{max} \ \ \forall i \in I$$

where η is a E_b/N_o threshold value, and E_i is the energy efficiency of UT_i with ϕ_{max} as the maximum transmit power utilization. Further mathematical treatment of this optimization problem will be performed in the future.

3.4 Performance Evaluation

3.4.1 Simulation Setup

The simulation was setup with a link budget analysis using parameters outlined in Table 3.1. The value of C/N at 50 MHz from Fig. 3.4, is used in deriving α, and for ease of presentation, the same frequency band is used across all orbital layers. MATLAB was used to simulate the performance of the proposed algorithm while comparing other state-of-the-art algorithms.

Algorithm 2: Terminal-aware Multi-Connectivity

Input:

Eb/No_L = LEO Eb/No
Eb/No_M = MEO Eb/No
Eb/No_G = GEO Eb/No
C/N_{T_L} = IoT C/N on LEO
C/N_{T_M} = IoT C/N on MEO
C/N_{T_G} = IoT C/N on GEO
C/N_{V_L} = VSAT C/N on LEO
C/N_{V_M} = VSAT C/N on MEO
C/N_{V_G} = VSAT C/N on GEO
Q_{LT} = Length of IoT PDU queue
Q_{LV} = Length of VSAT PDU queue
$\sigma = Q_{LT} + Q_{LV}$
$\eta = E_b/N_o$ Threshold
$j = 1$

Carrier allocation ratio
LEO Carrier == α_L from (11)
MEO Carrier == α_M from (12)
GEO Carrier == α_G from (13)
Computing the multi-carrier allocation Sequence as w
$w = (\alpha_L, \alpha_M, \alpha_G)$
Carrier Allocation Implementation
while $j \leq \sigma$ **do**
  if E_b/N_{oG} *and* E_b/N_{oM} *and* $E_b/N_{oL} > \eta$ **then**
    Implement MC with w
  else
  Switch to single carrier mode on any available carrier
  if E_b/N_{oG} *and* $E_b/N_{oM} > \eta$ **then**
    Implement DC with IoT on MEO CC; VSAT on both GEO and MEO CC
  else
  Switch to single carrier mode on any available carrier
  if E_b/N_{oG} *and* $E_b/N_{oL} > \eta$ **then**
    Implement DC with IoT on LEO CC; VSAT on both GEO and LEO CC
  else
  Switch to single carrier mode on any available carrier
  if E_b/N_{oM} *and* $E_b/N_{oL} > \eta$ **then**
    Implement DC with IoT and VSAT on both MEO and GEO CCs
  else
  Switch to single carrier mode on any available carrier
end

3.4.2 Performance Analysis

The objective is to enhance the uplink capacity by implementing multi-connectivity, whilst reducing the energy utilization for the two classes of terminals using the TAMC scheduler. To optimize the uplink capacity along with energy efficiency in a heuristic way, the TAMC algorithm defines α using (3.8) to (13), such that (α_{TL}, α_{VL}, α_{TM}, α_{VM}, α_{VG}, α_{TG}) = (0.17, 0.17, 0.20, 0.13, 0.33, 0); α_{TG} is made 0 because of the low E_b/N_o value of -1.03 dB which cannot close the link, hence IoT terminals will not be scheduled on GEO CC by this scheduling algorithm. The RR will schedule IoT on MEO CC, VSAT on LEO CC and IoT on GEO CC per time with evenly divided weight values across the three available CCs, due to its operation limitation. Likewise JC is assumed to schedule only IoT since its PDU is first on the single queue, and this limitation is based on the architecture that it operates on, which only allows the first PDU on queue, of one particular type of terminal to be scheduled per time.

In Fig. 3.5, the data rate of the TAMC scheduler is compared to RR and JC schedulers, the data rate is plotted against traffic load ρ. The capacity C is derived from (3.5) with BW of 50 MHz set for each of the three CCs. The value of C varies from IoT and VSAT, depending on the particularly serving satellite, and this is because the value of E_b/N_o varies as shown in Table 3.1. The plot shows that TAMC acheived average data rate of 138.45 Mbps, while RR and JC performed at 56.72 Mbps and 81.83 Mbps respectively when ρ is 0.1 load; it shows that TAMC out performs RR and JC by 83.75 % and 51.40 % respectively. The same percentage difference is noticed when ρ is at 0.5.

The performance of delay is shown in Fig. 3.6, which indicates same overlapping trend for TAMC, RR and JC schedulers. This is due to the usage of the three orbital layers by the three schedulers of TAMC, RR and JC. In Fig. 3.7, the energy efficiency in b/J is plotted against traffic load (ρ), and it shows the performance of TAMC compared with RR and JC. When ρ traffic load is 0.1, TAMC attains energy efficiency of 0.91 b/J, while RR and JC perform at 0.36 b/J and 0.48 b/J respectively. This shows that TAMC out performs RR and JC by 86.61 % and 61.87 % respectively. Even when ρ is 0.5, TAMC still out performs RR and JC by 85.71 % and 59.74 % respectively. During the scheduling process it was discovered that RR and JC experience limitation on the number of terminals and variety of satellite CCs they can utilize at once, thereby limiting their data rate and energy efficiency performance. TAMC is robust without limitations, as it can schedule all terminals including

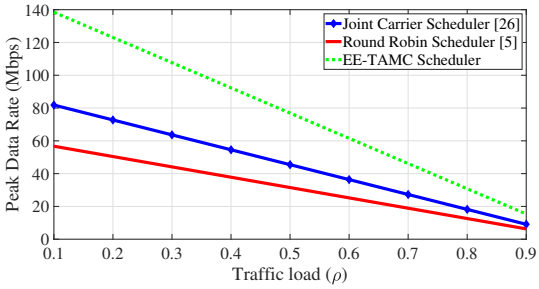

Figure 3.5: Data rate verses traffic load.

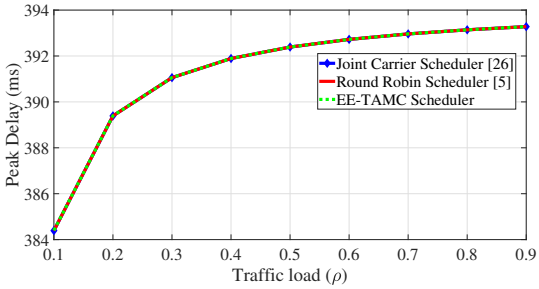

Figure 3.6: Delay verses traffic load.

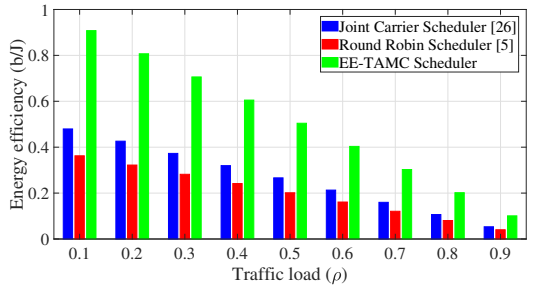

Figure 3.7: Energy efficiency verses traffic load.

IoT and VSAT at the same time, utilizing all the available CCs of LEO, MEO and GEO satellites, in an intelligent resource allocation optimal pattern where data rate and energy efficiency are optimized with efficient utilization of the spectrum and system. This confirms TAMC is more superior to RR and JC.

3.5 Conclusions

In this chapter, the uplink capacity and energy utilization of a satellite network is optimized by employing MC technique which aggregates the capacity of LEO, MEO and GEO CCs. A network topology was design of a multi-layer NTN with a HGS that connects to the three orbital satellites of LEO, MEO and GEO, allowing for the usage of MC at higher layers

for the optimization of network performance aided by softwarized network controller and scheduling algorithms. A new scheduling architecture was also presented known as terminal differentiating multi-layer NTN resource scheduling architecture, that employs a softwarize dispatcher at the network layer which implements the terminal packet classification and dispatching. The dispatcher separates the PDUs onto different queues based on UT type of VSAT and IoT UTs. This architecture employs the proposed algorithm known as the TAMC algorithm, which intelligently defines the resource allocation pattern in form of a proportionality ratio α, that is derived based on C/N of the respective serving links to the various VSAT and IoT terminals. From the evaluation of the energy efficiency and throughput, TAMC outperformed RR and JC, confirming that TAMC is a superior uplink energy efficient scheduler with high capacity capabilities.

Future research areas that can be considered is the extension of this work to include many satellites in each of the three orbital layers; exploiting artificial intelligence and machine learning in the functionality of a robust optimizing scheduler.

Chapter 4

Uplink: Resource Management Techniques involving 5G Use-cases and Protocols in Multi-Orbital NTN

This chapter introduces the concept of energy efficiency (EE) in the uplink with the capability of multi-connectivity (MC) in a multi-orbit non-terrestrial network (NTN), where user terminals (UTs) can be simultaneously served by more than one satellite to achieve higher peak throughput at reduced energy consumption. This concept also considers the service classification of the users, so that network dimensioning is performed in order to satisfy the quality of service (QoS) requirement of users. MC can increase throughput, but this entails increased power consumption at user terminal for uplink transmissions. To this end, an energy-efficient service-aware multi-connectivity (EE-SAMC) scheduling algorithm is developed in this chapter to improve the EE of uplink communications. EE-SAMC uses available radio resources and propagation information to intelligently define a dynamic resource allocation pattern, that optimally routes traffic so as to reduce the energy consumption at the UT while ensuring QoS is maximized. EE-SAMC is designed based on the formulation of a non-convex combinatorial problem, it is solved in two ways involving firstly an optimization solution and secondly a heuristic approach. The effectiveness of EE-SAMC is compared with random allocation, round robin and heuristic schedulers in terms of EE, throughput and

delay; EE-SAMC outperforms all schedulers.

4.1 Introduction

Energy efficiency is a growing concern in the design of satellite networks and there are concerted efforts to reduce the energy consumption of satellite communication systems, especially in the ground segment [70]. Most satellite user terminals (UTs) have been traditionally designed to operate on an always-on basis, which can result in significant energy usage [71]. This impact is becoming more significant as the number of UTs increases, resulting in elevated levels of carbon dioxide (CO_2) emissions and raising environmental issues. To mitigate these concerns, it is crucial to focus on efficient uplink transmissions and to implement power-saving measures wherever possible [72]. Consequently, employing such procedures can reduce the environmental footprint of satellite communication systems while maintaining global connectivity that is both reliable and effective. This underscores the importance of considering the EE of satellite networks and making it a priority in their design and operation. Thus, the escalating energy costs and the associated global carbon emissions from the communications devices have inspired researchers to devote more efforts for developing energy-efficient communication systems [73].

Furthermore, satellite communications industry is witnessing a major transformation because the paradigm shift brought about by several key technological advancements such as software-defined satellites, very high throughput satellites (VHTS), non-geostationary orbit (NGSO) systems, virtualization and service orchestration [48]. Specifically, recent developments primarily focus on deploying reconfigurable satellite payloads in order to offer generic and software-based solutions as well as providing high throughput transmissions [49]. In addition to the established satellite applications like aeronautical, maritime, mapping, weather forecasting, and broadcasting, the recent advances have opened up the satellite potentials to convey and execute various innovative use cases and new services from space [74]. Therefore, satellite traffic demand is currently soaring to provide affordable, accessible, uninterrupted wireless connectivity especially to the underserved and unserved areas.

Another hurdle faced by the satellite communications is the scarcity of resources particularly the radio frequency (RF) spectrum [51]. Therefore, it is crucial to devise unconventional techniques to improve resource utilization while satisfying the high data rate and low latency

requirements. In this direction, an intriguing concept has been recently studied within the multi-beam satellite architectures, that is dual connectivity (DC), which allows users to be simultaneously served with different systems and/or frequency bands [1]. The DC feature has been considered by the 3rd Generation Partnership Project (3GPP) in Release 12 for adoption to the fifth-generation (5G) New Radio (NR) specifications owing to its capability of maximizing the spectrum utilization and avoiding the traffic overload [36]. Similarly, the well-known carrier aggregation (CA) concept has been introduced to the satellite communication systems [12] to increase the achievable peak data rate, where a single user is served by multiple beams/carriers simultaneously.

Beyond this, multi-layered non-terrestrial network (NTN) is a vital enabler for providing ubiquitous and ultra-high capacity global connectivity to a wide range of applications requiring high availability and high resilience [75]. Multi-layered multi-orbit hierarchical NTNs of satellites, i.e., the orchestration among different satellites cooperating at different altitudes, are a highly appealing technological solution for addressing coverage and latency constraints associated with the NTN paradigm. In this direction, the 3GPP group has lately codified the use of satellites and aerial platforms to construct multi-layer NTNs in order to provide space-based 5G communication services and support future wireless ecosystems [52]. Thus, it is essential to expand the concept of DC into MC in order to adapt to the flexibility and scalability offered by the emerging NTN architectures and the integrated terrestrial and non-terrestrial communication systems [53] [54].

The MC techniques are envisioned as an indispensable technology to significantly enhance the offered system capacity and improve the spectral efficiency in the heterogeneous networks. An important foreseeable application of MC is the interworking among various communication standards and architectures promoting a smoother transition, e.g., between fourth generation (4G) and 5G systems [55]. The MC solution achieves not only higher per-user data rate but also provides mobility robustness, and thus, it can improve the resilience of wireless communications [56]. Additionally, data traffic in NTNs is highly diverse and randomly distributed in the service areas, and arising from various users with different quality-of-service (QoS) requirements [57]. Thus, employing MC in NTNs would help satisfy the asymmetry and heterogeneity of traffic demands. However, enabling MC in UTs to utilize multiple aggregated carriers/systems that inevitably comes at the cost of higher power consumption [12]. Further, the EE in NTNs is one of the major challenges, especially for

uplink transmissions and for the battery-limited mobile terminals [58].

In the literature, some contributions have studied and evaluated the issue of EE for the uplink transmissions in the satellite domain. For instance, the energy resource allocation problem in the uplink communications is investigated in [59] within the space-air-ground Internet of remote things networks, which aims at maximizing the system EE by jointly optimizing sub-channel selection and uplink transmission power control. In [60], a joint optimization model of spectrum efficiency and EE in a single-station multi-satellite multiple input multiple output (MIMO) system was proposed based on a knee-point driven optimization algorithm. Further, a spatial group based optimal uplink power control scheme is proposed in [61] for enhancing the performance of random access in satellite networks. Additionally, two optimal power control schemes are proposed in [62] for maximizing both delay-limited capacity and outage capacity in cognitive satellite terrestrial networks, which are useful performance indicators for real-time applications. It is worth noting that the aforementioned works [59–62] do not consider concurrent aggregating multi-orbit scenarios in optimizing the uplink transmit power for satellite users.

Nevertheless, the potential of performance enhancements in throughput, latency, and reliability with MC especially for the new service use-cases of 5G [76] [77], have motivated this work to further investigate the uplink EE issue from a UT standpoint. Furthermore, network resiliency and redundancy is an important feature that empowers the network high survivability in the event of failures, and multi-layer architecture is a promising technology that is going to be explored in this direction [33]. The power limitation of UTs including the battery-powered which are sometimes used in remote/rural areas [78], is a fundamental problem that requires intervention; this is the focus of this chapter. Similarly the global CO_2 emission reduction target of 45% by 2030 and carbon neutrality by 2050 [79] is also a motivation to investigate ways to enhance the EE of the ever-increasing satellite users. To the best of our knowledge, optimizing the uplink transmit power problem has not been studied yet in the open literature within MC enabled multi-orbit NTNs. In addition, a novel scheduling technique is proposed to satisfy the variations in user traffic demand.

Contributions: Our key technical contributions can be explicitly summarized as follows:

1. Design guidelines are outlined for the deployment of a multi-layer satellite network comprising low earth orbit (LEO), medium earth orbit (MEO), and geostationary earth

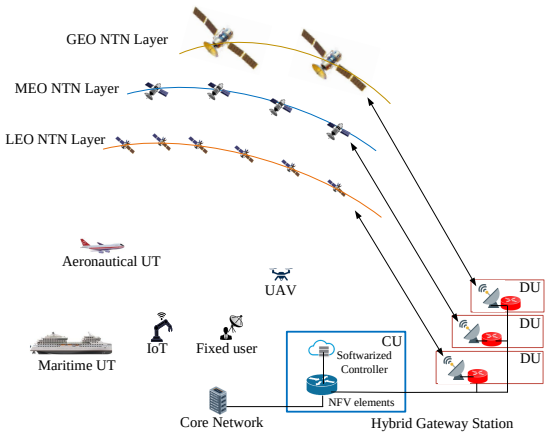

Figure 4.1: A schematic diagram of the network topology for the multi-layer NTN.

orbit (GEO) satellites, which are all served by multi-orbital hybrid gateway stations (HGSs) [1]. These gateway stations operate with softwarized controller and network function virtualization (NFV) elements at the network and data link layers, the softwarized controller performs functions including the segmentation and classification of protocol data units (PDUs) based on the service category of the transmitting user [80]; this allows for a pure softwarized implementation of schedulers. PDUs are specific block of information units transmitted over a network channel.

2. Developing a scheduler aided by a segmentation algorithm with protocol stack adaptation, which assigns priority and preference for resource allocation to PDUs based on identified service classes. In this work, three classes are considered from 3GPP; namely, ultra-reliable low latency communication (URLLC)[1], massive machine type communication (mMTC), and enhanced mobile broadband (eMBB).

3. An energy-efficient service aware multi-connectivity (EE-SAMC) scheduling algorithm is developed for optimal resource allocation involving power and spectrum leading to a high capacity transmission with energy efficiency in the uplink. This algorithm considers radio parameters such as transmit power, carrier-to-noise ratio (C/N) and the energy-per-bit-to-noise ratio (E_b/N_o) of the available orbital satellite links. Scheduling and resource allocation are performed jointly.

4. The service aware multi-connectivity (SAMC) heuristic scheduler is designed based on

[1]3GPP requirements for URLLC cannot be satisfied in satellite communications due to propagation delay, so this represents latency-sensitive traffic/services in this chapter.

3GPP specification and link budget analysis. The proposed EE-SAMC algorithm and heuristic scheduler are evaluated by simulations and then compared to other state-of-the-art algorithms in terms of throughput, delay and energy efficiency.

The rest of the chapter is structured as follows. In Chapter 4.2, the network model and architecture are extensively discussed. The following Chapter 4.3 focuses on the resource allocation optimization problem. In Chapter 4.4, the proposed solution for the optimization problem is outlined. While the simulation setup and performance evaluation are covered in Chapter 4.5. Finally, the conclusion and future work are summarized in Chapter 4.6.

4.2 Network Model and Architecture

4.2.1 Network Topology and Service Architecture

The network topology consists of the three layers of LEO, MEO and GEO satellite constellations, along with a HGS in which resides NFV elements with softwarized controllers at the central unit (CU), that controls the communication to these satellites through multiple inter-connected antenna ports operating in their respective distributed unit (DU), as shown in Fig. 4.1. The corresponding satellites then configure beams which provide coverage to various UT types such as terrestrial fixed, maritime, aeronautical, land-mobile, and internet of things (IoT). Fig. 4.2 shows a representation for fixed satellite service (FSS), aeronautical, and maritime heterogeneous traffic demand over the European continent from the coverage of 71 beam pattern provided by the European space agency (ESA) [57]. This clearly shows the dynamic service requirements involving different terminals with different service demands in the same geographical area. For instance, the traffic demands in the beam range from the $4th$ to the $13th$ beam is widely diverse in terms of type and amount as shown in in Fig. 4.2 (b). The HGS is configured with network elements (NEs) including NFV elements and softwarized controller operating at the network and data link layers. The softwarized segmentation unit (SSU) is in the NFV element, which performs the segmentation and classification of PDUs into different queues based on the service class demand of the user. This action allows the scheduling algorithm to allocate resources efficiently with high flexibility thereby optimizing the network key performance indicators (KPIs).

The proposed multi-layer NTN resource scheduling architecture is shown in Fig. 4.3, both control and user plane structural designs are provided along with the protocol stack of the

Table 4.1: List of used symbols.

Symbol	Definition	Symbol	Definition
P_{tx}, P_{tx}^{U}, P_i	Transmit power	$\vartheta_i(t, F_c)$	Channel gain
C/N	Carrier to noise ratio	Y, y	Number of propagation paths
E_b/N_o	Energy per bit to noise ratio	$\bar{R}, R$	Achievable rate
PL, PL_{t,S_t}	Total path loss	ρ	Traffic/system load
FSL	Free space loss	μ	Processing service time
L_{atm}	Atmospheric loss	A	Arrival rate
L_s	Loss due to troposheric or ionospheric scintillation	E_{η_i}, E	Energy efficiency
L_σ	Zero mean lognormal variable of shadowing environment	ϕ_i	Service class
F_c	Carrier frequency	s, S	Number of satellites
D	Propagation distance	P_c	UT circuitry power consumption
C_{pi}^{U}	Satellite received carrier power	a, b, c	URLLC, mMTC, eMBB
$EIRP_i^U$	Uplink EIRP of UT	M	Number of allowable CCs
G_{Si}	Satellite antenna gain	Z	Number of allowable satellites
G_{tx}^{U}	UT antenna gain	R_i^{min}	Minimum allowable data rate
N	Noise power	P_i^{max}	Maximum allowable transmit power
k_B	Boltzmann's constant	D_i^{max}	Maximum allowable latency
T	Noise temperature	ξ	Barrier parameter
B	Bandwidth	v, v_i	Slack variables
I_i^U	Uplink interference	$L(p, \lambda)$	Lagrange function
C/I	Carrier to interference ratio	$f_\xi(p, v)$	Merit function
γ_i^U	Carrier to interference and noise ratio	λ_g	Lagrange multiplier
t	time	H	Hessian
$\varrho_i(t, F_c)$	Space domain channel response	D_i	Latency
φ_i	Doppler shift	α, α_k^i	Weighting factor
τ_i	Propagation delay	η	Energy efficiency objective function
k, K	Number of resource blocks	C_t	Entropy penalty constant
i, I	Number of UTs	J	Jacobian
j, J	Number of component carriers	e	Vector of ones
$Q_{i,s,j,k}$	Independent variable indicator	G'	Weighted bipartite graph
c	Number of servers	M_p^*, M_p	Perfect matching

open system interconnect layers and corresponding 5G sublayers as described in [81]. In the control plane, some of the signaling activities that occur between the UT, radio access network (RAN), and core network (CN) include link adaptation, UT authentication, scheduling request and others. Link adaptation is performed at the physical layer, where the UT sends the estimated channel state to the HGS to perform the adaptation of modulation, coding and power. The UT also sends non access stratum (NAS) protocol signaling messages from the network layer to the CN, this message is passed transparently through the RAN, NAS is used for authentication of UT in the network. The service class of the UT is also determined from the service identification (SID) in the signaling message, and this is sent to the SSU in the radio link control (RLC) sublayer for classification and segmentation definitions. When the UT sends the scheduling request to the HGS from the medium access control (MAC) sublayer of the data link layer, the HGS will use the classification information from the SSU, to schedule and map the appropriate resources that meet the QoS requirement of the service class of the UT, this is done by using the radio scheduler (RS) and the proposed algorithm running in it at the MAC sublayer. The radio resource controller (RRC) sublayer handles the RRC connection establishment, maintenance and release signaling between the UT and HGS, where the addition, modification and release of CA, DC and MC is initiated.

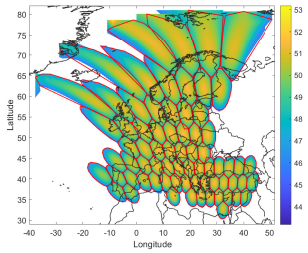

(a) The 71 beam pattern of ESA over Europe.

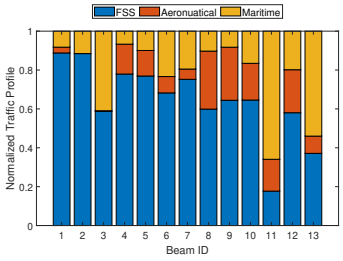

(b) Traffic profile of heterogeneous demand with 71 beam pattern.

Figure 4.2: Emulated heterogeneous traffic for FSS, aeronautical and maritime over the European continent [57].

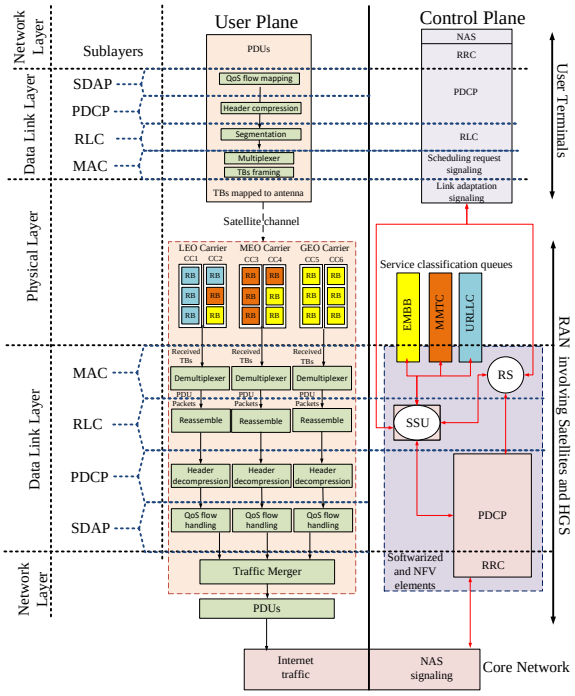

Figure 4.3: Schematic diagram of service aware multi-layer NTN resource scheduling architecture for the uplink transmission scenario.

In the user plane, PDUs from the network layer of the UT are transfer to the service data adaptation protocol (SDAP) sublayer in the data link layer, where QoS flow mapping is performed onto data radio bearers for each PDU session. This is further sent to the packet data

convergence protocol (PDCP) sublayer, where header compression and ciphering is performed on the PDUs. At the RLC sublayer, segmentation is performed on the PDUs, and then the PDUs are forwarded to the multiplexer in the MAC sublayer, where the PDUs are multiplexed and mapped from logical channels to transport channels. Then framing into transport blocks (TBs) occurs, and the TBs are mapped to the antenna in the PHY layer, then transmitted using appropriate satellites (either LEO, MEO or GEO), component carriers (CCs) and resource block (RBs) in PHY of the HGS, based on the scheduling pattern assign by RS inline with the service classification of SSU identified during the signaling session on the control plane. The TBs of different UTs in the uplink direction follow a Markovian arrival process with arrival rate A [69], arrive at the demultiplexer unit in the MAC sublayer, where TB frames are demultiplexed to PDUs, belonging to one or more logical channels from transport channels of physical layer. Then MAC pass the PDUs to the reassemble unit of the RLC sublayer for reassembling. Header decompression and deciphering is performed at the PDCP sublayer on the PDUs. Furthermore, the PDCP then pass the PDUs to the SDAP sublayer for QoS flow handling after which the PDUs are merged at the traffic merger in the network layer and pass to the CN as internet traffic. It is important to note that SDAP protocol only exits in the user plane and it does not exit in the control plane. Based on our proposed architecture, the datalink and network layer parts of the HGS are softwarized and NFV elements. This virtualisation at the HGS, will introduce energy consumption reduction at the HGS as fewer physical network elements will be required to function for the three orbitals as compared to conventional gateway stations [82].

As the scheduling algorithm is executed in the RS unit, it implements the resource allocation process based on input radio link parameters including transmit power (P_{tx}), uplink C/N, and the E_b/N_o along with the information of the type of service required by the uplink transmitting terminal in the control plane. In this chapter, three service classes are considered in the optimization problem of the proposed EE-SAMC scheduling algorithm, i.e. URLLC, mMTC, and eMBB as detailed in 3GPP Release-15 of 5G standards [52]. The following conditions must be satisfied to perform the dynamic resource allocation and traffic steering using the EE-SAMC algorithm.

- There must be sufficient E_b/N_o value to satisfy the link budget requirement for the respective LEO, MEO, and GEO satellite links.

- The orbital satellites of LEO, MEO, and GEO must be visible to the users employing MC. In addition, the UTs must be capable of connecting to the three orbital constellations [63].

- The UTs must be capable of informing the HGS of its unique service category with a SID via signalling information exchange, which will allow the SSU at the HGS to differentiate UTs into the different service classes. This can be done by implementing policy control configurations with stored subscription information of the users in a subscriber database.

4.2.2 Uplink Transmission Model

The uplink transmission begins from the UT that transmits to the satellites in the constellation, then further to the HGS which is connected to the core network, the satellite and the HGS comprise of the RAN. The communication link is established based on the ink budget analysis with air-interface configurations that accounts for the required power and gains to successfully transmit over the satellite channel. The total path losses (PL) in dB of the link between the UT and the satellite can be modelled as follow:

$$PL = FSL + L_{atm} + L_s + L_\sigma \tag{4.1}$$

where FSL is the free space loss that is given in (4.2). The atmospheric loss (L_{atm}) accounts for the losses from the atmosphere, which is modelled by taking into consideration temperature, pressure, and water vapour density as provided in ITU-R P.676 [83]. The signal loss due to tropospheric or ionospheric scintillation is represented as L_s which impacts signals in Ka band, and this is influenced by the user elevation angle as decribed in ITU-R P.618 [84]. L_σ represents zero mean lognormal variable with variance indicating the harshness of shadowing environment $L_\sigma \sim (0, \sigma^2)$, where σ^2 values are given by 3GPP for rural, dense urban and urban scenarios [85].

$$FSL = 32.45 + 20\log_{10} F_c + 20\log_{10} D \tag{4.2}$$

where F_c is the carrier frequency in GHz and D is the propagation distance in meters. In this system, the UTs are randomly distributed within the coverage area of the satellites, and the impact of the inter-user interference is taken into account. Specifically, an intended UT_i

is served by the satellite S_i while interfering UT_t is served by interfering beam of another satellite S_t. Then, the received power at the satellite S_i from UT_i is computed as follows

$$C_{pi}^{U} = EIRP_{i}^{U} + G_{S_i} - PL \tag{4.3}$$

where the uplink $EIRP_i^U$ is based on the radiation pattern of the UT antenna and expressed as $EIRP = P_{tx}^{U} + G_{tx}^{U}$, with P_{tx}^{U} and G_{tx}^{UT} representing transmit power in dB and gain in dBi of the UT. G_{S_i} is the gain of the satellite S_i. The uplink noise power is expressed as:

$$N = 10\log_{10}(k_B T B) \tag{4.4}$$

where k_B is the Boltzmann's constant in J/K, T is equivalent noise temperature of the satellite antenna in Kelvin and B is the bandwidth in Hz.

Thereby, the uplink C/N in dB is obtained by subtracting (4.4) from (4.3) in dB as shown below:

$$C/N_{i}^{U} = EIRP_{i}^{U} + G_{S_i} - PL - N \tag{4.5}$$

Consequently, the total interference in the uplink (I_i^U) in dB is derived as:

$$I_{i}^{U} = EIRP_{t}^{U} + G_{S_t} - PL_{t,S_t} \tag{4.6}$$

This is the interference from UT_t served by satellite S_t. The resultant carrier to interference ratio (C/I) in dB is given as

$$C/I_{i}^{U} = EIRP_{i}^{U} + G_{S_i} - PL - I_{i}^{U} \tag{4.7}$$

The carrier to interference and noise ratio ($C/I + N$) in dB is [85]:

$$\gamma_{i}^{U} = C/I + N_{i}^{U} = -10\log_{10}(10^{-0.1C/N_{i}^{U}} + 10^{-0.1C/I_{i}^{U}}) \tag{4.8}$$

- Uplink Channel Model: The uplink channel can be modeled as a ray-tracing channel modeling approach. Using this approach, the space domain channel response between

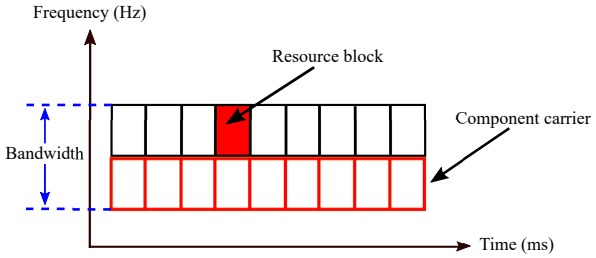

Figure 4.4: Resource block and component carrier

UT i and satellite s at time t and frequency F_c is represented as [86]

$$\varrho_i(t, F_c) = exp\{j2\pi[t\varphi_i - F_c\tau_i]\} \; . \; \vartheta_i(t, F_c) \tag{4.9}$$

where j is $\sqrt{-1}$, φ_i is Doppler shift, τ_i is propagation delay and $\vartheta_i(t, F_c)$ is the UL channel gain of the UT i given as

$$\vartheta_i(t, F_c) \triangleq \sum_{y=1}^{Y-1} \vartheta_i . exp\{j2\pi[t\varphi_i - F_c\tau_i]\} \tag{4.10}$$

where Y is the number of propagation paths of the UT i. The channel model in (4.9) is applicable when the relative position of the UT and satellite do not change substantially. If the UT and/or the satellite move over wide distances, the channel parameters mentioned above will vary and they will require to be update accordingly [87].

- Radio Resource: This is the radio resources used for scheduling, it comprises CCs that are made up of several RBs that serve as time and frequency domain resources as shown in Fig. 4.4.

- Achievable Rate: Assuming ideal HGS to satellite links, the achievable rate in Mbps on the return link of UT_i though satellite S_i on RB k and CC j with bandwidth B is

$$\bar{R} = B \log_2(1 + \gamma_i^{UT}) \tag{4.11}$$

Hence the average data rate is expressed as

$$R_i = \sum_{j=1}^{J} \bar{R}_{ij} \tag{4.12}$$

where the number of CCs is represented by J.

- System Queuing Model: The satellite UL PDU transmission can be modelled with $M/M/c$-PS queue model, where the first M is for the Markovian Poisson arrival and the second M represents the exponentially distributed service time in a processor sharing (PS) having c servers [66]. Here the UTs transmit the PDUs which arrive the RAN in a Markovian arrival process with A arrival rate, and PDU process service time as μ at the server. The system load is given as [67]:

$$\rho = \frac{A}{c.\mu} \tag{4.13}$$

- 5G Service Classification: The service classification adopted includes URLLC, mMTC and eMBB as specified by 3GPP.
  - URLLC application services are latency intolerant such as industrial automation and smart grids, hence network dimensioning is performed to satisfy the objective of low latency transmission, which can be achieved with LEO resource. Although LEO cannot guarantee the 3GPP requirements, it will be used for URLLC because it exhibits the lowest latency.
  - mMTC use case involves IoT which requires low power consumption for many connected devices; continuity of service for telematic applications of a group of sensor devices distributed over stationary or mobile wide areas, examples of mMTC applications includes assets tracking and surveillance of critical oil infrastructure. This particular service class has a characteristic of limited power budget for signal transmission especially in the uplink, hence LEO and MEO can be used for resource scheduling.
  - The eMBB service class requires high data rate resilience transmission network with high traffic capacity, and majority of the traffic demand is less sensitive to delay. Examples of eMBB use case includes provisioning of broadband connectivity to passengers on board a cruise ship and TV/multimedia service delivery to homes [52]. Hence LEO, MEO and GEO resources can be used even in DC/MC for this service.

4.2.3 Energy Efficiency Metrics

The achievable energy efficiency in a transmission system is the ratio of data rate R to the transmission power P required to achieve R [69]. It is expressed in bits-per-Joules (b/J) as given in (4.14).

$$E = \frac{R}{P(R)} = \frac{B\log_2(1+\frac{P_{tx}^U G_{tx}^U G_{S_i}}{k_B T B P L})}{P_{tx}^U + P_c} \tag{4.14}$$

where P_c is UT circuitry power consumption [88].

4.3 Resource Allocation Optimization Problem

4.3.1 The Objective Function

The energy efficiency of the users is defined as

$$\max_{Q_{i,s,j,k} P_i} \sum_{i=1}^{I}\sum_{s=1}^{S}\sum_{j=1}^{J}\sum_{k=1}^{K} \phi_i E_{\eta_i} Q_{i,s,j,k} \tag{4.15}$$

where $E_{\eta_i} = \frac{R_i}{P_i(R_i)}$ is the energy efficiency of UT_i with R_i and $P_i(R_i)$ as the data rate and transmit power, respectively. Additionally, $Q_{i,j,k,s}$ is an independent variable that denotes UT_i can be scheduled on the k-th RB of the j-th CC on satellite s. Further, ϕ_i is the traffic class connection identifier of the UT_i and $\phi_i \in \{a, b, c, 0\}$ which allows the resource allocation algorithm to give different resource priority and allocation preference to different users based on their service classes; i.e. a, b or c that correspond to URLLC, mMTC and eMBB, respectively.

4.3.2 Optimization Constraints

The design of the EE-SAMC strategy will be subject to several key constraints as detailed next.

Constraint on Route Selection

The PDUs can only be transmitted through available RBs on CCs of satellites, hence, the route selection strategy should be subjected to the utilization of these resources and service

identity of the user.

$$\mathbb{C}_1 : \sum_{i=1}^{I} Q_{i,s,j,k} \leq 1 \quad \forall k \in K, \forall j \in J, \forall s \in S \tag{4.16}$$

$$\mathbb{C}_2 : \sum_{j=1}^{J} \max_{k \in B} \; Q_{i,s,j,k} \leq M \quad \forall i \in I, \forall s \in S \tag{4.17}$$

$$\mathbb{C}_3 : \sum_{s=1}^{S} \max_{j \in L} \max_{k \in B} \; Q_{i,s,j,k} \leq Z \quad \forall i \in I \tag{4.18}$$

The constraint C_1 ensures that each RB_k can only be assigned to a single UT_i. On the other hand, C_2 restricts a UT_i to not having more than M CCs, constraint C_3 allows for MC with up-to Z different satellites of similar or different orbits.

Constraint on Transmit Data Rate

The transmit data rate must be above a set threshold, hence C_4 guarantees the UT_i operates above minimum data rate.

$$\mathbb{C}_4 : R_i = \sum_{s=1}^{S} \sum_{j=1}^{J} \sum_{k=1}^{K} Q_{i,s,j,k}.R_{i,s,j,k} \geq R_i^{min} \; \forall i \in N \tag{4.19}$$

Constraint on Transmit Power

The UT_i transmit power should not exceed the maximum transmit power required of the link as in constraint C_5.

$$\mathbb{C}_5 : P_i = \sum_{s=1}^{S} \sum_{j=1}^{J} \sum_{k=1}^{K} Q_{i,s,j,k}.P_{i,s,j,k} \leq P_i^{max} \; \forall i \in N \tag{4.20}$$

Constraint on Delay

Constraint C_6 ensures that the UE_i operates below maximum latency.

$$\mathbb{C}_6 : D_i = max\{Q_{i,s,j,k}.D_{i,j,k}\} \leq D_i^{max} \; \forall i \in N \tag{4.21}$$

Constraint on QoS Threshold

In C_7 the orbital link QoS must be above the threshold in order to be utilized.

$$\mathbb{C}_7 : min\{\frac{E_b}{N_o}_L, \frac{E_b}{N_o}_M, \frac{E_b}{N_o}_G\} > \eta \quad \forall, s, j, k, and \quad \forall i \tag{4.22}$$

4.4 Optimization Problem Solutions

The energy efficient maximization and capacity enhancement problem with the objective function in (4.15) and constraints C_1 to C_7 outlined above is a non-convex optimization problem; these constraints comprise of inequality constraints. This problem is combinatorial because it is intended to search and arrive at a combination of variables (which includes RBs, CCs and satellites) from many different available options under the mentioned constraints which optimizes an index (E_η). It is non-convex due to the maximization of the objective function, and similarly constraint C_4 is non-convex. The combinatorial optimization problem in (4.15) with constraints C_1 to C_7 is difficult to solve. For the sake of tractability, two approaches are used to solve this problem; first approach is by decoupling the problem into two optimization sub-problems, while the second option is a heuristic approach.

4.4.1 Sub-problem Decoupling Approach

This approach involves subdividing the problem into the joint route and power allocation sub-problem and the path matching sub-problem.

Joint Route and Power Allocation

The joint route and power allocation sub-problem is represented as (4.23).

$$\eta = \max_{Q_{i,s,j,k}, P_i} \sum_{i=1}^{I} \sum_{s=1}^{S} \sum_{j=1}^{J} \sum_{k=1}^{K} E_{\eta i}.Q_{i,s,j,k} \tag{4.23}$$

subject to $C_1 - C_5$

This problem is solved using the interior point algorithm (IPA) which offers a fast convergence in solving nonlinear programming problems especially the large scale ones [89].

Interior Point Algorithm In this Chapter, attempt is made to solve the sub-problem of (4.23) by using IPA which can serve as a linear and nonlinear programming solver [90]. This work uses the IPA from [91], adapted to the problem at hand.

IPA finds the minimum value of a convex objective function. The objective function in this case is non-convex which can be converted to convex by negating the function, and the inequality constraints $C_1 - C_5$ are considered. The corresponding problem for IPA is represented as a general nonlinear program model in (4.24), for ease of comprehension and presentation, the problem in (4.23) is adapted into it with further IPA solutions to follow.

$$\begin{aligned} &\min_{p} \quad -f(p) \\ &\text{subject to} \quad g(p) \leq 0 \end{aligned} \tag{4.24}$$

The approximate minimization problem in (4.24) with the interior-point algorithm is difficult to solve because of the inequality constraints, hence this will be simplified having $\xi > 0$ as,

$$\min_{p,v} f_{\xi}(p,v) = \min_{p,v} f(p) - \xi \sum_{i} \ln(v_i) \tag{4.25}$$

subject to

$$v \geq 0, \quad g(p) + v = 0.$$

The $v = \{v_1, v_2, v_3, ...\}$ represents the slack variables that are many as the inequality constraints g. The v variables are made positive to maintain the iterates in the interior of the feasible region. Hence when ξ (which is the barrier parameter) moves towards zero, the minimum of f_{ξ} extends to the minimum of f, while the logarithmic inserted in (4.25) represents a barrier function [92]. The transformation for the inequality constraint is applied to the constraints in (4.23), resulting in the new constraints outlined below.

$$\mathbb{C}_{1a} : \sum_{i=1}^{I} Q_{i,s,j,k} - 1 + v_1 = 0 \quad \forall k \in K, \forall j \in J, \forall s \in S$$

$$\mathbb{C}_{2a} : \sum_{j=1}^{J} \max_{k \in B} \; Q_{i,s,j,k} - M + v_2 = 0 \quad \forall i \in I, \forall s \in S$$

$$\mathbb{C}_{3a} : \sum_{s=1}^{S} \max_{j \in L} \max_{k \in B} \; Q_{i,s,j,k} - Z + v_3 = 0 \quad \forall i \in I$$

$$\mathbb{C}_{4a} : \sum_{s=1}^{S}\sum_{j=1}^{J}\sum_{k=1}^{K} Q_{i,s,j,k}.R_{i,s,j,k} - R_i^{min} + v_4 = 0 \ \forall i \in N$$

$$\mathbb{C}_5 a : \sum_{s=1}^{S}\sum_{j=1}^{J}\sum_{k=1}^{K} Q_{i,s,j,k}.P_{i,s,j,k} - P_i^{max} + v_5 = 0 \ \forall i \in N$$

The solution from (4.25) is obtained by using the Newton step in (p, v) at each iteration. The step tries to solve the Karush–Kuhn–Tucker (KKT) conditions in (4.26) and (4.27) through a linear approximation, the KKT equations give necessary and sufficient conditions for solving the minimization problem [93].

$$\nabla_p L(p, v, \lambda) = 0 \tag{4.26}$$

$$\lambda_g g_i(p) = 0 \ \forall_i \tag{4.27}$$

These KKT conditions use the Lagrangian function of

$$L(p, v, \lambda) = f_\xi(p, v) + \sum \lambda_g g_i(p) \tag{4.28}$$

where λ_g is the Lagrange multipliers. For each iteration, the algorithm attempts to decrease a merit function as

$$f_\xi(p, v) + \varsigma \|g(p) + v)\| \tag{4.29}$$

The parameter ς might increase with the iteration number so as to force the solution to a feasible point. This Newton step also known as the direct step uses the Hessian (H) of the Lagrangian of f_ξ as

$$H = \nabla^2 f_\xi(p) + \sum_i \lambda_i \nabla^2 g_i(p) \tag{4.30}$$

The outcome of attempting to solve for the KKT conditions using the linearized Lagrangian yields this matrix equation

$$\begin{bmatrix} H & 0 & 0 & J_g \\ 0 & \Lambda & 0 & V \\ J_g & I & 0 & 0 \end{bmatrix} \begin{bmatrix} \nabla_p \\ \nabla_v \\ \nabla_\lambda \end{bmatrix} = - \begin{bmatrix} \nabla_f + J_g \lambda \\ V\lambda - \xi e \\ g + v \end{bmatrix} \tag{4.31}$$

where J is the Jacobian of the respective constraint functions, λ is the Lagrange multiplier vector for inequality constraint g, e is the vector of ones with the same size as g, V is diag(v) and Λ is the diag(λ) [94] [95]. To solve for (∇_p, ∇_v), LDL factorization of the matrix is performed. LDL factorization allows for the unique factorization of the square Hermitian positive definite input of matrix $W = LDL^+$, where L is lower triangular matrix with elements that are unity diagonal, L^+ is the complex conjugate transpose of L; the diagonal matrix is represented as D [96].

As mentioned earlier, we utilize the available IPA solvers adapted to our problem. In particular, we are faced with the binary nature of the entries of Q. To incorporate the binary optimization under IPA, we relax Q to take values in the interval $[0, 1]$ and use the entropy penalty function

$$\mathbb{F}(Q) = C_t * (Q \log_2(Q) + ((1 - Q) \log_2(1 - Q)) \tag{4.32}$$

to the objective function, where C_t is a defined constant, to impose binary restrictions

The optimization problem in (4.24) is solved with the IPA by obtaining P_i for (4.23) as illustrated in Fig. 4.5a. With this, the joint route and power allocation sub-problem is solved; it paves the way for the path matching sub-problem to be solved.

Path Matching Sub-problem

The path matching sub-problem is expressed in (4.33) with the addition of constraints C_8, C_9 and C_{10}. The $\phi = \{a, b, c, 0\}$ is a set of service classes where a, b, c stands for URLLC, mMTC and eMBB services, respectively. 0 is included to account for PDUs that may not be identifiable into any of the three service classes defined. The aim is to solve for the perfect path match (Q^*) that ensures EE is maximized.

$$\max_{Q^*_{i,s,j,k}} \phi_i \eta_i \tag{4.33}$$

subject to $C_6 - C_{10}$

$$C_8 : R_i^* = \begin{cases} R_{iL} & \text{if } \phi = a \\ R_{iM} + RiL & \text{if } \phi = b \\ R_{iG} + R_{iM} + R_{iL} & \text{if } \phi = c \\ 0 & \text{otherwise} \end{cases} \tag{4.34}$$

$$C_9 : P_i^* = \begin{cases} \max(P_{iL}) & \text{if } \phi = a \\ \max(P_{iM}, P_{iL}) & \text{if } \phi = b \\ \max(P_{iG}, P_{iM}, P_{iL}) & \text{if } \phi = c \\ 0 & \textit{otherwise} \end{cases} \tag{4.35}$$

$$C_{10} : D_i^* = \begin{cases} \max(D_{iL}) & \text{if } \phi = a \\ \max(D_{iM}, D_{iL}) & \text{if } \phi = b \\ \max(D_{iG}, D_{iM}, D_{iL}) & \text{if } \phi = c \\ 0 & \textit{otherwise} \end{cases} \tag{4.36}$$

The constraints C_8 indicates the optimal data rate for the different service class, while C_9 and C_{10} represents the optimum transmit power and delay based on the service class in question. Since the route selection and power allocation strategy have both been solved, solution can now be derived for the path matching strategy. The UT path matching sub-problem is solved by modelling the uplink transmission network, as a weighted bipartite graph. The system is modelled as a weighted bipartite graph $G' = \{U', E', W'\}$, where U' represents the set of UTs, $E' = \{E'_{U,S}\}$ denotes the set of paths between the UTs and the satellites S'; $W' = \{_{\eta_i, P_i}\}$ is the weight sets (comprising of power, data rate and delay) between links E'.

A path weighted matching technique (PWMT) is used to arrive at the optimal path matching strategy that offers the maximum energy efficiency while satisfying the service class requirements. The PWMT was used in a seemingly small scale, however in a larger scale involving many UTs and satellites, the Hungarian algorithm can be applied which is presented from literature for completeness in Appendix A. At this stage, PWMT is applied to solve the sub-problem as illustrated in Fig. 4.5(b). Hence the optimal solution of the problem is obtained.

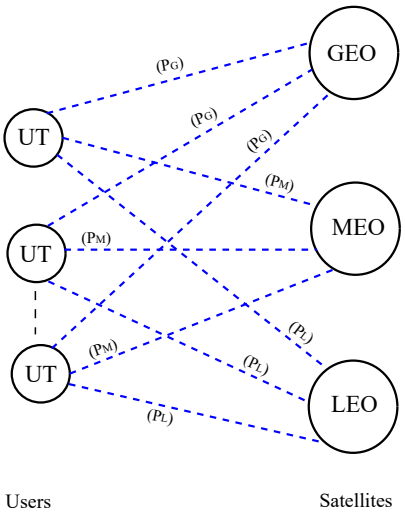

(a) Initial route selection and power allocation.

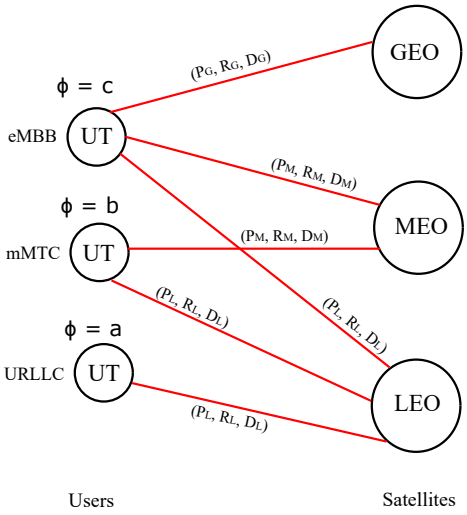

(b) Path matching.

Figure 4.5: Route selection and path matching.

4.4.2 Proposed Algorithm

The proposed algorithm is known as the EE-SAMC algorithm, which uses the service aware multi-layer NTN resource scheduling architecture shown in Fig. 4.3. The resource scheduling process commences with control plane signaling, where the service classification and segmentation of the UTs is performed using the SSU in the RLC sublayer, which segments the UTs to different queues of URLLC (a), mMTC (b) and eMBB (c) with Algorithm 3, also using the SID of the UTs as a differentiating identifier. Once the UT service class is known, the respective UTs are scheduled to appropriate resources including RBs, CCs and satellites that satisfy the QoS requirement of the service class in question, this scheduling is achieved using the EE-SAMC scheduling-Algorithm 4 at the RS unit in the MAC sublayer of the HGS. As

Algorithm 3: Service Classification and Segmentation.

Input: P_s = Arriving terminal PDUs
ID_s = Service ID
σ = Total number of transmitted PDUs
$j = 1$
Output: Q^a, Q^b, and Q^c

```
while j ≤ σ do
    if φ_k^i = a then
        Classify and Segment P_s as URLLC
    end
    if φ_k^i = b then
        Classify and Segment P_s as mMTC
    end
    if φ_k^i = c then
        Classify and Segment P_s as eMBB
    end
    if φ_k^i = 0 then
        Return to step 2
    end
end
```

the UTs transmit the PDUs in the user plane to the RAN, the PDUs arrive with arrival rate A to the appropriate RAN resources as described in Chapter 4.2.1.

The EE-SAMC algorithm defines the number of users, RBs, CCs and satellites; it considers the following parameters, the $\frac{E_b}{N_o}$ of the orbital satellites and the queue length of the respective service classes from Algorithm 3. It then solve for the route selection and power allocation strategy using (4.23); then the path matching strategy is obtained by solving (4.33) with the PWMT in Chapter 4.4.1. EE-SAMC algorithm then begins to perform the decision phase, by confirming if the $\frac{E_b}{N_o}$ values of the orbital satellites in view satisfy the QoS threshold requirement. If $\frac{E_b}{N_o}_L$, $\frac{E_b}{N_o}_M$ and $\frac{E_b}{N_o}_G$ satisfy the QoS threshold, then MC is performed. But if only two of any of the orbital links meets the threshold, then DC is performed with the satisfying links, else the algorithm reverts to single carrier mode to provision and maintain the network connectivity.

4.4.3 Heuristic Approach

This approach heuristically derives a weighting factor α to arrive at an energy efficient with uplink MC resource allocation pattern for the UTs on different orbital satellite links of LEO, MEO and GEO, while considering the service class of URLLC, mMTC and eMBB ascribed

Algorithm 4: Energy Efficient Service Aware Multi-Connectivity Scheduler

Number of users = I; Number of CCs = J; Number of RBs = K; Number of satellites = S. **Input:** $\frac{E_b}{N_o}_L$ = *QoS for LEO,* $\frac{E_b}{N_o}_M$ = *QoS for MEO,* $\frac{E_b}{N_o}_G$ = *QoS for GEO*
Q^a = Length of URLLC PDUs
Q^b = Length of mMTC PDUs
Q^c = Length of eMBB PDUs
$\sigma = Q^a + Q^b + Q^c$, $\eta = E_b/N_o$ Threshold, , $t = 1$
Route Selection and Power allocation strategy
Solve the problem in (4.23) with IPA to obtain P_i
Multi-connectivity strategy
Implement while considering C_7 (4.22)
while $t \leq \sigma$ **do**
  if E_b/N_{oG} *and* E_b/N_{oM} *and* $E_b/N_{oL} > \eta$ **then**
    Implement MC using all orbital carriers
  end
  if E_b/N_{oG} *and* $E_b/N_{oM} > \eta$ **then**
    Implement DC using GEO and MEO CCs
  end
  if E_b/N_{oG} *and* $E_b/N_{oL} > \eta$ **then**
    Implement DC using GEO and LEO CCs
  end
  if E_b/N_{oM} *and* $E_b/N_{oL} > \eta$ **then**
    Implement DC using LEO and MEO CCs
  end
  revert to single carrier mode on any available carrier
end
Path matching strategy
Solve the path matching sub-problem in (4.33) to obtain Q^*
Optimum solution obtained for (4.15):
$\max_{Q_{i,s,j,k},P_i} \sum_{i=1}^{I} \sum_{s=1}^{S} \sum_{j=1}^{J} \sum_{k=1}^{K} \phi_i^* E_{\eta_i}.Q_{i,s,j,k}$ *with* C_1 *to* C_7

$$\alpha''^{a}_{L} = \frac{\frac{\frac{C}{N}^{a}_{L}}{\frac{C}{N}^{a}_{L}+\frac{C}{N}^{a}_{M}+\frac{C}{N}^{a}_{G}}}{(\frac{\frac{C}{N}^{a}_{L}}{\frac{C}{N}^{a}_{L}+\frac{C}{N}^{a}_{M}+\frac{C}{N}^{a}_{G}}) + (\frac{\frac{C}{N}^{b}_{L}}{\frac{C}{N}^{b}_{L}+\frac{C}{N}^{b}_{M}+\frac{C}{N}^{b}_{G}}) + (\frac{\frac{C}{N}^{c}_{L}}{\frac{C}{N}^{c}_{L}+\frac{C}{N}^{c}_{M}+\frac{C}{N}^{c}_{G}})} \tag{4.37}$$

$$\alpha''^{b}_{L} = \frac{\frac{\frac{C}{N}^{b}_{L}}{\frac{C}{N}^{b}_{L}+\frac{C}{N}^{b}_{M}+\frac{C}{N}^{b}_{G}}}{(\frac{\frac{C}{N}^{a}_{L}}{\frac{C}{N}^{a}_{L}+\frac{C}{N}^{a}_{M}+\frac{C}{N}^{a}_{G}}) + (\frac{\frac{C}{N}^{b}_{L}}{\frac{C}{N}^{b}_{L}+\frac{C}{N}^{b}_{M}+\frac{C}{N}^{b}_{G}}) + (\frac{\frac{C}{N}^{c}_{L}}{\frac{C}{N}^{c}_{L}+\frac{C}{N}^{c}_{M}+\frac{C}{N}^{c}_{G}})} \tag{4.38}$$

$$\alpha''^{c}_{L} = \frac{\frac{\frac{C}{N}^{c}_{L}}{\frac{C}{N}^{c}_{L}+\frac{C}{N}^{c}_{M}+\frac{C}{N}^{c}_{G}}}{(\frac{\frac{C}{N}^{a}_{L}}{\frac{C}{N}^{a}_{L}+\frac{C}{N}^{a}_{M}+\frac{C}{N}^{a}_{G}}) + (\frac{\frac{C}{N}^{b}_{L}}{\frac{C}{N}^{b}_{L}+\frac{C}{N}^{b}_{M}+\frac{C}{N}^{b}_{G}}) + (\frac{\frac{C}{N}^{c}_{L}}{\frac{C}{N}^{c}_{L}+\frac{C}{N}^{c}_{M}+\frac{C}{N}^{c}_{G}})} \tag{4.39}$$

$$\alpha'^{a}_{L} = \frac{\alpha''^{a}_{L}}{\alpha''^{a}_{L} + \alpha''^{a}_{M} + \alpha''^{a}_{G} + \alpha''^{b}_{L} + \alpha''^{b}_{M} + \alpha''^{b}_{G} + \alpha''^{c}_{L} + \alpha''^{c}_{M} + \alpha''^{c}_{G}} \tag{4.40}$$

$$\alpha^{a}_{L} = \frac{(\frac{\alpha'^{a}_{L}}{\alpha'^{a}_{L}+\alpha'^{a}_{M}+\alpha'^{a}_{G}})}{N_c} \tag{4.41}$$

$$\alpha_L = \left\{\alpha^{a}_{L}, \alpha^{b}_{L}, \alpha^{c}_{L}\right\} \tag{4.42}$$

$$\alpha_M = \left\{\alpha^{a}_{M}, \alpha^{b}_{M}, \alpha^{c}_{M}\right\} \tag{4.43}$$

$$\alpha_G = \left\{\alpha^{a}_{G}, \alpha^{b}_{G}, \alpha^{c}_{G}\right\} \tag{4.44}$$

It should be noted that $0 \leq \alpha^{i}_{k} \leq 1$, where i represents the service class of URLLC (a), mMTC (b) or eMBB (c); k represents orbital satellite links of LEO (L), MEO (M) or GEO (G); N_c represents the number of service classes. The same notation applies to $\frac{C}{N}^{i}_{k}$.

to the UTs. A link budget analysis is performed as shown in Table 4.2, where the $\frac{C}{N}$ values of the orbital links are obtained from Table 4.2. The obtained $\frac{C}{N}$ values is applied into (4.37) - (41), to derived the corresponding weighting factor α. Then ultimately the α_L, α_M and α_G values are obtained using (42) - (44), which defines the allocation pattern.

4.4.4 Bench-mark Approach

Two other bench-marking approaches are described below which are used in Chapter 4.5.4, for comparison with the performance of the proposed optimization algorithm and the Heuristic approach.

Table 4.2: Link Parameters Specified by 3GPP Release 16 [68] and analytically derived

Parameters	LEO S-band	LEO Ka-band	MEO S-band	MEO Ka-band	GEO S-band	GEO Ka-band
Orbit altitude (Km)	1,200 ✓	1,200 ✓	10,000 ✓	10,000 ✓	35,786 ✓	35,786 ✓
Propagation range (Km)	2,942 †	2,942 †	10,752 †	10,752 †	36,343 †	36,343 †
UT elevation angle (degrees)	12.43 †	12.43 †	54.70 †	54.70 †	63.88 †	63.88 †
Satellite G/T (dB/K)	1.1 ✓	13 ✓	10 *	20 *	19 ✓	28 ✓
UL carrier frequency (GHz)	2 ✓	30 ✓	2 *	30 *	2 ✓	30 ✓
Bandwidth (MHz)	20 ✓	100 ✓	20 *	100 *	20 ✓	100 ✓
UT circuit consumption (dBm)	23 *	26.98 *	23 *	26.98 *	23 *	26.98 *
UT Tx gain (dBi)	0 ✓	43.20 ✓	0 *	43.20 *	0 ✓	43.20 ✓
UT transmit power (dBm)	49 †	29.03 †	51 †	29.54 †	53 †	30 †
Free space loss (dB)	167.84 †	191.36 †	179.09 †	202.62 †	189.67 †	213.19 †
Received isotropic power (dBW)	-156.63 †	-156.35 †	-165.60 †	-167.38 †	-174.18 †	-177.51 †
Uplink C/N (dB)	-0.16 †	4.47 †	-0.51 †	0.72 †	-0.09 †	-1.41 †
Eb/No (dB)	2.84 †	14.47 †	2.49 †	10.72 †	2.91 †	8.59 †
Data rate (Mbps)	24.00 †	133.55 †	24.49 †	131.07 †	26.10 †	130.68 †
Modulation	QPSK ‡	16QAM ‡	QPSK ‡	8PSK ‡	QPSK ‡	8PSK ‡
Code rate	1/3 ‡	5/6 ‡	1/3 ‡	5/6 ‡	1/3 ‡	3/4 ‡
✓ 3GPP, † Analytically derived, * Assumed, ‡ DVB-RCS2						

Random Allocation Scheduling Approach

This random allocation (RA) scheduling approach uses the different orbital transmission power of LEO, MEO and GEO as shown in Table 4.2, and the allocation pattern is derived in a random distribution, without any preferential consideration given to neither the orbital resource nor the UT service class. This approach is considered due to its low-complexity and fast allocation capability.

Round Robin Scheduling Approach

This scheduling approach makes use of the orbital transmission power of LEO, MEO and GEO as shown in Table 4.2. The resource allocation pattern is obtain using the round robin (RR) mechanism in [1], which allocates resources in a cyclic proportional pattern across all CCs regardless of all channel constraints.

4.5 Performance Evaluation

In this Chapter, the simulation configurations are outlined, along with discussions on the performance analysis of the proposed algorithm.

4.5.1 Simulation Setup

The simulation was setup to solve the problems and sub-problems mentioned in 4.4.1. In addition, more simulations were setup with a link budget analysis using parameters outlined in Table 4.2 for the Heuristic approach scheduler. MATLAB was also used to simulate the performance of the proposed algorithm in terms of energy efficiency, throughput and delay

while comparing other state-of-the-art algorithms. It is important to note that the link budget parameters used for analysis is the one related to Ka-band for LEO, MEO and GEO. This is because Ka-band UT uses a lower transmit power compared to the S-band UT which has a lower gain of 0 dBi resulting to a lower EIRP compared to the Ka-band; similarly the s-band satellites have lower G/T values compared to Ka-band satellites. In addition, s-band is a frequency range that is used for 4G and 5G NR [97] [98], and it has a limited bandwidth up to 30 MHz, while Ka-band offers a higher bandwidth of up to 400 MHz [68], and 100MHz with 20MHz have been adopted for Ka-band and S-band respectively in this chapter; even if three CCs of LEO, MEO and GEO are aggregated with 20MHz each it will result to only 60MHz which is less than 100 MHz (for a single CC) from Ka-band. A uniform band is also used across the three orbits, in order to minimize the complexity at the UT. The modulation and code rate (MODCOD) scheme impact is captured in the different Eb/No and C/N values of the link budget for the three orbital links, which demonstrates the performance of the air interface to limit the impact of the satellite channel noise and ensure the condition in constraint C_7 is satisfied with acceptable QoS value above the threshold set. The MODCOD is adopted of DVB-RCS2 air interface parameters, by mapping the resultant E_b/N_o of the link budget analysis to related ones as specified in [99].

4.5.2 Concept Evaluation of Multi-connectivity

In this Chapter, the advantages of using MC over single connectivity is discussed. Here we have three orbital satellite constellation resources with three service class demands, the constraints on the service class requirement is summarised in Chapter 4.2.2. The available satellite resources include LEO, MEO and GEO orbital satellites with different characteristics some of which are mentioned in Table 4.2. These resources are in form of frequency blocks called component carriers (CCs), that are made up of a collection of resource blocks (RBs), these RBs are time-frequency resources over which transmissions are scheduled. Hence packets can be scheduled for transmission over the satellites of the three orbits simultaneously, the transmitted information is multiplexed and not duplicated.

The achievable data rate (uplink capacity) enhancement which is an added feature is a non-convex linear optimization problem, and this problem can be solved by the aggregation of the allocated capacity of the CCs of the orbital satellites LEO, MEO and GEO, which can enable the realisation of the data rate requirement of use-case services especially eMBB.

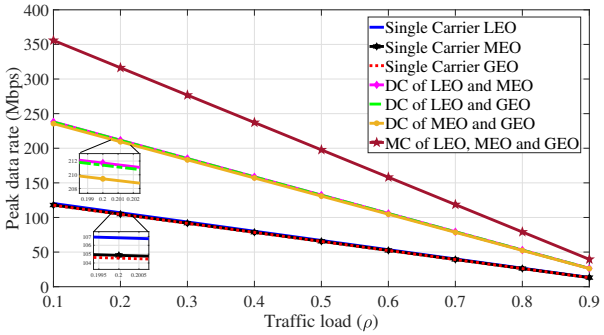

(a) Peak data rate with respect to traffic load.

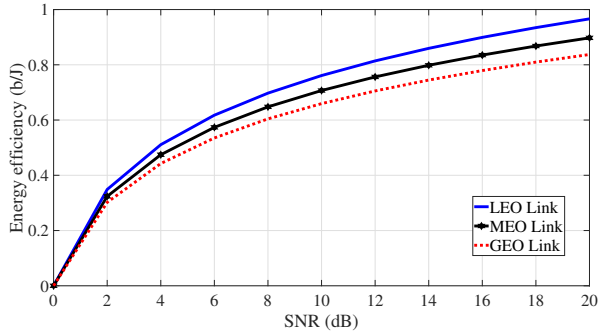

(b) Normalized orbital energy efficiency with respect to SNR.

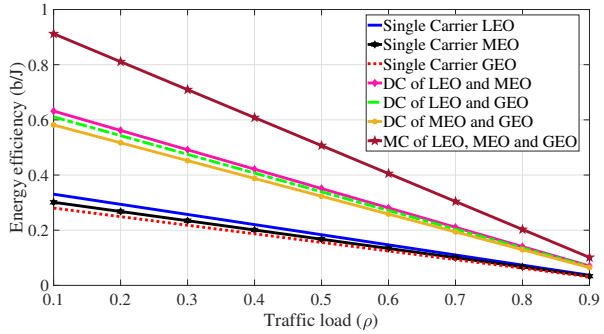

(c) Normalized energy efficiency with respect to traffic load.

Figure 4.6: Evaluation of MC, DC and single carrier performance.

Using the parameters in Table 4.2 data rate and EE with respect to traffic load is shown in Fig. 4.6. Precisely Fig. 4.6a shows that with DC and MC higher peak data rate can be achieved by using (4.12) compared to single carrier connectivity (SC) links. DC of LEO/MEO and LEO/GEO performs slightly better in peak data rate than DC of MEO/GEO due to the reduced FSL in the LEO CC which is a function of the satellite altitude; while MC of LEO/MEO/GEO out performs all carriers in data rate because of the aggregation of the three orbital CCs. It is also seen that DC and MC links maintain higher data rates trends over SC even as the traffic load increases. Another observation is the peak data rate performance

trend of SC LEO, MEO and GEO which overlap, mainly because of the parameter variation described in Table 4.2 involving satellite Gain to temperature ratio (G/T), transmit power and resultant FSL. Which shows LEO to operate with a lowest transmit power (29.03 dBm), lowest satellite G/T (13 dBi) and FSL (191.36 dB); MEO operating with a transmit power of 29.54 dBm, satellite G/T of 20 dBi and FSL of 202.62 dB, while that of GEO is 30 dBm for transmit power, 28 dBi for satellite G/T and 213.19 dB for FSL. Hence these parameter values leads to the overlapping in peak data rate trends for the SC and DC trends.

It is important to note that the transmit power requirement for LEO, MEO and GEO CCs are different which is obvious in the energy efficiency in Fig. 4.6b, LEO has the highest energy efficiency because of the limited power required to satisfy the link budget due to the low altitude and low FSL. This also corresponds to the energy efficiency of the DC and MC links in Fig. 4.6c, where all SC perform below the DC and MC combinations. Consequently, MC out performs DC in EE, because of the higher achievable data rate transmission capable with MC, as seen in Fig. 4.6a. Furthermore, the EE performance of SC LEO is better than SC MEO and GEO because of the lower transmit power required in LEO, and also MEO when comparing to GEO. Similarly, DC LEO/MEO is better than DC LEO/GEO and DC MEO/GEO because of the lower transmit power required for LEO and MEO compared to the other two DC options. MC of LEO/MEO/GEO achieves higher energy efficiency and data rate than all other single and DC carriers. Multi-orbital MC is advantageous because it introduces robustness to the network which allows for resiliency and higher system capacity.

4.5.3 Algorithm Complexity Analysis

The total complexity cost involved in solving the problem using Algorithm 2, depends on the sum of cost of the IPA and PWMT together. The cost of using IPA to solve the joint route and power allocation sub-problem is a product of the number of iterations, including the computation required to determine the Newton direction in each iteration. The Newton direction can be determined by solving linear equations in (4.31). Recall that the general complexity involved in solving n linear equations with n unknowns is $O(n^3)$, however the cost of computation of the Newton step based on (4.31) is $O(n)$. If the log barrier function in (4.25) is a self-concordant function, the number of Newton iterations is considered polynomial and it depends on the structure of the function. The complexity of IPA translates to $O(\sqrt{n}\ log\frac{n}{\epsilon})$ Newton iterations required to arrive at a feasible and optimal solution, with error tolerance

of ϵ, where n is the variables, which in our case is the sum of the number of UTs, RBs, CCs and satellites defined. As n increases, the execution time and complexity of the IPA increases. Hence, the complexity of IPA used in solving the joint route and power allocation sub-problem is $O(n^{1.5})$ [100] [101]. From the analysis of the simulation run time, the run time for network configuration comprising 3 variable counts for each of UTs, RBs, CCs and satellites is 0.024ms, while that with a configuration of 9 variable counts for each of UTs, RBs, CCs and satellites is 0.041ms.

The PWMT (Hungarian) algorithm increases complexity based on the increase in the number of user U' vertices in the bipartite graph, as $O(U'^3)$ [102].

4.5.4 Performance Analysis

The objective is to maximize the uplink energy efficiency of the UTs, whilst enhancing the data rate by implementing the MC technique using the EE-SAMC scheduler taking into consideration the requirements of the PDU service classifications. This is done by defining an optimal transmit power P and resource allocation pattern Q.

Likewise, the SAMC Heuristic scheduler also operates to maximize the uplink energy efficiency of the UTs, whilst enhancing the data rate by implementing the MC technique while taking into consideration the requirements of the UT service classifications. It achieves this by defining the transmit power from the link budget analysis in Table 4.2, and then it generates the resource allocation pattern α as explained in 4.4.3. Both EE-SAMC and SAMC Heuristic schedulers do not allocate resources on MEO and GEO CCs for URLLC class of PDUs. Similarly, both only utilize LEO and MEO CCs when allocating PDUs for mMTC class of services; for eMBB class of services all three LEO, MEO and GEO CCs are used for PDU allocation.

The other two schedulers used as benchmark in this chapter, are the RA and the RR schedulers. Both of them function by using the transmit power outlined in Table 4.2 from link budget analysis, but defined different allocation patterns. The Allocation pattern of RA is generated randomly using MATLAB program for each of the available orbital CCs without considering the service classifications. Similarly, RR also allocates PDUs on all available orbital CCs, in an equally proportionate manner without considering the service classifications.

In Fig. 4.7(a), the data rate performance of the EE-SAMC scheduler is compared to

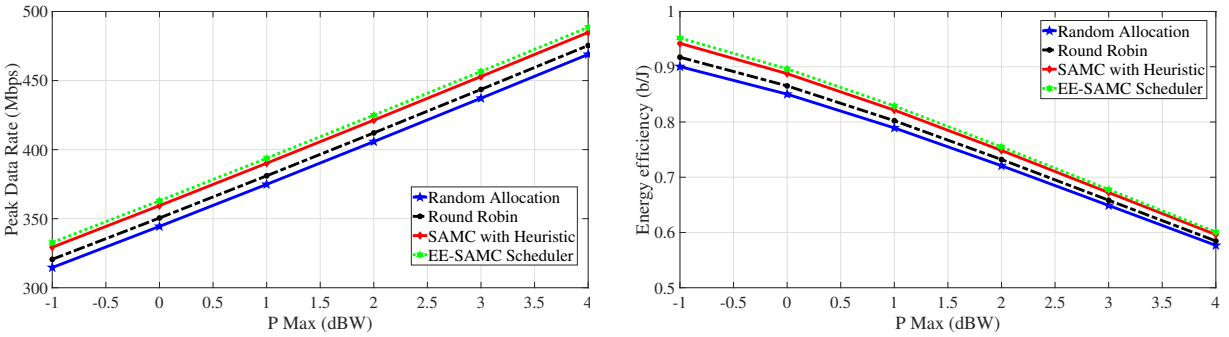

(a) Peak data rate with respect to P Max. (b) Normalized energy efficiency with respect to P Max.

Figure 4.7: Evaluation of PMax in peak data rate and energy efficiency.

heuristic, RR and RA schedulers, the data rate is plotted against maximum power (P Max). The achievable data rate R is derived using (4.12) with equal BW of 100 MHz set for each of the three orbital CCs. The plot shows that EE-SAMC achieves average data rate of 393.72 Mbps at P Max of 1 dBW, the Heuristic scheduler also achieves 390.14 Mbps data rate while RR and RA performed at 381.02 Mbps and 374.82 Mbps respectively when P Max is 1 dBW. This shows that EE-SAMC out performs the Heuristic, RR and RA by 0.91 %, 3.27 % and 4.91 % respectively. Further observation of the same chart trend shows that EE-SAMC out performs other schedulers.

In Fig. 4.7(b), the energy efficiency in b/J is plotted against P Max in dBW, and it shows the EE performance of EE-SAMC compared with the Heuristic, RR and RA schedulers. When P Max is 1 dBW, EE-SAMC attains energy efficiency of 0.83 b/J, while Heuristic, RR and RA schedulers perform at 0.82 b/J, 0.80 b/J and 0.78 b/J respectively. This shows that EE-SAMC out performs the Heuristic, RR and RA by 1.21 %, 3.68 % and 6.21 % respectively.

Similarly in Fig. 4.8a, where energy efficiency is plotted against signal-to-noise ratio (SNR) in dB. The energy efficiency performance shows that EE-SAMC achieved 0.80 b/J at 12 dB, while the Heuristic, RR and RA schedulers achieve 0.77 b/J, 0.75 b/J and 0.74 b/J respectively. It further shows that EE-SAMC out performs the Heuristic, RR and RA by 3.82 %, 6.45 % and 7.79 % respectively.

Furthermore, performance evaluation is done using Fig. 4.8b of energy efficiency against bandwidth in MHz. It shows that EE-SAMC achieves EE of 0.75 b/J at BW of 120 MHz, while the Heuristic, RR and RA schedulers achieve 0.72 b/J, 0.70 b/J and 0.69 b/J respectively. This shows that EE-SAMC out performs the Heuristic, RR and RA by 4.08 %, 6.89 % and 8.33 % respectively. In Fig. 4.8c, the performance of energy efficiency verse number

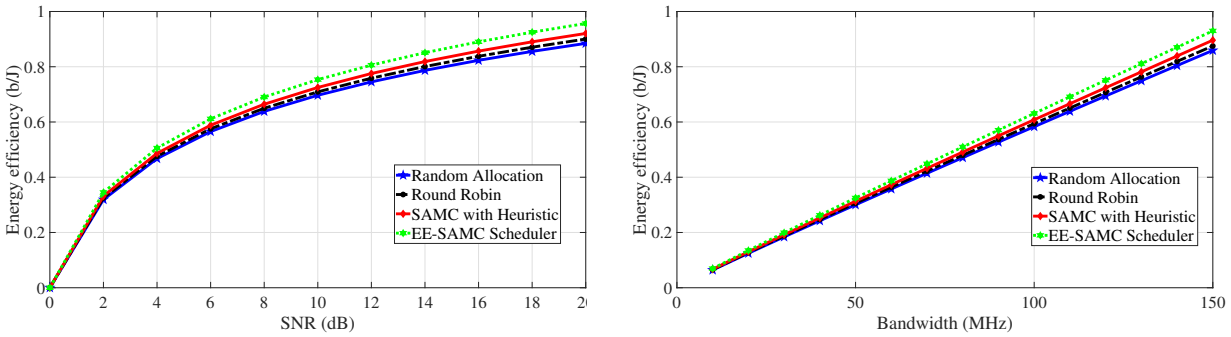

(a) Normalized energy efficiency with respect to SNR. (b) Normalized energy efficiency with respect to Bandwidth.

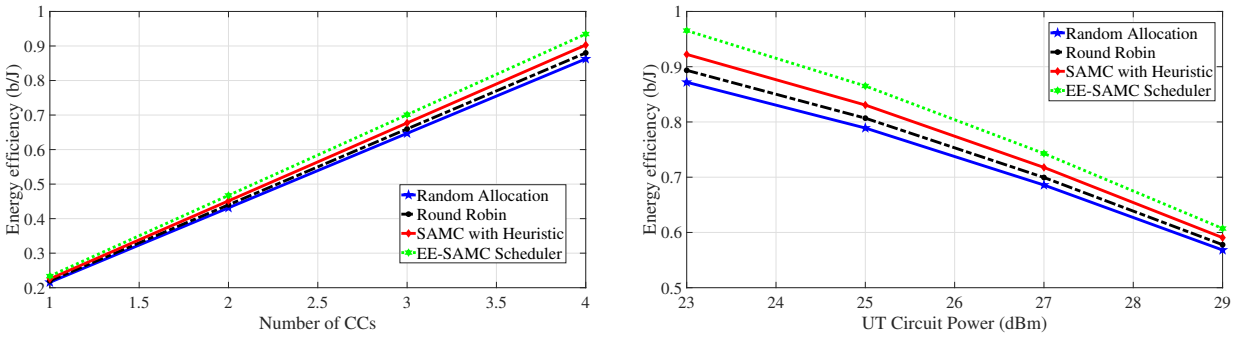

(c) Normalized energy efficiency with respect to CCs. (d) Normalized energy efficiency with respect to UT circuit power

Figure 4.8: Evaluation of normalized energy efficiency with SNR, bandwidth, CCs and UT circuit power.

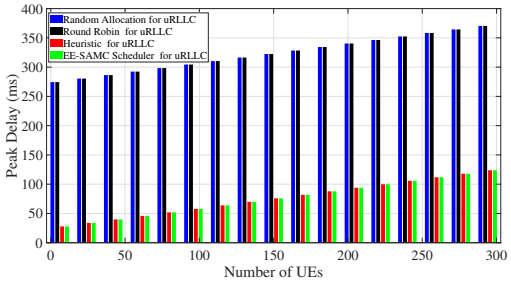

Figure 4.9: Peak delay with respect to number of UTs for URLLC service class.

of CCs is shown for EE-SAMC scheduler compared to Heuristic, RR and RA schedulers. The plot shows that at 4 CCs, EE-SAMC achieves 0.93 b/J, while the Heuristic, RR and RA schedulers achieve 0.90 b/J, 0.87 b/J and 0.86 b/J respectively. Which shows that EE-SAMC out performs the Heuristic, RR and RA by 3.27 %, 6.66 % and 7.82 % respectively.

The performance evaluation of EE verse UT circuit power (P_c) is shown in Fig.4.8d. It shows that EE-SAMC achieves EE of 0.74 b/J at P_c of 27 dBm, while the Heuristic, RR and RA schedulers achieve 0.71 b/J, 0.69 b/J and 0.68 b/J respectively. This shows that EE-SAMC out performs the Heuristic, RR and RA by 4.13 %, 6.99 % and 8.45 % respectively.

Finally, in Fig. 4.9 the performance of delay in ms of URLLC class of services are evaluated against number of CCs. The delay performance shows that EE-SAMC achieved 93.83 ms when number of users is 200, while the Heuristic, RR and RA schedulers achieved 93.83 ms, 340.37 ms and 340.37 ms respectively. This shows that EE-SAMC and the Heuristic schedulers achieve similar delay performance with the heuristic scheduler because they consider the service class during scheduling, and the URLLC PDUs are only allocated to the LEO CC. The RR and RA both achieved the same delay performance and are higher than EE-SAMC and heuristic schedulers, this is so because the schedulers do not consider the service class when scheduling the PDUs, they utilize any of the three orbital CCs of LEO, MEO and GEO for all service classes using their respective allocation patterns. Hence both of EE-SAMC and Heuristic out performed the RR and RA schedulers by 113.56 % and 113.56 % respectively.

During the scheduling process it was discovered that RR and RA showed limitations on the ability to dimension resources whilst considering the requirements of the service class of URLLC, mMTC and eMBB. This further impacted their energy efficiency, data rate and URLLC delay performance. EE-SAMC slightly out performed the Heuristic schedulers due to the fact that EE-SAMC allocates power in a more efficient pattern compared to the latter, nonetheless both showed robustness without much limitations in resource allocation, as they can route traffic intelligently in an optimal pattern while considering the requirements of the service classes of URLLC, mMTC and eMBB, where energy efficiency, data rate and delay are optimized with efficient utilization of the spectrum and system power resources. This confirms EE-SAMC is a superior scheduler compared to the Heuristic, RR and RA schedulers.

4.6 Conclusions

In this chapter, a multi-layer NTN network topology is considered that connects to LEO, MEO and GEO satellites simultaneously, which uses a HGS that employs softwarized controllers, NFV elements and scheduling algorithms for the optimization of uplink energy efficiency, throughput, delay and guarantees resiliency. A service-aware multi-layer scheduling architecture is also crafted with adaptation into the protocol stack, which shows user and control plane implementation framework. Furthermore, the optimization of uplink energy

efficiency, throughput and delay in a multi-layer satellite network is explored, by employing intelligent resource allocation strategies. Two approaches were analyzed involving optimization and heuristic algorithms, which were designed from combinatorial non-convex problem with linear inequality constraints and link budget analysis. These approaches took into account the service class of the transmitted PDUs and used MC to enhance throughput. From result analysis, our proposed scheduler (EE-SAMC) outperformed the heuristic and other state-of-the-art schedulers in terms of EE and throughput. A future research area could include exploiting the features of deep machine learning in solving the combinatorial optimization problem.

Chapter 5

Downlink: Multi-Agent DRL-Aided Dynamic Beam and Resource Allocation in Multi-Orbital NTN

Multi-tier non-terrestrial networks (NTNs) involving low Earth orbit (LEO), medium Earth orbit (MEO), and geostationary orbit (GEO) satellites are expected to be a major enabling technology for 6th generation (6G) systems, providing ubiquitous coverage to underserved areas. However, effectively managing such heterogeneous networks to satisfy dynamic traffic demands in a time-varying environment remains a challenge for satellite operators. This Chapter explores dynamic beam and resource allocation management techniques to enhance the capacity of multi-tiered NTNs over a stochastic channel, meeting the diverse service level agreements (SLAs) of users. To this end, a non-convex combinatorial optimization problem is formulated with inequality constraints. The problem is addressed by decoupling it into two subproblems: dynamic beam allocation and joint power and bandwidth allocation. The dynamic beam allocation subproblem is solved using an iterative algorithm, while the joint power and bandwidth allocation subproblem is solved using a multi-agent deep reinforcement learning (MADRL) aided resource allocation algorithm. This is achieved by leveraging the multi-connectivity (MC) technique with the objective of maximizing the offered capacity. The proposed algorithm operates within a network architecture that includes a hybrid gateway station (HGS) responsible for managing the satellites and providing different waveforms, such as 5G New Radio (NR) and DVB-S2X. The algorithm is executed at the HGS and determines the resource allocation pattern based on the channel quality indicator (CQI) and the user's

traffic class of ultra reliable low latency communications (URLLC), high definition television (HDTV) or enhanced mobile broadband (eMBB). The proposed algorithm outperforms the proportional fairness (PF) and bottleneck max fairness (BMF) algorithms in terms of sum rate/offered capacity by 44.94% and 72.56%, respectively.

5.1 Introduction

Our ability to communicate has evolved significantly over the past century, driven by the digitalization of information and the proliferation of interconnected computing devices. Today, as we advance toward the era of 6G networks, satellite communications and non-terrestrial networks (NTNs) are set to play a crucial role in this technological transformation [103]. By extending coverage to remote and underserved areas, enhancing connectivity in urban environments, and supporting low-latency applications, NTNs will be integral in realizing the full potential of 6G. NTNs can provide global seamless connectivity, bridging gaps that terrestrial networks alone cannot cover, and enabling new services and applications that rely on ubiquitous and reliable communications [49].

To fully harness the potential of NTNs in 6G, a multi-layered NTN architecture is essential. This approach integrates satellites across geostationary orbit (GEO), medium Earth orbit (MEO), and low Earth orbit (LEO) to ensure comprehensive coverage, enhanced capacity, and improved resilience for diverse environments and use cases. Additionally, this architecture supports the implementation of dual connectivity (DC) and multi-connectivity (MC) techniques, allowing devices to simultaneously connect to multiple satellites across different orbits or within the same orbit [4]. This redundancy enhances network reliability and ensures seamless transitions, thereby improving overall communication robustness. Moreover, data traffic within NTNs is characterized by significant variability and random distribution across different service areas, driven by diverse users with varying quality-of-service (QoS) requirements [104] [57]. Integrating DC and MC into this multi-layered NTN architecture can effectively address the inherent asymmetry and complexity of these traffic patterns.

In the context of multi-layer NTNs, beamforming is the technique of directing radio signals toward specific users or regions by precisely adjusting the phase and amplitude of signals from multiple antennas [105]. This technique is essential for effectively managing the highly dynamic and heterogeneous environment of NTNs [14]. However, the multi-layered

NTN architecture, while promising, introduces daunting challenges in resource management and beamforming, especially when DC and MC techniques are employed. The dynamic nature of satellite orbits, combined with varying user demands and channel conditions, complicates efficient resource allocation and makes it difficult to achieve optimal performance. Addressing these challenges through dynamic resource allocation and beam management is essential for the successful deployment and operation of multi-layered NTN architectures in 6G networks.

In this direction, reinforcement learning (RL) is a promising approach to address the complex and dynamic challenges of resource management and beamforming in multi-layered NTNs [106]. RL agents can learn optimal policies for resource allocation and beamforming decisions through interaction with the environment, making them well-suited for handling the dynamic and multi-objective nature of NTNs. Key advantages of using RL include adaptability to dynamic environments, handling multi-objective optimization, dealing with uncertainty, and scalability. By leveraging RL, NTN operators can develop intelligent resource management and beamforming strategies that optimize network performance, improve user experience, and enhance the overall efficiency of the system.

5.1.1 Related Works

The literature includes several contributions that study beamforming and resource allocation in wireless communications. In [107], the authors investigate the performance of a GEO-based high throughput satellite (HTS) system that uses free-space optical feeder links and has multi-beam capabilities over a Rician channel for the user link. In [108], an HTS equipped with a multi-beam digital channelizer is examined, where the system performs flexible frequency resource allocation in the presence of inter-beam interference in a varying demand environment, with the objective of improving throughput. Similarly, [109] presents a digital beamforming-based fusion control of transmit power and beam directivity for dynamic resource allocation in GEO HTS systems. The proposed model allows for the joint optimization of beam gain, power, and beam placement location, aiming to maximize the traffic accommodation rate.

Furthermore, the authors in [110] study joint power allocation and user pairing in a 5G LEO satellite random access network. A non-convex mixed-integer optimization problem is formulated with the objective of maximizing the sum rate. This problem is decomposed into two subproblems: optimal user pairing and optimal power allocation. The former is

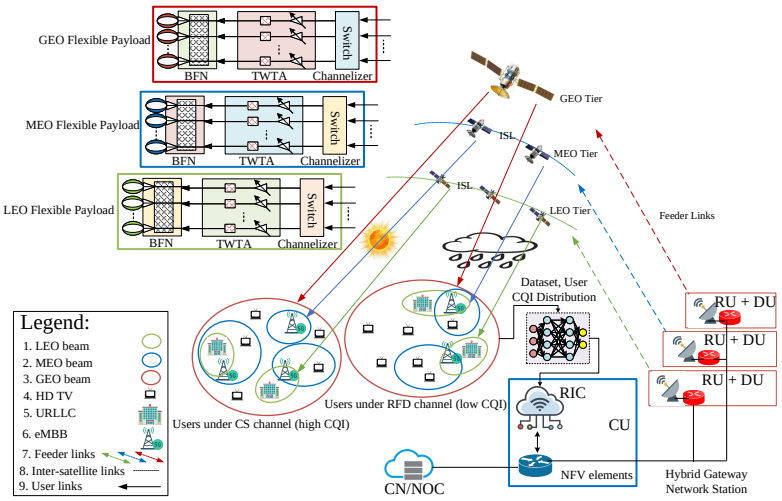

Figure 5.1: Schematic of the considered network topology of Dynamic Beam Forming in Multi-Tier NTN.

solved using RL, specifically the Q-learning algorithm, while the latter subproblem is solved using convex optimization. In [111], a satellite-terrestrial coordinated multi-satellite beam hopping (BH) scheduling strategy is proposed for a BH problem involving multiple LEO satellites, formulated as subproblems. The cell-satellite association subproblem is solved using a low-complexity iterative algorithm, while the multi-satellite traffic BH subproblem is solved using a multi-agent deep reinforcement learning (MADRL) approach, allowing each satellite to make cooperative real-time BH pattern decisions to maximize the network utility function.

5.1.2 Contributions

To this end, a MADRL-aided algorithm is proposed for optimizing the offered capacity, specifically designed to align with the dynamic properties of multiple NTN orbits. This algorithm effectively addresses the capacity challenges in a stochastic radio channel with dynamic capacity demands while achieving various defined service level agreements (SLAs). As a result, it facilitates the provision of seamless, uninterrupted, and high-capacity communication services for different use cases.

Contributions: Our key technical contributions can be summarized as follows:

1. Provide potential 6G network design involving a multi-layer NTN comprising LEO, MEO, and GEO satellites, managed by multi-orbital hybrid gateway stations/systems

(HGS) [112], within an open radio access network (RAN) architecture powered by artificial intelligence/machine learning (AI/ML) in the radio intelligent controller (RIC). The network is designed to operate with different waveforms, including 5G-NR for MEO and LEO links, while the GEO link employs a non-3GPP waveform such as DVB-S2X. This work tackles the challenges posed by the coexistence of different waveform designs, ensuring that our analysis remains both thorough and practical.

2. Development of a novel and robust dynamic beamforming and resource allocation (DyBM-RA) algorithm that optimizes transmit power, beam gain, and bandwidth allocation in the downlink to maximize capacity and enhance subscriber QoS. This algorithm incorporates MADRL to manage users with dynamic traffic categories, including Ultra-Reliable Low-Latency Communications (URLLC), High-Definition Television (HDTV), and enhanced Mobile Broadband (eMBB). The algorithm accounts for the stochastic behavior of the radio channel, and further considers the channel quality indicator (CQI) to identify and segment users as clear sky (CS) or rain fading (RFD), ensuring efficient resource allocation.

3. Present a systematic resource allocation technique that assigns users to specific orbits—LEO, MEO, or GEO, to satisfy SLAs. This approach enables the aggregation of traffic using DVB-S2X and 5G-NR protocols to achieve DC and MC functions in the downlink across intra- and inter-orbit LEO, MEO, and GEO layers, ensuring efficient resource utilization.

4. Derive a reference list of CQI values for the DVB-S2X waveform, systematically mapped from the 5G-NR standardization definitions.

The remainder of this Chapter is organized as follows: Chapter 5.2 covers the network architecture, channel model, and waveform designs. In Chapter 5.3, we present the formulated optimization problem, while Chapter 5.4 and 5.5 discuss our proposed solution. The simulation setup and performance evaluation are detailed in Chapter 5.6. Finally, the conclusions are provided in Chapter 5.7.

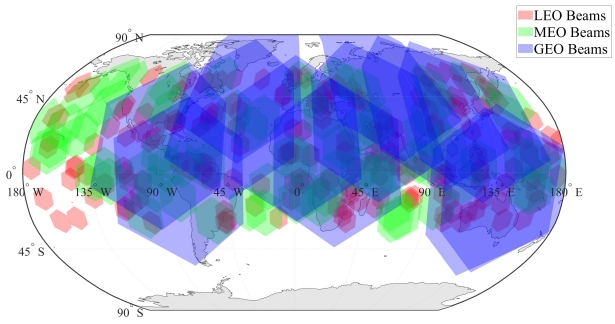

Figure 5.2: Depiction of beam layout in Latitude (-30 to 60 degrees) and Longitude (-180 to 180 degrees) for multi-orbital constellation of LEO, MEO and GEO satellite coverage.

5.2 Network Model and System Architecture

5.2.1 Description of Network Topology and Architecture

The system topology comprises satellite constellations in three orbits: LEO, MEO, and GEO, managed by a hybrid gateway station (HGS) through globally distributed radio units (RUs) and decentralized units (DUs) that are collocated within an Open RAN architecture. Here, the HGS is implemented in the cloud/data center, and the cloud provider is responsible for the placement of DUs/RUs, based on connectivity requirements of the users. This setup is further connected to a centralized unit (CU), which is linked to a core network, as shown in Fig. 5.1.

The satellites are configured to generate multiple beams using a channelizer, traveling wave tube amplifiers (TWTAs), and beamforming networks (BFNs) located in the satellite payloads. These beams provide coverage to various user equipment (UEs) operating under stochastic radio channel conditions, including varying weather scenarios such as CS and RFD. The UEs are classified into different traffic categories, namely URLLC, HDTV, and eMBB, each with distinct QoS/SLA requirements.

The CU of the HGS is equipped with a near-real time RIC that classifies UEs into two categories: CS and RFD. This classification is based on the CQI information reported in each UE's signaling message, after threshold verification using the energy-per-symbol-to-noise ratio (Es/No). Additionally, the RIC manages the beamforming mechanism and resource allocation patterns for the UEs. LEO and MEO satellites are equipped with inter-satellite links (ISLs) to facilitate in-space traffic routing, which is also managed by the RIC.

This study focuses on the forward transmission link, which extends from the HGS to

the satellites and ultimately to the user equipment (UE). Both DVB-S2X and 5G-NR are advanced waveform designs that are ideally suited to meet the demands of contemporary satellite communications. These designs offer several benefits, including increased spectral efficiency, lower latency, enhanced flexibility, robustness to interference, and compatibility with various access schemes. To ensure a comprehensive system, we have chosen to apply DVB-S2X to the GEO link and 5G-NR to the MEO and LEO links in our network configuration. This strategic choice leverages the strengths of each waveform based on the specific characteristics and requirements of the satellite system.

Additionally, the network design facilitates coverage and beam overlap among LEO, MEO, and GEO orbital satellites, as shown in Fig. 5.2. This design enables intra- and inter-orbital MC, enhancing capacity across the network. The network is design with Ka-band, with assumption of 4 frequency reuse pattern.

5.2.2 Downlink Transmissions Link Model

The forward transmission link involves signals transmitted from the HGS to the UEs through the satellites. This satellite link is designed employing link budget analysis including waveforms specifications that determine the transmission power, and the modulation/coding (MODCOD) to achieve a successful transmission over the stochastic channel with minimal error. In the satellite DL, the total propagation loss (L_T) in dB is:

$$L_T = L_{FSL} + L_{atm} + L_{scn} \tag{5.1}$$

where L_{atm} represents the atmospheric loss, which is calculated according to the methodology outlined in ITU-R P.676 [83], and accounts for losses due to rain fading. The term L_{scn} denotes the loss caused by tropospheric scintillation, particularly affecting the Ka band, with values obtainable following the guidance of ITU-R P.618 [84]. Finally, L_{FSL} refers to the free space loss, which depends on both the propagation distance and the carrier frequency, as detailed in [85] as follows:

$$L_{FSL} = 32.45 + 20\log_{10} F_c + 20\log_{10} d_p \tag{5.2}$$

where F_c denotes the carrier frequency in GHz, and d_p represents the propagation distance in meters. Thus, the received power in dB at a UE i from satellite s on beam k can be

calculated using the following formula:

$$C_{s,k,i} = P_k + G_k + G_i - L_T \tag{5.3}$$

where P_k represents the satellite beam transmission power in dBm, and G_k is the corresponding antenna gain, also in dBm. Additionally, G_i denotes the antenna gain of the UE i in dBi. The noise power at the receiver can be determined as:

$$N = N_f + 10\log_{10}(T_0 + (T_{ant} - T_0)10^{-0.1N_f}) + K_B + 10\log_{10}(BW) \tag{5.4}$$

where K_B is Boltzmann's constant in dBW/K/Hz, T_{ant} denotes the temperature of the receiving antenna, T_0 is the reference noise temperature, BW represents the bandwidth in Hz, and N_f is the noise figure of the receiver in dB. Consequently, the DL carrier-to-noise ratio $(C/N)_{s,k,i}$ in dB can be calculated as:

$$(C/N)_{s,k,i} = P_k + G_k + G_i - L_T - N \tag{5.5}$$

Further, the interference at UE i on the k-th beam is presented as:

$$I_{i,k} = 10log10\left(\sum_{in=1}^{N_{in}} 10^{0.1I_{in,i}}\right) \tag{5.6}$$

where $I_{in,i}$ is the interference originating from the in-th interfering beam to the i-th user:

$$I_{in,i} = EIRP_{in} + G_i - L_T \tag{5.7}$$

with in = 1,...,N_{in}, here N_{in} is number of co-channel beams and $EIRP_{in}$ is the equivalent isotropic radiation power (EIRP) from the interfering beam. Hence, the carrier to noise and interference ratio can be obtained as in [85]:

$$(C/IN)_{s,k,i} = P_{k,i} + G_{k,i} + G_i - L_T - N - I_{i,k} \tag{5.8}$$

5.2.3 Downlink Channel Model

A ray-tracing channel modeling approach from [86] is used to model the downlink channel; the space domain channel impulse response vector between satellite s and UE i at time t and

frequency F_c is given as:

$$h_i(t, F_c) = exp\{j2\pi[t\Psi_i - F_c\tau_i]\} \; . \; g_i(t, F_c) \tag{5.9}$$

where j is $\sqrt{-1}$, Ψ_i is the Doppler, τ_i is propagation delay and $g_i(t, F_c)$ is the downlink channel gain of the UE i.

Further, the channel vector $h_i(t, F_c)$ comprises of the line of sight (LoS) and non line of sight (NLoS) components according to the air-to-ground 3D channel model in [6,113], this is presented as:

$$h_i(t, F_c) = h_i^{LoS}(t, F_c) + h_i^{NLoS}(t, F_c) \tag{5.10}$$

where $h_i^{LoS}(t, F_c)$ is the deterministic LoS component and $h_i^{NLoS}(t, F_c)$ is the NLoS component.

$$\begin{aligned} h_i^{LoS}(t, F_c) &= \sqrt{\frac{\zeta_i \kappa_i}{\kappa_i + 1}} \; exp\{j2\pi[t\Psi_i^{LoS} - F_c\tau_i^{LoS}]\} \\ &\quad . \; \vee_i^{LoS} \in C^{Z_x Z_y * 1} \\ h_i^{NLoS}(t, F_c) &= \sqrt{\frac{\zeta_i}{\kappa_i + 1}} \sqrt{\frac{1}{P_{ch}}} \sum_{ch=1}^{P_{ch}} g_i(t, F_c) \\ &\quad exp\{j2\pi[t\Psi_i^{NLoS} - F_c\tau_i^{NLoS}]\} \; . \\ &\quad \vee_i^{NLoS} \in C^{Z_x Z_y * 1} \end{aligned} \tag{5.11}$$

Here κ_i is the Rician factor, $\vee$ is the channel vector, ζ_i is the large scale fading, and P_{ch} denotes the channel propagation paths of UE i.

5.2.4 Beam Gain

The transmit peak gain of the satellite beam k is presented as [114,115]:

$$G_k^{Peak} = \beta \left(\frac{70\pi}{\theta_k^{3dB}} \right)^2 \tag{5.12}$$

where β is the antenna aperture efficiency, θ_k^{3dB} is the antenna half-power beam width (HPBW) in degrees that can be controlled by BFN with the constraint discussed below.

$$\theta_k^{3dB} \geq \frac{70\lambda}{D_m F_c} \tag{5.13}$$

where F_c is the carrier frequency, D_m is the satellite antenna diameter and λ is the speed of light.

Furthermore, the resultant gain of beam k towards user i which is affected by G_k^{Peak} is denoted as

$$[G_{k,i}] = [G_k^{Peak}] - 10\log_{10}\left(12.\frac{G_k^{Peak}}{\beta}\left(\frac{\theta_{i,k}}{70\pi}\right)^2\right) \tag{5.14}$$

where [.] denotes dB value, and $\theta_{i,k}$ is the angular beam width between user i position (which is considered as x_i, y_i coordinates) and the center of the position of beam k.

$$\theta_{i,k} = tan^{-1}\left(\frac{\sqrt{(x_i - x_k^c)^2 + (y_i - y_k^c)^2}}{D_p}\right) \tag{5.15}$$

where x_k^c, y_k^c represents the coordinates of the center position of the beam k.

5.2.5 Link Achievable Capacity

The offered achievable satellite downlink capacity of the beam at user i can be computed as [116, 117]:

$$C_{s,k,j,i}^{ofd} = BW_{j,i} * \log_2\left(1 + \frac{|h_i(t, F_c)|^2 P_{k,i}\ G_{k,i}\ G_i}{N_f\ K^B\ T\ BW_{j,i}\ L_T\ I_i}\right) \tag{5.16}$$

5.2.6 Link Waveform

Waveforms play a vital role in defining standards for wireless communication technologies because they significantly affect the effectiveness of transmitting and receiving information. In satellite communications, there are two primary waveform designs in use. The first is the non-3GPP access waveform, outlined in the DVB-S2 and its extended DVB-S2X specifications. The second is a more recent standard developed by 3GPP under the 5G-NR guidelines, which aims to offer direct 5G radio access for low-gain handheld devices via satellite [49].

In DVB-S2X, MODCOD schemes are defined based on spectral efficiency considerations [118]. In 5G-NR when adapted to satellite communications, the CQI is used to convey information about the channel quality [119], and it plays a role in adaptive modulation and coding, i.e., the selection of the MODCOD schemes is conducted based on the quality of the communication channel. Therefore, to be comprehensive and address the concerns about the coexistence of both waveform designs in future satellite communications, a unified perspective is presented in Table 5.1 to represent each CQI value with its corresponding spectral efficiency

from the DVB-S2X standardization. This mapping is especially relevant for future networks and operators considering the integration of both DVB-S2X and 5G-NR technologies.

Table 5.1: Mapping of DVB-S2X MODCOD schemes to 5G-NR CQI levels

CQI	5G-NR MODCOD	5G-NR SE	DVB-S2X MODCOD	DVB-S2X SE	DVB $\frac{E_s}{N_o}$ (dBm)
3	QPSK 1/5	0.37	QPSK 2/9	0.43	-2.85
4	QPSK 1/3	0.60	QPSK 13/45	0.56	-2.03
5	QPSK 4/9	0.87	QPSK 9/20	0.88	0.22
6	QPSK 3/5	1.17	QPSK 11/20	1.08	1.45
7	16QAM 3/8	1.47	8APSK 5/9	1.64	4.73
8	16QAM 1/2	1.91	16APSK 1/2	1.97	5.97
9	16QAM 3/5	2.40	16APSK 28/45	2.45	8.10
10	64QAM 1/2	2.73	16APSK 25/36	2.74	9.27

5.3 Problem Formulation

The optimization problem, with the objective of maximizing the offered capacity $C^{ofd}_{s,k,j,i}$ is formulated in (5.17). The critical resources under consideration are the transmit power for each user $P_{k,i}$, beam gain $G_{k,i}$ and the allocated bandwidth $BW_{j,i}$; these factors play an essential role in shaping the following optimization framework

$$\max_{P_{k,i},G_{k,i},BW_{j,i},\eta_{i,s,k,j}} \quad \sum_{i=1}^{I}\sum_{s=1}^{S}\sum_{k=1}^{K}\sum_{j=1}^{J} \vartheta_i \left(C^{ofd}_{s,k,j,i}\right).\eta_{i,s,k,j} \tag{5.17a}$$

$$\text{s.t.} \quad (C1) - (C12), \tag{5.17b}$$

where I, S, K and J are the number of users, satellites, beams and component carriers (CCs) which is the frequency-time resource respectively, $BW_{j,i}$ is the bandwidth of the i-th user on the j-th CC, while $\eta_{i,s,k,j}$ is the binary resource allocation indicator for power, gain and bandwidth allocation. ϑ_i is the user traffic class identification (of either URLLC, eMBB or HDTV). The objective function has four variables to optimize including $P_{k,i}$, $G_{k,i}$, $BW_{j,i}$, and $\eta_{i,s,k,j}$, where the bandwidth $BW_{j,i}$ is a limited resource that is subject to the number of active users and the satellite constellation capacity of the network.

The objective function is subject to the constraints defined below. In C_1, the angular width between center of beam (CoB) and the user must not be smaller than antenna HPBW to ensure that all users are within beam coverage, i.e.,

$$(C_1) : \theta_{i,k} \leq \theta_k^{3dB} \quad \forall k \in K. \tag{5.18}$$

Constraint C_2 limits the satellite transmit power not to exceed P^{max} to minimize intra/inter

satellite/beam interference as follows:

$$(C_2) : P_{k,i} \leq P_k^{max} \ \forall k \in K. \tag{5.19}$$

Constraint C_3 determines the maximum number of CCs (W) that can be allocated to user i for overall satellites. This is based on 3GPP specification, and implemented in the UE chipset with appropriate antenna diversity design.

$$(C_3) : \sum_{s=1}^{S} \sum_{j=1}^{J} \eta_{i,s,k,j} \leq W \ \ \forall i \in I. \tag{5.20}$$

Furthermore, constraint C_4 ensures at most Q beams can be allocated to user i. The beams from the same satellite use orthogonal frequencies.

$$(C_4) : \max_{j \in J} \sum_{s=1}^{S} \sum_{k=1}^{K} \eta_{i,s,k,j} \leq Q \ \ \forall i \in I, \tag{5.21}$$

Constraint (C_5) shows the condition on the maximum number of satellites (M) that users can connect to as follows:

$$(C_5) : \max_{k \in K, j \in J} \sum_{s=1}^{S} \eta_{i,s,k,j} \leq M \ \ \forall i \in I. \tag{5.22}$$

Constraint C_6 ensures that the sum of the bandwidth allocated from the Ka-band, to all the users in the satellite network is not more than the maximum available system bandwidth $BW_{s,k,j}^{max}$, after the deduction of the BW capacity used for ISL. This constraint can be represented as

$$\begin{aligned} (C_6) : & \sum_{i=1}^{I} \sum_{s=1}^{S} \sum_{k=1}^{K} \sum_{j=1}^{J} \eta_{i,s,k,j}.BW_i \\ & \leq \sum_{s=1}^{S} \sum_{k=1}^{K} \sum_{j=1}^{J} BW_{s,k,j}^{max} - \varrho_{r,s} BW_{s,k,j}^{ISL}, \end{aligned} \tag{5.23}$$

where $\varrho_{r,s}$ is the ISL indicator.

Constrain (C_7) illustrates the ISL status, which is given by

$$(C_7) : \varrho_{r,s} \in \{0, 1\} \ \ \forall s \in S, \tag{5.24}$$

where $\varrho_{r,s} = 1$ means the ISL is used and $\varrho_{r,s} = 0$ otherwise. In constraint (C_8), it ensures that the C_{ofd} is equal to or exceeds the requested capacity C_i^{req} to avoid SLA violation, which is expressed as

$$(C_8) : \sum_{i=1}^{I}\sum_{s=1}^{S}\sum_{k=1}^{K}\sum_{j=1}^{J} \vartheta_i C_{s,k,j,i}^{ofd} \geq \sum_{i=1}^{I}\sum_{s=1}^{S}\sum_{k=1}^{K}\sum_{j=1}^{J} C_i^{req} \tag{5.25}$$

Constraint (C_9) considers the capacity used for ISL relay, especially for the satellites that offered capacity for ISL, to ensure that only available capacity after ISL capacity deduction is offered to satisfy users' demand. It can be represented as

$$(C_9) : \sum_{s=1}^{S}\sum_{k=1}^{K}\sum_{j=1}^{J} \vartheta_i C_{s,k,j,i}^{ofd} \leq \sum_{s=1}^{S}\sum_{k=1}^{K}\sum_{j=1}^{J} C_s^{tot} - \varrho_{r,s} C_{r,s}^{ofd} \tag{5.26}$$

where C_s^{tot} is the total available capacity in satellite s.

Constraints (C_{10}), (C_{11}) and (C_{12}) enforce user-to-satellite association. They guarantee that the appropriate satellite beam gain, power and delay are mapped to the UE i respectively, based on the traffic class of the user to allow for SLA satisfaction.

$$(C_{10}) : G_{k,i}^{*} = \begin{cases} \{G_{k,i}^{LEO}\} & \text{if } \vartheta_i = URLLC \\ \{G_{k,i}^{LEO}, G_{k,i}^{MEO}\} & \text{if } \vartheta_i = eMBB \\ \{G_{k,i}^{MEO}, G_{k,i}^{GEO}\} & \text{if } \vartheta_i = \ HDTV \\ 0 & otherwise \end{cases} \tag{5.27}$$

$$(C_{11}) : P_{k,i}^{*} = \begin{cases} \max(P_{k,i}^{LEO}) & \text{if } \vartheta_i = URLLC \\ \max(P_{k,i}^{LEO}, P_{k,i}^{MEO}) & \text{if } \vartheta_i = eMBB \\ \max(P_{k,i}^{MEO}, P_{k,i}^{GEO}) & \text{if } \vartheta_i = \ HDTV \\ 0 & otherwise \end{cases} \tag{5.28}$$

$$(C_{12}) : D_{i}^{*} = \begin{cases} \max(D_{s,i}^{LEO}) & \text{if } \vartheta_i = URLLC \\ \max(D_{s,i}^{LEO}, D_{s,i}^{MEO}) & \text{if } \vartheta_i = eMBB \\ \max(D_{s,i}^{MEO}, D_{s,i}^{GEO}) & \text{if } \vartheta_i = \ HDTV \\ 0 & otherwise \end{cases} \tag{5.29}$$

5.4 Optimization Solution for Beam and Resource Allocation

The optimization problem (5.17) is a non-convex combinatorial problem, characterized by certain non-convex constraints and sets which are discrete in nature, making it inherently NP-hard. Traditional methods, including convex optimization techniques, are unable to solve this problem optimally within an acceptable time frame. Hence, the problem is solved by first decoupling it into the following two sub-problems: dynamic beam allocation and joint power and bandwidth allocation.

5.4.1 Sub-problem 1: Dynamic Beam Allocation Optimization Solution with Iterative Approach

This sub-problem aims to maximize $G_{k,i}$ from (5.14) by minimizing $\theta_{i,k}$, which is expressed as

$$\underset{\theta_{i,k}}{max} \quad \sum_{i=1}^{I}\sum_{s=1}^{S}\sum_{k=1}^{K} G_{k,i} \tag{5.30a}$$

$$\text{s.t.} \quad (C1). \tag{5.30b}$$

To solve this problem, an iterative algorithm is applied, which operates by varying random values of the user's angular width, $\theta_{i,k}$. This parameter, representing the user's position respective to the serving satellite beam, changes due to the assumption of the ISL, enabling dynamic beam placement by different satellites, thereby affecting $G_{k,i}$.

5.4.2 Sub-problem 2: Joint Power and Bandwidth Allocation Optimization Solution

Given the beam allocation achieved by addressing sub-problem 1 in (5.30), the objective of this sub-problem 2 is to develop a joint power and bandwidth allocation strategy to maximize the offered capacity, which is expressed as

$$\underset{P_{k,i},BW_{j,i},\eta_{i,s,k,j}}{max} \quad \sum_{i=1}^{I}\sum_{s=1}^{S}\sum_{k=1}^{K}\sum_{j=1}^{J} \vartheta_i \left(C_{s,i}^{ofd}\right).\eta_{i,s,k,j} \tag{5.31a}$$

$$\text{s.t.} \quad (C_2) - (C_{12}). \tag{5.31b}$$

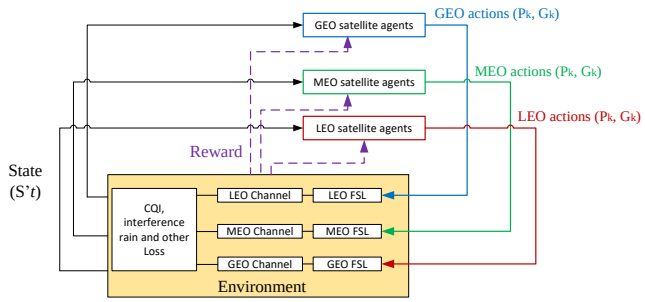

Figure 5.3: The MDP involving agents and environment interaction in MADRL for Multi-layer NTN.

To address this problem that has dynamic and time-varying features, MADRL-based joint power and bandwidth assignment solutions are developed, where different MADRL techniques are investigated.

5.5 Resource Allocation with Multi-Agent Deep Reinforcement Learning

An MADRL approach is used to derive optimal solutions for $P_{k,i}$, $G_{k,i}$, $BW_{j,i}$, and $\eta_{i,s,k,j}$, serving as an effective strategy for optimizing (5.17). The problem is tackled in a distributed manner, with each agent independently selecting its actions while adhering to specific constraints. Despite operating in interconnected and divergent environments with varying transmission properties, the actions of the agents differ. The problem's complexity, arising from its dynamic and time-varying nature and the large number of variables involving satellites and users, makes RL an appropriate solution approach.

5.5.1 Markov decision process

The Markov decision process (MDP) provides a framework involving states, actions, and rewards, as illustrated in Fig. 5.3. In this study, the MDP for MADRL is defined as a tuple with four components: $(S^{\dagger}, A^{\dagger}, P^{\dagger}(s_{t+1}|s_t, a_t), R^{\dagger})$. Here, $S^{\dagger}$ represents the set of states, $A^{\dagger}$ denotes the set of actions taken by the agents (LEO, MEO, and GEO satellites), $P^{\dagger}(s_{t+1}|s_t, a_t)$ is the set of transition probabilities from state s_t to state s_{t+1} after executing action $a_t \in A^{\dagger}$, and $R^{\dagger}$ indicates the reward function resulting from the actions $A^{\dagger}$.

- **Action**: The agents $x \in X$ observe the environment, which comprises dynamic values

of CQI, user traffic class and L_{FSL}, and sense the state before taking actions, which involves selecting the beam gain $G_{k,i}$ and beam power $P_{k,i}$ collectively, in a discretized manner as

$$a_t \in A^{\dagger} = \{1, 2..., NM\}, \tag{5.32}$$

where X denotes the agent set including LEO, MEO, and GEO satellites. Basically, the action space is discrete such that power is quantized into M levels that result in $P_{k,i} = P_{k,i}^{max}/M$ $(i \in \{1, 2.., M\})$. Similarly, beam gain is in N levels, that is $G_{k,i} = G_{k,i}^{max}/N$ $(i \in \{1, 2.., N\})$. Hence the action space of agent x is NM, while the action space of the entire agents is $(NM)^X$. The values of $G_{k,i}$ and $P_{k,i}$ differ for the respective agents of LEO, MEO and GEO satellites as defined in Table 5.2. To obtain an optimal policy, the action selection of each agent can be deployed based on the ϵ-greedy strategy to balance the exploration-exploitation trade-off during the learning process, which is expressed as

$$a_t = \begin{cases} \text{random action}, & \text{if probability } \epsilon \\ \arg\max\limits_{a \in A^{\dagger}} \{Q(s_t, a)\}, & \text{probability } 1 - \epsilon \end{cases} \tag{5.33}$$

This action function operates under two distinct conditions. The first condition involves selecting a random action with a probability of ϵ to encourage environment exploration. The second condition emphasizes the exploitation of accumulated learning experiences by choosing the best action based on Q-value function $Q(s_t, a)$ with probability of $1-\epsilon$, where ϵ gradually decreases after each action taken according to a ϵ-decay rate.

- **State**: The state space is designed by the number of actions NM taken by the agent, represented as:

$$S^{\dagger} = \{1, 2..., NM\}. \tag{5.34}$$

Thus the state of an agent $x \in X$ at a time-slot t is defined as the combination of the previously selected beam gain $G_{k,i}$ and beam power $P_{k,i}$ in time-slot $t-1$, given as:

$$s_t = \{P_{k,i,t-1}, G_{k,i,t-1}\} \in S^{\dagger}. \tag{5.35}$$

The state is formulated based on the local information available to the agent, aiming to reduce the signaling overhead between the agent and the environment [120]. It is noteworthy that in (5.35), the agent's state has a cardinality of 2.

- **Reward Function**: The actions selected by the agents lead to corresponding rewards, which are granted only if the constraints in problem (5.17) are satisfied. The reward mechanism is decentralized, meaning each agent receives a distinct reward. This approach is effective because the agents select unique actions that differ from one another, resulting in varying reward values. This allows the agents to properly learn the actual outcomes of their specific actions. The reward function used is based on the objective function of the offered capacity, where offered capacity is in bps. The reward function is expressed as:

$$r_t = \sum_{i=1}^{I}\sum_{s=1}^{S}\sum_{k=1}^{K}\sum_{j=1}^{J} \vartheta_i \left(C_{s,i}^{ofd}\right).\eta_{i,s,k,j} \in R^{\dagger}. \tag{5.36}$$

5.5.2 Bandwidth Allocation

The allocation of $BW_{j,i}$ is implemented using (5.37) by the proposed algorithm (DyBM-RA). This allocation is carried out when the single carrier (SC) bandwidth, denoted as BW_{sc}, is known and specified as:

$$BW_{j,i} = K_i * BW_{sc}. \tag{5.37}$$

where K_i represents the number of CCs generated to meet the required bandwidth allocation $BW_{j,i}$, and it is expressed as:

$$K_i = \left(\frac{W_i^c * BW_{s,k}^{tot}}{I_\vartheta}\right) * \frac{1}{BW_{sc}}. \tag{5.38}$$

This is determined by the bandwidth allocation weight, W_i^c, for user i within a specific CQI channel category, either CS or RFD, where $0 \leq W_i^c \leq 1$. It also depends on the total number of users, I_ϑ, within the specific traffic class ϑ under consideration, such as URLLC, HDTV, or eMBB. Here, BW^{tot} represents the total available bandwidth. Finally, the actual resource allocation, $\eta_{i,s,k,j}$, is determined using C_{10}, C_{11}, and C_{12}, where K_i, $G_{k,i}^*$, $P_{k,i}^*$, and $D_{s,i}^*$ are restricted to specific orbital satellites based on ϑ_i.

5.5.3 Proposed Algorithm

The Q-learning algorithm, a reinforcement learning (RL) method, operates by maintaining a Q-table that records Q-values, which represent state-action pairs. Each state-action pair has an associated value that is considered a reward. During the training phase, the Q-values are continuously updated until the Q-table converges. This update is performed using [121]:

$$\begin{aligned} Q(s_t, a_t) \ &= Q(s_t, a_t)(1-\alpha) + \alpha[r_{t+1} \\ &\quad +\gamma \max_a Q(s_{t+1}, a)] \end{aligned} \tag{5.39}$$

where α is the learning rate, and γ is the discount factor.

Generally, Q-learning is best suited for small state and action spaces. As these spaces grow larger, deriving an optimal solution from the extensive Q-table becomes challenging. Therefore, the MADRL approach is employed by the DyBM-RA algorithm to effectively solve the resource allocation problem in (5.17), aiming to maximize the offered capacity. With the DRL methodology, a deep neural network (DNN) is incorporated into the Q-learning algorithm, leading to a reduction in memory and computational complexity. This is achieved by defining different layers in the DNN to derive the best action for the respective states, rather than relying on a large storage space (Q-table) for storing Q-values [121]. In this Chapter, the MADRL approach includes the use of deep Q-networks (DQN), double DQN (2DQN), and dueling double DQN (3DQN) models, which are further explained as in [120].

DyBM-RA with MADQN Approach

In this approach, each agent develops its own DQN model, which consists of two DNNs: the online network and the target network, as illustrated in Fig. 5.4(a). At each time step t, agent x employs the online network to approximate the Q-function $Q(s_x(t), a_x(t); \delta_x)$ to select an action $a_x(t) \in A_x^\dagger$ when it is in state $s_x(t) \in S_x^\dagger$. The parameters and weights for agent x in the online network are denoted as δ_x. The target network serves to stabilize the learning process with its parameters $\overline{\delta_x}$, which are updated periodically by copying the parameters from δ_x of the online network, a process referred to as frequency parameter update.

For action selection, the ϵ-greedy policy, as expressed in (5.33), is employed to balance exploration and exploitation throughout the learning phase. This approach helps determine the optimal policy for selecting the best learned action.

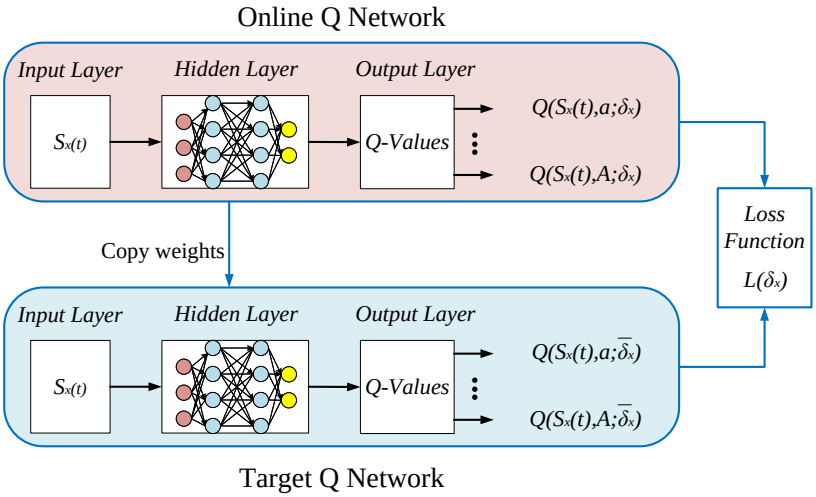

(a) DQN/2DQN model architecture.

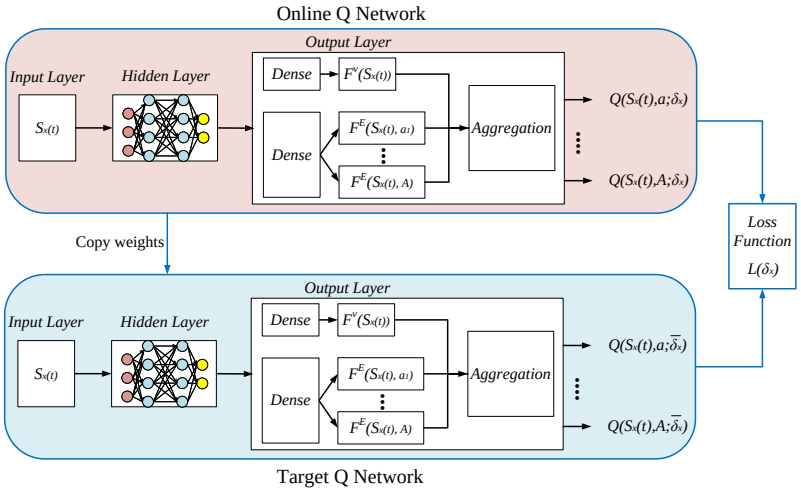

(b) 3DQN model architecture.

Figure 5.4: Illustration of the DQN, 2DQN and 3DQN model architecture [120].

Additionally, MADQN leverages the experience replay mechanism to enhance learning stability. During the learning process, transitions in the form of tuples $(s_x(t), a_x(t), r(t), s_x(t+1))$ are stored in the experience replay memory of each agent x. In each iteration, a mini-batch of these experiences is uniformly sampled to train the model and update the parameters of the online network δ_x, with the goal of minimizing the loss function, which is given by:

$$L_x(\delta_x) = [y_m(t) - Q(S_x(t+1), a; \delta_x)]^2 \tag{5.40}$$

Here, $y_m(t)$ represents the target value obtained from the target network, which is:

$$y_m(t) = \left(r(t) + \gamma \max_{a \in A} Q(S_x(t+1), a; \overline{\delta_x}) \right) \tag{5.41}$$

DyBM-RA with MA2DQN Approach

In the MADQN approach expressed in (5.40), the same Q-value function is used for both action selection $\max_{a \in A} Q(S_x(t+1), a; \overline{\delta_x})$ and action estimation $Q(S_x(t+1), a; \overline{\delta_x})$. This can result in instability during the learning or training process due to overestimation of the Q-value function. To address this issue, the DyBM-RA approach incorporating MA2DQN introduces the 2DQN model [122], [123], [124], as illustrated in Fig. 5.4(a). The 2DQN model separates action selection from evaluation to mitigate overestimation by adjusting the target value in (5.41) as follows:

$$y_m(t) = r(t) + \gamma Q \left(s_x(t+1), \max_{a \in A} Q_x(t+1); \overline{\delta_x} \right) \tag{5.42}$$

Here $Q_x(t+1) = Q(s_x(t+1), a; \delta_x)$. The online network $Q(s, a; \delta_x)$ is employed for action selection, while for action estimation, the target network $Q(s, a; \overline{\delta_x})$ is used.

DyBM-RA with MA3DQN Approach

The DyBM-RA with MA3DQN approach employs the 3DQN model [121], whose architecture is depicted in Fig. 5.4(b), enhancing the learning efficiency of the DyBM-RA algorithm. In this method, agent x develops its 3DQN model from the 2DQN model by splitting the final layer into two components: the state value function (VF) $F^V(s_x(t))$ and the advantage function (AF) $F^E(s_x(t), a_x(t))$. The $F^V(s_x(t))$ function estimates the quality of the state $s_x(t)$, helping the agent assess the long-term potential of that state. In contrast, the $F^E(s_x(t), a_x(t))$ function measures the relative quality of an action compared to others within the same state $s_x(t)$. These functions are combined to calculate the joint action-value function $Q(s_x(t), a_x(t); \delta_x, \delta^{F^V} x, \delta^{F^E} x)$, which is used for action selection in a multi-orbital satellite environment. Here, $\delta^{F^V} x$ and $\delta^{F^E} x$ denote the VF and AF parameters, respectively. Consequently, the action-value function for agent x in state $s_x(t)$ with action $a_x(t)$ is:

Algorithm 5: Iterative Method for Dynamic Beam Allocation to Obtain $G_{k,i}$

Initialize Parameters: - π
- $\lambda \leftarrow$ // Speed of light (m/s)
- Fc $\leftarrow$ // Carrier frequency (Hz)
- dm $\leftarrow$ // MEO Antenna diameter (m)
- LeoMin, MeoMin, GeoMin $\leftarrow$ // Minimum values
- AtEff_Leo, AtEff_Meo, AtEff_Geo $\leftarrow$ // Antenna efficiencies for LEO, MEO and GEO

Compute Beam 3dB HPBW:
- Leo3dB_HPBW $\leftarrow$ 1.76, Geo3dB_HPBW $\leftarrow$ 0.17 // **From 3GPP** [68]
- Meo3dB_HPBW $\leftarrow \dfrac{70 \times \lambda}{dm \times Fc}$ using (5.13)

Compute Peak Beam Gain:
- LeoPeakBeamGain $\leftarrow$ 38.5, GeoPeakBeamGain $\leftarrow$ 58.5 **From 3GPP** [68]
- Using (5.12), get MeoPeakBeamGain

$\leftarrow 10 \cdot \log_{10}\left(AtEff\_Meo \cdot \left(\dfrac{70 \cdot \pi}{Meo3dB\_HPBW}\right)^2\right)$

Convert to Absolute Peak Beam Gain:
- Leo_absoluteGain $\leftarrow$ dBiToAbsolute(LeoPeakBeamGain)
- Meo_absoluteGain $\leftarrow$ dBiToAbsolute(MeoPeakBeamGain)
- Geo_absoluteGain $\leftarrow$ dBiToAbsolute(GeoPeakBeamGain)

Function dBiToAbsolute($dBiGain$): Return $10^{(dBiGain/10)}$

Define Random User Theta Angular Width:
- Leotheta $\leftarrow$ linspace(LeoMin, Leo3dB_HPBW, 10)
- Meotheta $\leftarrow$ linspace(MeoMin, Meo3dB_HPBW, 10)
- Geotheta $\leftarrow$ linspace(GeoMin, Geo3dB_HPBW, 10)

Compute Beam Gain with (5.14):
- Leo_beam_gain $\leftarrow$ LeoPeakBeamGain $- 10 \cdot \log_{10}\left(12 \cdot \dfrac{Leo\_absoluteGain}{AtEff\_Leo} \cdot \left(\dfrac{Leotheta}{70 \cdot \pi}\right)^2\right)$
- Meo_beam_gain $\leftarrow$ MeoPeakBeamGain $- 10 \cdot \log_{10}\left(12 \cdot \dfrac{Meo\_absoluteGain}{AtEff\_Leo} \cdot \left(\dfrac{Meotheta}{70 \cdot \pi}\right)^2\right)$
- Geo_beam_gain $\leftarrow$ GeoPeakBeamGain $- 10 \cdot \log_{10}\left(12 \cdot \dfrac{Geo\_absoluteGain}{AtEff\_Leo} \cdot \left(\dfrac{Geotheta}{70 \cdot \pi}\right)^2\right)$

Create Beam Gain Matrices:
- Leo_beam_gain_matrix, Meo_beam_gain_matrix, Geo_beam_gain_matrix $\leftarrow$ matrices matching *Leotheta*, *Meotheta*, and *Geotheta* lengths

for i *in* $\{1, length(Leotheta)\}$ **do**
    Fill Leo_beam_gain_matrix(i, :) with Leo_beam_gain

for ii *in* $\{1, length(Meotheta)\}$ **do**
    Fill Meo_beam_gain_matrix(i, :) with Meo_beam_gain

for iii *in* $\{1, length(Geotheta)\}$ **do**
    Fill Geo_beam_gain_matrix(i, :) with Geo_beam_gain

$$Q\left(s_x(t), a_x(t); \delta_x, \delta_x^{F^V}, \delta_x^{F^E}\right) = F^V(s_x(t)) + F^E(s_x(t), a_x(t)) - \frac{1}{|A_x|}\sum_{a\in A_x} F^E(s_x(t), a_x(t)) \tag{5.43}$$

The term subtracted in (5.43) accounts for the mean value of the AF across all actions. This subtraction from the AF of a specific action centers the AF around zero, which facilitates more effective network training. This method enhances the stability and convergence of the neural network while providing adequate separation of VF and AF estimations. As a result, it offers better performance compared to the DQN and 2DQN models.

The DyBM-RA algorithms operate by classifying the UEs into CQI groups of CS and RFD based on their CQI values and MODCOD requirements. It then identifies the traffic demand class with the SLA requirements of the UEs, categorizing them as URLLC, HDTV, or eMBB, as outlined in Algorithm 6. The solution to (5.30) is derived using iterative algorithm, which is presented in Algorithm 5. The proposed algorithm subsequently performs the MADRL operation, where the agents X (LEO, MEO, and GEO) select actions $a_t \in A^{\dagger}$, such as $P_{k,i}$ and $G_{k,i}$ allocation with $BW_{j,i}$ and the association policy $\eta_{i,s,k,j}$, based on CQI and traffic class, after observing the current state $s_x(t) \in S_x^{\dagger}$. These actions result in a reward r_t based on the offered capacity $C_{s,i}^{ofd}$, and the agent transitions to a new state $s_x(t+1)$. DyBM-RA stores an experience tuple $(s_x(t), a_x(t), r_x(t), s_x(t+1))$ in the experience replay memory, and a minibatch of experiences is sampled to train the online Q-network. The parameters δ_x are updated to minimize the loss function $L_x(\delta_x)$ (5.40) using stochastic gradient descent, with the target values defined in (5.41), (5.42), and (5.42) for the MADQN, MA2DQN, and MA3DQN approaches, respectively. The parameters $\overline{\delta_x}$ are updated using δ_x. After a series of training episodes, the DyBM-RA algorithm proceeds to the testing phase, where actions a_t are selected based on the learned policies.

5.5.4 Complexity Analysis

The complexity of algorithm 5 is subject to the cardinality of the set of $\theta_{i,k}$, which is represented as $L_{\theta_{i,k}}$. Hence the complexity is $O(L^2_{\theta_{i,k}})$ [125] and it increases as $L_{\theta_{i,k}}$ increases. The complexity of Algorithm 6 is influenced by the number of *episodes* and *time step* t configured. Specifically, the complexity of DyBM-RA is $O(E^pT)$, where T represents the maximum number of *time steps* configured in each *episode*, and E^p denotes the maximum number of *episode* [126]. When multiple agents X are involved, the complexity increases to $O(XE^pT)$.

Algorithm 6: DyBM-RA with Multi-Agent DRL

Input: I = Total number of users; BW^{tot} = Total available bandwidth; BW_{sc} = Single carrier bandwidth; *Training Episode*, *Testing Episode*, *Timestep*, ϵ, $\epsilon - decay$, α, γ.

User CQI classification based on MODCOD
Under RFD => CQI 3 - 6
Under CS => CQI 7 - 10
User demand identification based on traffic and SLA
SLA˙1 => *URLLC*
SLA˙2 => *HDTV*
SLA˙3 => *eMBB*
Solve subproblem 1: (5.30) for $G_{k,i}$ **with iterative algorithm**
Multi-Agent RL Setup with DQN, 2DQN, 3DQN
Initialize *environment* **with parameters**;
Initialize the *Online Network* (Q_{online}) **and** *Target Network* (Q_{target}) **for each agent**;
Define the BW_u **and user-to-network association policy**;
while $i \leq I$ *(solving for* $\eta^*_{i,s,k,j}$ *and* $BW_{j,i}$*)* **do**
    Associate users based on traffic/SLA class using (5.27, 5.28, 5.29)
    Derive BW using: $BW_{j,i} = K_i * BW_{sc}$;
    $K_i = \left(\frac{W_i^c * BW_{s,k}^{tot}}{I_\vartheta}\right) * \frac{1}{BW_{sc}}$
end
Training Procedure: for $ep \leftarrow 1$ *to Training Episode* **do**
    Randomly select initial state s_0;
    for $st \leftarrow 1$ *to Timesteps* **do**
        Choose actions LEO_{action}, MEO_{action}, GEO_{action} **based on epsilon-greedy policy using** Q_{online};
        Take actions using (5.33) and receive rewards while considering all constraints especially C_8;
        Store transitions (s_t, a_t, r_t, s_{t+1}) *in replay memory*;
        Sample a mini-batch of transitions from replay memory;
        Evaluate the loss function:;
        For MADQN => Use (5.40) and (5.41);
        For MA2DQN => Use (5.40) and (5.42);
        For MA3DQN => Use (5.40) and (5.42), calculate Q-value with (5.43);
        Update δ_x **using stochastic gradient to minimize** $L_x(\delta_x)$;
        Update Q_{online} *using the Bellman equation:*
        $Q_{online}(s_t, a_t) = Q_{online}(s_t, a_t)(1 - \alpha) + \alpha[r_{t+1} + \gamma \max_a Q_{target}(s_{t+1}, a)]$;
        Update Q_{target} **with** Q_{online} **periodically**;
        Decay exploration rate ϵ;
    end
end
Testing Procedure: **for** $ep \leftarrow 1$ *to Test Episode* **do**
    for $st \leftarrow 1$ *to Timesteps* **do**
        Choose actions LEO_{action}, MEO_{action}, GEO_{action} **based on learned policies using** Q_{online};
        Take actions and receive rewards while considering constraints C_8**;**
    end
end
Export and plot results

Table 5.2: Wireless and MADRL Simulation Parameters

Wireless Network Parameters	**Values**
Satellite altitude LEO, MEO and GEO (Km)	1,200, 10,000, 35,786
Channel model	Rician
Rician K-factor	10
Number of URLLC, mMTC, eMBB and total users	500, 1,000, 1,000, 2,500
Number of LEO, MEO, GEO satellites	450, 90, 3
LEO, MEO, GEO BW per satellite (MHz)	100, 1,000, 45,500
Peak Gain for LEO, MEO, GEO (dBi)	38.5, 54, 58
3dB beam-width LEO, MEO, GEO (degrees)	1.76, 0.35, 0.17
User Gain (dBi)	39.7
Noise figure (dB)	1.2
Rain loss (dB)	25
P_s^{max} of LEO, MEO, GEO (dBw)	4, 8, 12
Carrier frequency (GHz)	20
Waveform LEO, MEO and GEO	5GNR, 5GNR and DVB-S2x
CQI range for CS and RFD	7 - 10; 3 - 6
MADRL Parameters	**Values**
Training, testing Episode	300, 50
Number of learning steps	10
epsilon (ϵ)	1
epsilon minimum (ϵ_{min})	0.001
epsilon-decay	0.99
Learning rate (α)	0.001
Discount factor (γ)	0.9
Number of hidden layers	3
Number of neurons of hidden layers	256, 128, 64
Batch size	32
Optimizer	Adam

Additionally, considering the architecture of the neural network used in DyBM-RA, the complexities for DyBM-RA with MADQN and DyBM-RA with MA2DQN are as follows [120]:

$$\mathbb{C}^{MADQN} = \mathbb{C}^{MA2DQN} = O(XE^pT(Z^I N_1 + \sum_{l=1}^{L-1} N_l N_{l+1})) \tag{5.44}$$

where L is the number of layers, N_L is the number of neurons in layer l, and Z^I is the size of the input layer.

The complexity of DyBM-RA with MA3DQN is higher than that of the other two methods, primarily due to the dueling network architecture. The complexity is expressed as

$$\mathbb{C}^{MA3DQN} = O(XE^pT(Z^I N_1 + \sum_{l=1}^{L-1} N_l N_{l+1} + N_{L-1})) \tag{5.45}$$

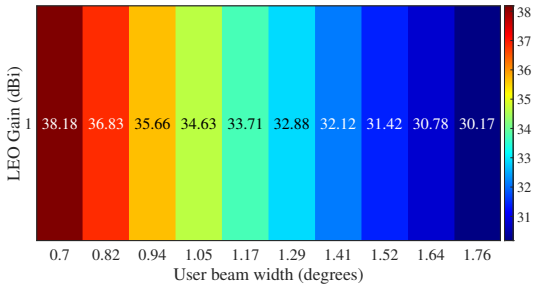

(a) LEO Gain in dBi with respect to user angular beamwidth.

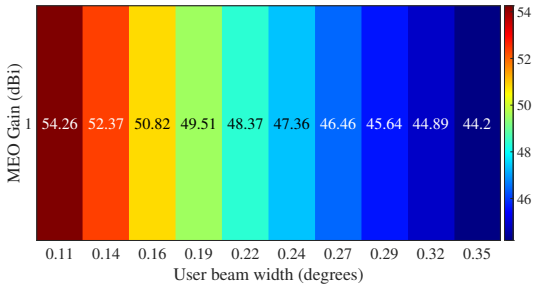

(b) MEO Gain in dBi with respect to user angular beamwidth.

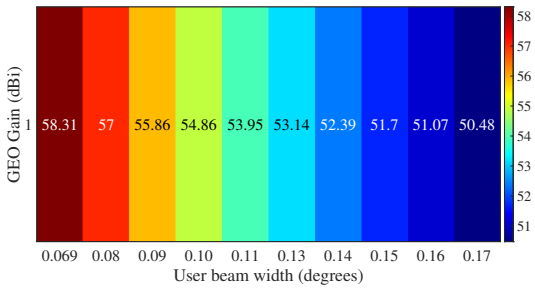

(c) GEO Gain in dBi with respect to user angular beamwidth.

Figure 5.5: Satellite beam gain evaluation for LEO, MEO and GEO with dynamic parameters.

5.6 Performance Evaluation

5.6.1 Simulation Setup

The simulation is initially set up to solve the problem in equation (5.30), aiming to derive different values of $G_{k,i}$ using the iterative algorithm described in Chapter 5.4.1. The iterative algorithm is configured in MATLAB with the parameters outlined in Table 5.2. Similarly, the DyBM-RA algorithm, which incorporates MADRL with MADQN, MA2DQN, and MA3DQN models, is implemented in Python to address the problem in equation (5.31), using the parameters specified in Table 5.2. The system used for the simulations runs Windows 10 64-bit with 32 GB of RAM and 16 Intel 2.40 GHz cores. The simulation software employed includes Python 3.9.18 and MATLAB R2023b.

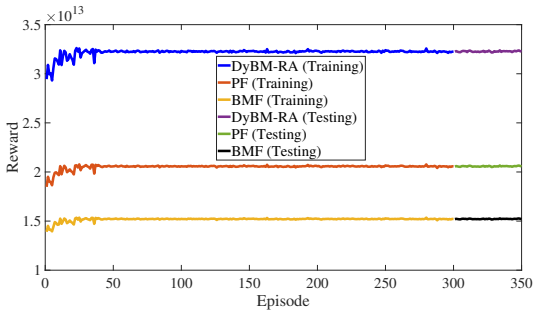

(a) DQN MADRL reward performance.

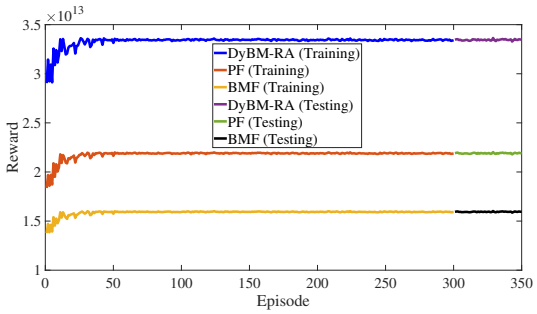

(b) 2DQN MADRL reward performance.

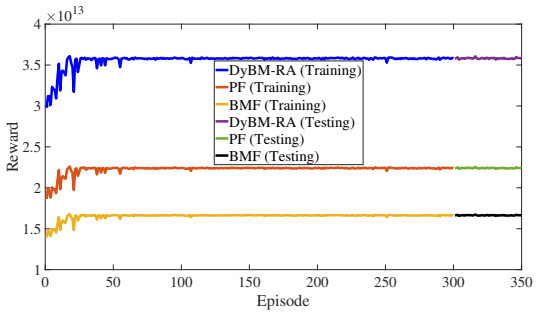

(c) 3DQN MADRL reward performance.

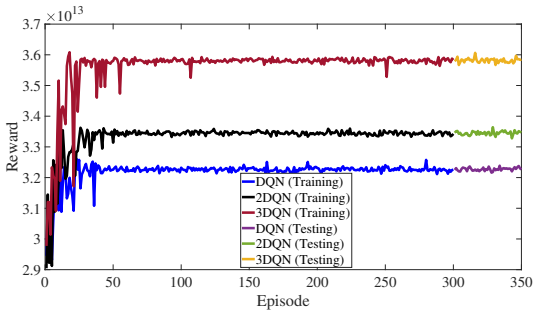

(b) Evaluation of DyBM-RA with DQN, 2DQN and 3DQN.

Figure 5.6: Evaluation of the various MADRL algorithms while considering the different resource allocation algorithms of DyBM-RA, PF and BMF.

5.6.2 Benchmark Algorithms

This proposed algorithm is compared with other state-of-the-art algorithms based on the resource allocation mechanism, which are discussed below.

Proportional Fairness Algorithms

The Proportional Fairness (PF) algorithm [127] allocates bandwidth resources fairly to all UEs, using the same ratio of W_i^c for both CS and RFD users.

Bottleneck Max Fairness Algorithms

The Bottleneck Max Fairness (BMF) algorithm [128] allocates more bandwidth to RFD UEs who experience poor channel conditions, such as an additional 25 dBm rain loss. This approach results in a higher ratio of W_i^c for RFD UEs compared to CS UEs.

5.6.3 Performance Analysis

The results for the optimization of gain $G_{k,i}$ for the LEO constellation are presented in Fig. 5.5(a). The figure shows how different values of $G_{k,i}$ vary as the user's angular beam width

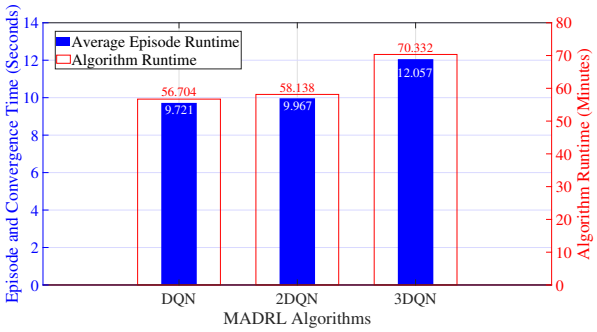

Figure 5.7: MADRL episode and overall run time analysis for the different algorithms.

$\theta_{i,k}$ changes, which is influenced by the velocity of the UE or satellites. The LEO gain $G_{k,i}$ improves and increases as $\theta_{i,k}$ decreases, indicating that the UE is closer to the center of the beam. This is achieved with inter-satellite links (ISLs), where relay satellites route traffic to the satellite that is best positioned to serve the UE based on $\theta_{i,k}$ resulting in the optimal value of $G_{k,i}$. The highest $G_{k,i}$ of 38.18 dBi is obtained when $\theta_{i,k}$ is 0.7 degrees. Similarly, for MEO, the highest $G_{k,i}$ of 54.26 dBi is achieved at $\theta_{i,k}$ of 0.11 degrees, as shown in Fig. 5.5(b). In Fig. 5.5(c), the value of $G_{k,i}$ for GEO is 58.31 dBi at $\theta_{i,k}$ of 0.069 degrees.

Further, Fig. 5.6(a) presents the reward performance of the MADQN for the DyBM-RA, PF, and BMF algorithms. It is observed that DyBM-RA outperforms PF and BMF. This superior performance is due to the resource allocation strategy where DyBM-RA allocates $BW_{j,i}$ with a higher ratio of weight W_i^c to CS UEs compared to RFD UEs. In contrast, PF and BMF algorithms allocate resources differently, as described in Chapter 5.6.2. A similar trend is observed in Fig. 5.6(b) for MA2DQN, where DyBM-RA also performs better than PF and BMF. For MA3DQN, as shown in Fig. 5.6(c), DyBM-RA continues to outperform PF and BMF.

In Fig. 5.6(d), the performance of DyBM-RA with MADQN, MA2DQN, and MA3DQN approaches is evaluated. The MA3DQN approach yields the highest reward of 3.58×10^{13} after convergence, compared to MA2DQN and MADQN, which result in rewards of 3.34×10^{13} and 3.22×10^{13}, respectively. DyBM-RA with MA3DQN achieves the best performance due to the dueling architecture and robust mechanism described in Chapter 34. However, DyBM-RA with MA3DQN has the drawback of a longer algorithm runtime of 70.33 minutes, with an average episode runtime of 12.05 seconds, as shown in Fig. 5.7. In comparison, DyBM-RA with MA2DQN and DyBM-RA with MADQN have runtimes of 58.13 minutes (with an average episode time of 9.96 seconds) and 56.70 minutes (with an average episode time of 9.72 seconds), respectively. This indicates that DyBM-RA with MA3DQN has runtimes that are

18.99% and 21.45% longer than DyBM-RA with MA2DQN and DyBM-RA with MADQN, respectively, due to the complexity of MA3DQN as described in Chapter 5.5.4.

Additionally, Fig. 5.8(a) shows that as P-Max (a component of agent action $P_{k,i}$) increases, the sum rate also increases. Specifically, DyBM-RA achieves a performance of 34.99 Tbps at 12 dBW, whereas PF and BMF achieve sum rates of 22.15 Tbps and 16.36 Tbps, respectively. This demonstrates that DyBM-RA outperforms PF and BMF by 44.94% and 72.56%, respectively. Similarly, Fig. 5.8(b) shows that as Gain $G_{k,i}$ (the second component of the agent action) increases, the sum rate rises. DyBM-RA achieves a sum rate of 30.05 Tbps at $G_{k,i}$ of 60 dBi, while PF and BMF yield sum rates of 21.73 Tbps and 16.24 Tbps, respectively. This shows that DyBM-RA outperforms PF and BMF by 32.13% and 59.66%, respectively.

In Fig. 5.9, it is shown that as $P_{k,i}$ increases, energy efficiency (EE) decreases. DyBM-RA yields an EE of 0.64 b/J at P-Max of 4 dBW, while PF and BMF achieve EEs of 0.39 b/J and 0.29 b/J, respectively. This indicates that DyBM-RA outperforms PF and BMF in EE by 48.54% and 75.26%, respectively. Similarly, in Fig 5.10, spectral efficiency (SE) increases with P-Max. DyBM-RA achieves an SE of 129.61 bps/Hz at 12 dBW, whereas PF and BMF yield SE of 82.07 bps/Hz and 60.61 bps/Hz, respectively. This indicates that DyBM-RA outperforms PF and BMF in terms of SE by 44.91% and 72.54%, respectively.

Further, Fig. 5.11 confirms that as the number of CCs K_i increases, the sum rate also increases, highlighting the impact of intra/inter orbital MC. DyBM-RA achieves a sum rate of 155.68 Tbps with 5 K_i, while PF and BMF yield sum rates of 98.08 Tbps and 72.74 Tbps, respectively. This shows that DyBM-RA outperforms PF and BMF by 98.08% and 72.62%, respectively.

Additionally, the impact of user-to-satellite association is evaluated in Fig. 5.12, specifically constraint C_{12}, which is a requirement to satisfy SLA for URLLC traffic. It is observed that DyBM-RA, which enforces association for URLLC to LEO satellites only, achieves a peak delay of 51.66 ms with 500 UEs. In contrast, when the association is random, with UEs distributed across GEO, MEO, and LEO satellites, the URLLC peak delay is 404.40 ms. This demonstrates that DyBM-RA satisfies the SLA requirements for the URLLC traffic class.

Finally, it is confirmed that the proposed DyBM-RA with MA3DQN outperforms DyBM-RA with MA2DQN and DyBM-RA with MADQN due to the dueling architecture of the MA3DQN model. However, DyBM-RA with MA3DQN has the drawback of increased com-

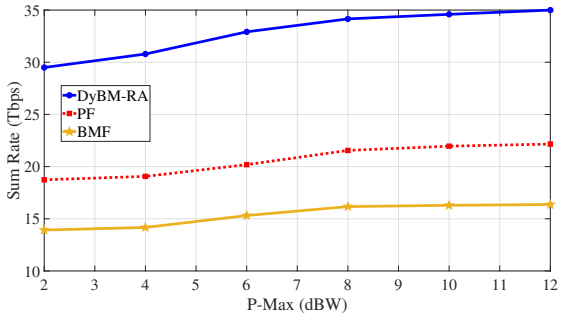

(a) Evaluation of sum rate vs P-Max.

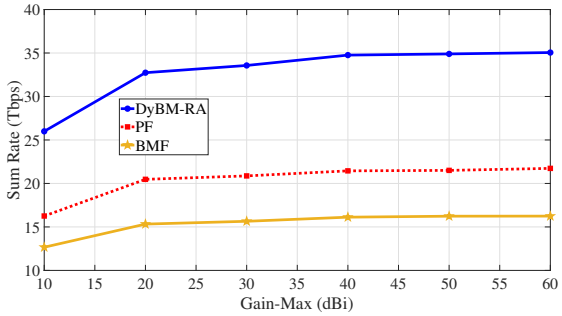

(b) Evaluation of sum rate vs Gain.

Figure 5.8: Evaluation of the sum rate with respect to P-Max and Gain for the different algorithms.

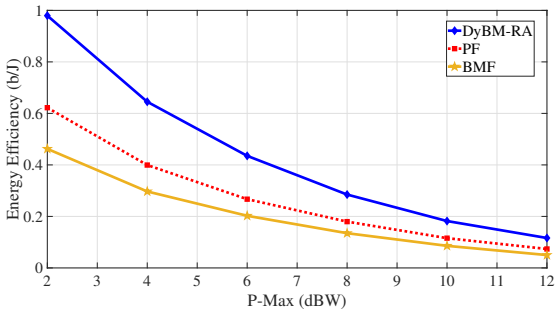

Figure 5.9: Evaluation of the energy efficiency performance with respect to P-Max for the different algorithms.

plexity and longer algorithm runtime. Similarly, DyBM-RA outperforms PF and BMF due to its resource allocation strategy, which allocates a higher bandwidth ratio of W_i^c to UEs under CS CQI compared to those under RFD CQI. DyBM-RA also meets SLA requirements for different traffic classes, including URLLC, due to its restrictive user-to-satellite association policy.

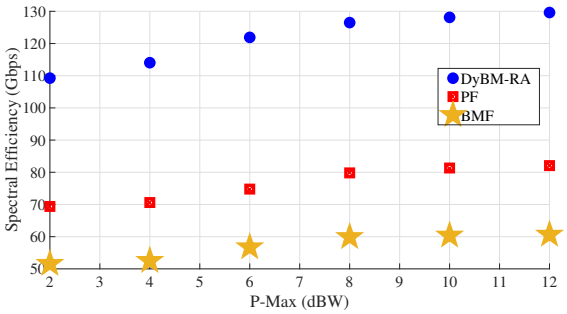

Figure 5.10: Evaluation of the spectral efficiency performance with respect to P-Max for the different algorithms.

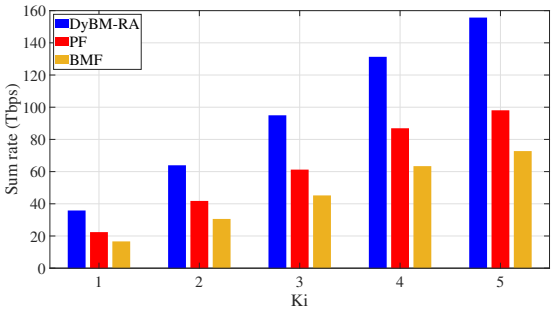

Figure 5.11: Evaluation of MC from K_i in the different algorithms.

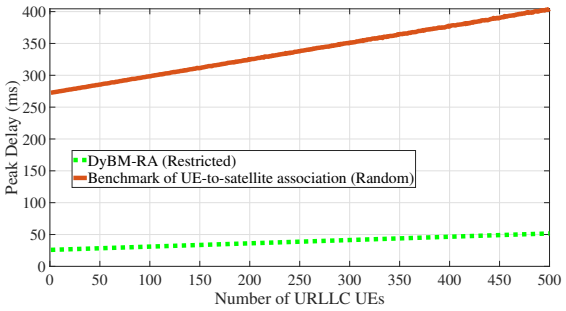

Figure 5.12: Evaluation of the UE-to-satellite association on URLLC peak delay.

5.7 Conclusions

In this Chapter, the offered capacity of a NTN is optimized by employing various strategies, including MC, which combines the capacity of LEO, MEO, and GEO CCs. A resource allocation architecture is designed for a multi-tier NTN that involves a HGS responsible for managing the orbital satellites. This architecture operates with two waveforms—DVB-S2X and 5G NR, that are beamed to UEs to provide capacity. To achieve this, a non-convex combinatorial optimization problem with inequality constraints is formulated. The problem is solved by decoupling it into two subproblems: dynamic beam allocation and joint

power and bandwidth allocation. The dynamic beam allocation subproblem is solved using an iterative algorithm, while the joint power and bandwidth allocation subproblem is addressed using a MADRL aided resource allocation algorithm. The objective is to maximize the offered capacity over a stochastic channel. The proposed dynamic beam and resource allocation (DyBM-RA) algorithm utilizes UE traffic class (that includes URLLC, HDTV and eMBB), and CQI categories, such as CS or RFD, to develop an intelligent resource allocation framework that maximizes the offered capacity. The DyBM-RA algorithm outperforms other state-of-the-art algorithms in terms of sum rate, SE, EE, and URLLC peak delay. It surpasses the PF and BMF algorithms in terms of sum rate/capacity by 44.94% and 72.56%, respectively. Future research will focus on integrating unmanned aerial vehicle (UAV) base stations into multi-tier NTNs.

Chapter 6

Deep Learning-based Network Slicing and Admission Control in Multi-Orbital NTN

Recently, there has been a surge in the adoption of multi-orbital satellite networks for integrated service delivery. Operators are increasingly collaborating and constructing multi-layer network infrastructures to meet growing traffic demands. This chapter introduces a novel service delivery model where infrastructure providers (InPs) lease out resources from non-terrestrial networks (NTNs) as slices to mobile virtual service operators (MVSOs). These MVSOs then offer the leased resources to subscribers, facilitating efficient utilization of NTN resources in the telecommunications ecosystem. The model utilizes an innovative NTN slicing architecture that incorporates multi-layer satellites, including low Earth orbit (LEO), medium Earth orbit (MEO), and geostationary orbit (GEO) constellations. It features a hybrid gateway station (HGS) tailored to the virtualization architecture specified by the 3rd Generation Partnership Project (3GPP). In this setting, we formulate a multi-objective optimization problem (MOOP) comprising two combinatorial objective functions for InPs and MVSOs, aiming to maximize revenue. The proposed algorithm addresses the joint network slicing and admission control (AC) requirements by employing techniques such as non-dominated sorting genetic algorithm II (NSGA-II), multi-objective reinforcement learning (MORL), and a heuristic approach. Our algorithm outperforms the Round Robin (RR) and Max-Min fairness approaches, achieving increases in peak revenue of 3.91% and 18.73%, respectively.

6.1 Introduction

The emergence of digital innovations and new technologies, such as the Internet of Things (IoT), machine-type communications, and Industry 4.0 solutions, has significantly transformed the demands for connectivity in today's world [129]. As a result, there is a growing need for reliable and widespread global connectivity. Satellite communication systems offer a promising solution to address these requirements, as they can provide coverage in remote areas, enable seamless connectivity across vast distances, and support a wide range of applications [130]. With their ability to overcome geographical limitations and reach under-served regions, satellite communication systems have the potential to meet the evolving connectivity needs of various industries and sectors. In this context, the specifications outlined by the 3rd Generation Partnership Project (3GPP) regarding satellite connectivity have created an intriguing prospect for terrestrial communication service providers and satellite operators to collaborate symbiotically and establish a global non-terrestrial network (NTN) ecosystem [49]. Specifically, 3GPP has made efforts to adapt the fifth-generation (5G) New Radio (NR) as well as narrow-band IoT (NB-IoT) and long-term evolution (LTE) for machine-type communications (LTE-M) to provide satellite-based connectivity [131]. This NTN ecosystem is expected to bring significant benefits to individuals and organizations by providing global connectivity opportunities [132].

The emerging use cases in wireless connectivity necessitate a departure from the conventional one-size-fits-all approach, as the diversity of service characteristics among these new use cases continues to expand. For instance, Industry 4.0 seeks flexible and highly customizable solutions, creating a demand for rapid deployment, configuration, modification, and cost-effective wide-area coverage. In the past, private networks were employed to address specific communication requirements of user groups, but these networks often had limited options for connection quality, functionality, and customization. To overcome these issues, 5G technology introduces network slicing as an effective solution. Network slicing enables the partitioning of wireless networks into virtual network elements or *slices* that can be configured to suit the unique needs of applications, services, devices, customers, or operators. Each network slice operates as a form of private network, running on a shared physical infrastructure while maintaining specified quality of service (QoS) requirements. This approach combines the benefits of private networks with the efficiency and scalability of a public network.

Additionally, data traffic in non-terrestrial networks (NTNs) is diverse and randomly distributed in the serving areas, and coming from various users with different QoS requirements [57]. Thus, employing network slicing in NTNs would also help satisfying the asymmetry and heterogeneity of the traffic demands. Specifically, NTN slicing allows for the efficient allocation of resources and tailored services to different user segments. For instance, it enables the separation of traffic between critical applications like emergency services and the less time-sensitive data transfers, optimizing system capacity utilization and ensuring uninterrupted connectivity in critical situations. NTN slicing also enhances security by isolating different user groups, minimizing the risk of data breaches or interference. Further, NTN slicing can foster innovation by enabling experimentation with new services and applications within isolated slices, without affecting the entire network.

Table 6.1: Comparison of Related Literature on Network Slicing and Admission Control

Main Topics	[133]	[134]	[135]	[136]	[137]	[138]	[139]	[140]	[141]	[142]	[143]	[144]	[145]	This work
Terrestrial Network slicing	✓	✓	✓	✓	✓	✓	✓	✓	✓	✓	✓	✓		
NTN Network slicing												✓	✓	✓
Multi-layer NTN Network slicing														✓
Block-chain based secure slicing						✓	✓							
Admission control with priority		✓			✓			✓	✓	✓	✓			✓
Congestion control		✓						✓						
Problem formed as MOOP						✓	✓							✓
Problem formed as non-MOOP	✓		✓	✓	✓			✓	✓	✓	✓	✓	✓	
Optimization with genetic algorithm		✓		✓									✓	✓
Optimization with machine learning	✓	✓	✓		✓	✓	✓	✓	✓	✓	✓	✓		✓
Synthetic dataset									✓					
Real dataset										✓	✓			✓
Traffic prediction/forecasting	✓			✓					✓	✓				✓
Optimization with Heuristic	✓			✓										✓
Revenue maximization objective	✓		✓	✓	✓	✓	✓	✓	✓	✓	✓		✓	✓
QoS satisfaction objective		✓	✓			✓	✓					✓	✓	✓
Efficient resource utilization	✓	✓				✓		✓		✓				✓
SLA violation minimization	✓	✓							✓					✓

6.1.1 Related Works

In the literature, several contributions have studied network slicing for terrestrial communications, including 5G, and some have integrated machine learning techniques to augment and streamline resource management processes. In [133], terrestrial 5G slicing is presented with a forecasting scheme per slice, employing an admission control decision process that considers traffic and spatial information to meet the required service level agreements (SLAs). Additionally, reinforcement learning (RL) has been integrated into the system to enhance overall performance. Q-learning, a form of RL, is applied in the 5G network slicing framework in [134], which was analyzed with admission and congestion control mechanisms.

Similarly, a Q-learning aided algorithm has been developed in [135] to maximize revenue

for the infrastructure providers (InPs) while ensuring QoS as required by the mobile virtual service operators (MVSOs), who lease network capacity in the form of slices from the InPs. This model is known as Infrastructure-as-a-Service (IaaS). The authors in [136] explored slice overbooking to maximize the terrestrial operator's revenue in an end-to-end orchestrated slicing framework. A radio access network (RAN) domain slicing for 5G is studied in [137], where a slice admission strategy based on RL is presented. The service demands have different priorities, upon which the InPs make decisions on slice requests to accept or reject in order to maximize revenue. Similarly, authors in [138] and [139] present blockchain-based resource trading between InPs and mobile virtual network operators, aided with RL for 5G RAN slice resource allocation.

In addition, a RL algorithm is presented in [140], which defines a policy that jointly optimizes admission and congestion control to maximize system reward while handling prioritized slices. A type of deep learning (DL) prediction algorithm, known as long short-term memory (LSTM), is studied in [141] and [142] to predict traffic demand requirements for efficient resource allocation in 5G network slicing, in order to avoid revenue loss due to forecasting errors. A joint network slicing and admission control (AC) problem has been formulated and solved using multi-agent deep RL in [143] for revenue maximization, considering three classes of slice requests: enhanced Mobile Broadband (eMBB), massive Machine-Type Communication (mMTC) and Ultra-Reliable Low-Latency Communications (URLLC) with real dataset.

Further, in satellite communications, research on network slicing has mainly focused on single-layer low Earth orbit (LEO) constellations [144] [145], overlooking the significant potential of incorporating multi-layered NTN architectures, which could harness the added resilience and reliability inherent in multi-orbit satellite systems [75]. This slicing paradigm has the potential for dynamic QoS offerings and to satisfy diverse capacity demands. In addition, integrating multi connectivity (MC) into the network slicing framework offers several advantages for the multi-layer NTNs. Specifically, it enables seamless load balancing among satellite layers, optimizing resource use and ensuring consistent service quality across orbits. MC also enhances network redundancy, reducing the impact of disruptions and improving reliability [4].

These observations have motivated this work to combine multi-layer NTN slicing with MC to further enhance the system capacity and communications reliability. Interestingly, multi-

layer NTN has attracted industry interest as many operators are investing in expanding their network portfolios with additional orbital constellations or merging with other operators that offer different orbital satellite capacities, for instance SES operates medium Earth orbit/geostationary orbit (MEO/GEO) constellations [146], and the merger of Eutelsat with Oneweb occurred for LEO/GEO service offerings [147]. However, the amalgamation of NTN slicing and MC brings about multiple challenges due to the inherent complexity and the dynamic nature of the NTN entities in order to realize the benefits fully. This intricate scenario underscores the significance of incorporating machine learning as a valuable tool within this framework, given its capacity to handle complex and non-linear time-series features within the data, especially for prediction.

In this complex setup, multi-objective optimization is essential to consider multiple, often conflicting, objectives simultaneously when making decisions. In our scenario, it is insufficient to optimize for just one objective because there are multiple objectives that need to be balanced or traded off against each other. In this context, multi-objective optimization problems (MOOPs) provide a framework for systematically exploring the trade-offs between these objectives and finding optimal solutions that balance them effectively. For example, the authors in [148] explored a form of genetic algorithms (GA) known as non-dominated sorting genetic algorithm II (NSGA-II) to solve a two-objective multi-objective optimization problem (MOOP) involving the maximization of profit and the minimization of satellite maneuver angle in GEO satellites. Further, RL-aided approach was considered in [149] to solve MOOP involving three objectives for dynamic beam hopping in satellites, using an algorithm labeled as multi-objective reinforcement learning (MORL).

6.1.2 Contributions

To this end, we formulate a MOOP and propose a novel algorithm that utilizes GA and MORL, along with deep learning predictions implemented with realistic dataset inputs, to enhance AC decisions while adapting to traffic fluctuations, to minimize service level agreement (SLA) violations and maximize revenue within the network.

Contributions: Our key technical contributions can be explicitly summarized as follows:

1. Design a novel network slicing architecture for a multi-layer NTN topology comprising of GEO/MEO/LEO satellites and hybrid gateway station (HGS) [150]. This architecture

is adapted to the 3GPP specification with network orchestration management flow, incorporating machine learning applications and resource scheduling integration.

2. Provide a practical business model framework for functional service operations, which entails mobile virtual service operator (MVSO) leasing satellite infrastructural network resources involving a multi-layer NTN. This model aims to offer services to end-users based on agreed SLAs.

3. Develop a joint network slicing and AC algorithm that considers dynamic traffic demand involving eMBB and URLLC, along with the available network resources with QoS and SLA requirements. The algorithm is designed from a MOOP to maximize the revenue of the infrastructure provider (InP) and the MVSO over some constraints. This problem is solved using three approaches: the first involves optimal vectors obtained from a Pareto curve using NSGA-II, the second utilizes MORL, and the last employs a Heuristic approach.

4. Introduce a novel AC mechanism known as revenue maximization (Rev-Max) algorithm, which is aided by recurrent neural networks (RNNs) using LSTM algorithm, for predicting the dynamic traffic demands of the two classes, eMBB and URLLC, which have diverse radio frequency features. The AC mechanism considers the available capacities of divergent LEO, MEO and GEO satellites, including the different slice weight of the demanded traffic classes and the priority configured for each class. It then admits the slices cognitively while ensuring that QoS requirements are satisfied.

The rest of the Chapter is structured as follows. In Chapter 6.2, the network model and architecture are discussed in detail. Chapter 6.3 focuses on the multi-objective optimization problem. while the optimization solution and the proposed algorithms are outlined in Chapter 6.4. In Chapter 6.5, the simulation setup and performance evaluation are discussed. Finally, the conclusion is summarised in Chapter 6.6.

6.2 Network Model and Architecture

6.2.1 Service Flow Model

The service and business flow model is depicted in Fig. 6.1, which involves three actors (i) the end user (subscribers), (ii) MVSOs, and (iii) InPs. The InP owns the network infras-

tructure over which services are offered by the MVSOs. This infrastructure involves satellite RAN connected to the core network (CN). Both hardware and virtualized/softwarized components of the network are leased as network resource offerings to multiple MVSOs for a fee. Details are discussed in Chapter 6.2.2. The MVSOs offer services such as broadband connectivity to cruise ships, trains, and airplanes, as well as multicast/broadcast content to homes. Additionally, some telecom operators requiring satellite backhauling services can also be categorized as MVSOs. The MVSOs provide subscribers with different QoS options based on their needs and budget, enabling access to a variety of broadband services accompanied by SLAs.

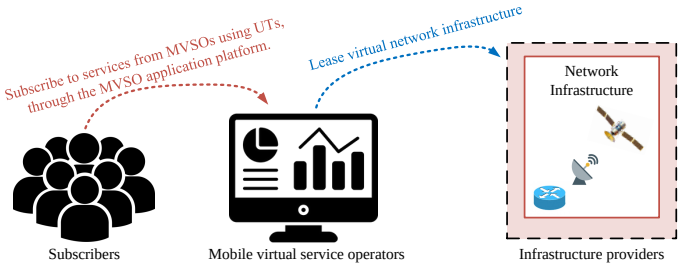

Figure 6.1: Service and business flow model involving subscribers, virtual operators and infrastructure providers.

6.2.2 Network Topology and Architectural Framework

Multi-domain Network

The network topology consists of RAN connected to a CN domain through the HGS. The RAN domain comprises the three orbital layers: LEO, MEO and GEO satellite constellations. These constellations are linked to a pool of interconnected hybrid gateway stations, and a common network operation center (NOC) for management and control, resulting in a multi-layer NTN RAN.

Network Slicing

Parts of the multi-layer NTN RAN have been adapted into the 3GPP network function virtualization (NFV) reference architecture [151], where network virtualization and softwarization are implemented for effective resource slicing and orchestration, as shown in Fig 6.2. Network slicing enables the dimensioning of network resources to cater to different individuals, organisations or third-party service suppliers/operators simultaneously. This technology has

become an essential part of 5G standardization, presenting a business case where InPs can maximally utilize their resources for optimum revenue generation. The network topology shows transmission sessions for multiple users with different traffic classes of URLLC and eMBB, denoted as ω_1 and ω_2, respectively. These users subscribe to the various services offered by MVSOs. To meet the dynamic lease demands of different MVSOs, the InP must dimension the virtual components of the physical network into portions known as network slices. These lease demands arise as slice requests (SRs) from different MVSOs. Each SR is accompanied by the desired QoS specifications and RAN/CN capacity requirements. Further, it is important to note that ensuring reliability and real-time performance in network slicing involves isolating slices to prevent interference, dynamically allocating resources, and managing slice life-cycles through orchestration. Implementing QoS policies and NFV enhances performance and scalability. The enforcement of SLAs, and incorporating redundancy also ensures reliability, while automation reduces errors and improves response times. The solution proposed in this chapter is designed to ensure reliability and real-time performance.

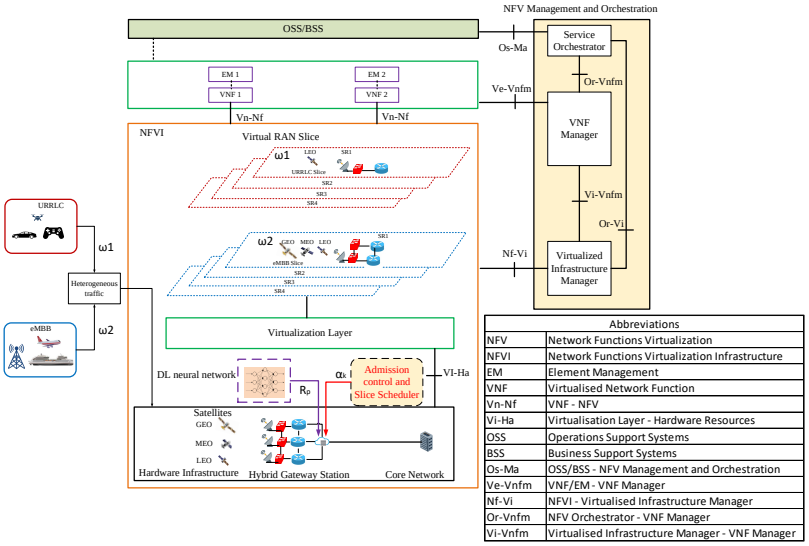

Abbreviations	
NFV	Network Functions Virtualization
NFVI	Network Functions Virtualization Infrastructure
EM	Element Management
VNF	Virtualised Network Function
Vn-Nf	VNF - NFV
Vi-Ha	Virtualisation Layer - Hardware Resources
OSS	Operations Support Systems
BSS	Business Support Systems
Os-Ma	OSS/BSS - NFV Management and Orchestration
Ve-Vnfm	VNF/EM - VNF Manager
Nf-Vi	NFVI - Virtualised Infrastructure Manager
Or-Vnfm	NFV Orchestrator - VNF Manager
Vi-Vnfm	Virtualised Infrastructure Manager - VNF Manager

Figure 6.2: Schematic diagram of the considered DL-aided network slicing architecture over the topology of the Multi-layer NTN.

Admission Control

The AC for the SR is executed in the HGS. The indicator of the accepted SR, α_k, is sent to the HGS controller so that SR k can be admitted into the RAN. This mechanism evaluates the total lease capacity from the InP, to ensure adequate accommodation of MVSO slice

demand based on the slice request (S_w[1]), and the corresponding constraints on the MVSO SLAs (additional details in Chapter 6.3). This is performed to establish an acceptance policy for all SR, based on the defined objective of the problem. In the current setup, revenue maximization is considered as an objective, with details provided in Chapters 6.3 and 6.4. Subsequently, appropriate RAN resources are allocated to ensure that the SLA is not violated, based on the dynamic traffic insights obtained using a deep learning model of RNN, details of which are deferred to Chapter 6.4.3.

6.2.3 Downlink Transmission Model

The transmission involves datacenter/CN to end users through the RAN domain. This chapter focuses on transmission in the RAN domain from the HGS over the multi-layer NTN and satellite channel, to the end users.

Link Budget Model

The transmission link is established based on link budget considerations to achieve reliable transmission over the channel. For a satellite link, the overall propagation loss (L_{Total}) in dB between the satellite and the user terminal (UT) is:

$$L_{Total} = L_{FSL} + L_{atm} + L_{\varsigma} + L_{sc} \tag{6.1}$$

where L_{atm} is the atmospheric loss as provided in ITU-R P.676 [83], and L_{sc} is the loss from tropospheric scintillation, which affects Ka band signals, with values obtained as described in ITU-R P.618 [84]. L_{ς} stands for the random lognormal variable with a variance based on the shadowing environment and zero mean, i.e, $L_{\varsigma} \sim (0, \varsigma^2)$, with 3GPP providing the values of ς^2; this term is influenced by the elevation angle for different cases of rural, dense urban, and urban environments [85]. The free space loss is represented as L_{FSL} in (6.2), which is a function of the propagation distance between the satellite and the UT.

$$L_{FSL} = 32.45 + 20\log_{10} F_r + 20\log_{10} d_p \tag{6.2}$$

where d_p (in meters) is the propagation distance, and F_r (in GHz) is the carrier frequency. Assuming a downlink satellite communications network where UTs are scattered over different

[1] A S_w is the unit of slice request per individual MVSO request, out of the total SR in that traffic category.

satellite beams, there exist intended user UT_n randomly positioned within the coverage area of the intended satellite S_s, while satellite S_a transmitting to user UT_a interferes with UT_n. The intended receive power by UT_n from satellite S_s is

$$C_{s,n} = EIRP_s + G_n - L_{Total} \tag{6.3}$$

where G_n is the gain of the receiving UT_n, and $EIRP_s$ is the downlink equivalent isotropically radiated power from the intended satellite S_s towards intended UT_n. The noise power observed at the receiver is computed as:

$$\begin{aligned} N = N_{fig} + 10\log_{10}\left(T_0 + (T_{ant} - T_0)10^{-0.1N_{fig}}\right) \\ + K_B + 10\log_{10}(B) \end{aligned} \tag{6.4}$$

where N_{fig} is the noise figure at the receiver, T_0 is the reference noise temperature (290 K), T_{ant} is the temperature of the receiving antenna, K_B is the Boltzmann's constant in dBW/K/Hz, and B is the bandwidth in Hz. Further, the corresponding downlink carrier to noise ratio can be obtained in dB by subtracting (6.4) from (6.3), as shown in (6.5):

$$\left(\frac{C}{N}\right)_{s,n} = EIRP_s + G_n - L_{Total} - N \tag{6.5}$$

The total interference captured at the intended receiving UT_n in the downlink is derived as I_n in dB, as shown below:

$$I_n = 10\log_{10}\left(\sum_{ch=1}^{N_{ch}} 10^{0.1I_{a,n}}\right) \tag{6.6}$$

where $I_{a,n}$ is the interference from the a-th interfering satellite/beam, and $ch = 1, ..., N_{ch}$, with N_{ch} being the number of co-channel beams.

$$I_{a,n} = EIRP_a + G_n - L_{Total} \tag{6.7}$$

The carrier to interference ratio in dB is obtain by subtracting (6.6) from (6.3)

$$C/I_{s,n} = EIRP_s + G_n - L_{Total} - I_n \tag{6.8}$$

Hence, the carrier to interference with noise ratio (C/IN) in dB is given below from [85]:

$$\gamma_{s,n} = \frac{C}{IN_{s,n}} = -10\log_{10}\left(10^{-0.1\frac{C}{N_{s,n}}} + 10^{-0.1\frac{C}{I_{s,n}}}\right) \tag{6.9}$$

Achievable Rate

The achievable rate on the forward transmission link from satellite S_s to receiver UT_n, utilizing bandwidth B summed over number of intra/inter orbital satellite component carriers C is given as:

$$R_n = \sum_{c=1}^{C} B\log_2(1+\gamma_{s,n}) \tag{6.10}$$

The sum rate for each provision slice k is derived below:

$$R_k = \sum_{n=1}^{N_k^u} R_n \tag{6.11}$$

where N_k^u is the total number of users in slice k.

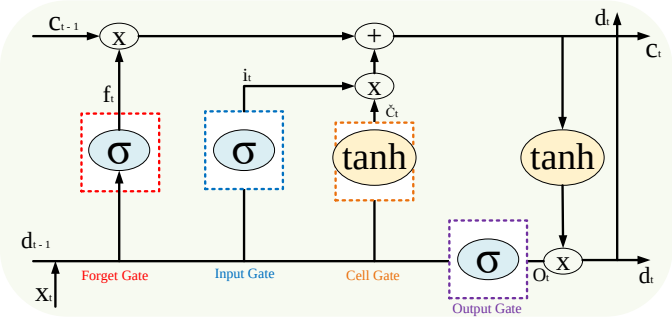

Figure 6.3: LSTM cell architecture.

6.2.4 Deep Learning Traffic Prediction Model

In this chapter, a RNN-based deep learning model is adopted since it can solve time-series learning problems. To tackle the vanishing gradient challenge in RNN, LSTM neural network was proposed in [152] with memory cell, and additional improvement was introduced with the addition of gates in [153]. The LSTM cell architecture is presented in Fig 6.3 [154], where the forget gate (f_t), input gate (i_t), cell gate ($\bar{C}_t$), and the output gate (O_t) are shown. Through these gate functions, LSTM can capture difficult features in time-series for either short or long terms [155]. To handle temporal dependencies, LSTM defines and maintains the cell state

to regulate information flow over time, a vital mechanism of the LSTM structure [156]. To effectively address long-term and short-term dependencies in time-series data from satellite communications applications, the LSTM architecture is a suitable prediction solution. [157].

The LSTM architecture performs the following actions discussed further. Firstly, the LSTM categorize the input data as important and redundant, crucial to eliminating redundant information irrelevant for data prediction. The forget gate decides which information should be discarded or retained by the LSTM, and this is shown below from [158].

$$f_t = \sigma(W_{f,t}x_t + W^{'}_{f,t}d_{t-1} + b_{f,t}) \tag{6.12}$$

where sigmoid function is denoted as σ, and the forget weight in time t are $W_{f,t} \in \mathbb{R}^{Z\times Y_{in}}$ and $W^{'}_{f,t} \in \mathbb{R}^{Z\times Z}$, while the biases at time t are represented as $b_{f,t} \in \mathbb{R}^{Z\times 1}$. Further, $x_t \in \mathbb{R}^{Y_{in}\times 1}$ denotes the input vector of size Y_{in} and d_{t-1} is the previous hidden state of size Z. The second step is for the LSTM cell to apply computations on the information through the input gate to store the relevant information as:

$$\begin{aligned} i_t &= \sigma(W_{i,t}x_t + W^{'}_{i,t}d_{t-1} + b_{i,t}) \\ \bar{c}_t &= \tanh(W_{\bar{c},t}x_t + W^{'}_{\bar{c},t}d_{t-1} + b_{\bar{c},t}) \end{aligned} \tag{6.13}$$

The third step involves LSTM updating the current cell state c_t with the previously mentioned two steps above.

$$c_t = f_t \odot c_{t-1} + i_t \odot \bar{c}_t \tag{6.14}$$

where $\odot$ is the Hadamard product.

The fourth and final step is to generate the LSTM cell output. This is achieved by updating the hidden state and generating the output using the output gate, as shown in the computation below:

$$\begin{aligned} o_t &= \sigma(W_{o,t}x_t + W^{'}_{o,t}d_{t-1} + b_{o,t}) \\ d_t &= o_t \odot \tanh c_t \end{aligned} \tag{6.15}$$

The metric evaluating the effectiveness of the model is the mean absolute error (MAE) [159] given by:

$$MAE = \frac{1}{T}\sum_{t=1}^{T} R_a - \widehat{R_p} \tag{6.16}$$

where T is the duration of prediction, R_a and $\widehat{R_p}$ are the actual and predicted traffic, respectively.

6.2.5 Datasets

The dataset comprises averaged real measured satellite traffic data from the operator SES networks, which has been preprocessed into two traffic classes with different QoS specifications, denoted as ω_1 and ω_2 for URLLC and eMBB, respectively. The data represents hourly traffic demand for a period of 22 days. For URLLC, the service specifications include latency ranging from 10 ms to 50 ms, throughput from 20 Mbps to 100 Mbps, and availability of 99% [160]. The corresponding use-cases for delay-intolerant communications include factory automation, airborne base stations for non-public network (NPN), autonomous driving, autonomous ship, and medical imaging/video traffic [161]. On the other hand, eMBB service specifications require 150 ms to 300 ms latency, 35 Mbps to 1,200 Mbps throughput, and 99% availability [52] [162] [163], catering to use-cases such as 5G backhauling and multimedia content delivery. Hence, the dataset aligns with the outlined specifications, such that ω_1 and ω_2 operate with a single-user maximum guaranteed bit rate (GBR) of 47 Mbps and 115 Mbps, respectively.

6.3 The Optimization Problem

This problem involves both slicing and AC, aiming to maximize operator revenue while ensuring efficient resource utilization and maintaining QoS requirements. Two functions are considered to create a multi-objective function.

6.3.1 Infrastructure Objective Function

The objective of this problem is to maximize revenue for the InP while ensuring that QoS requirements are satisfied and SLAs are not violated for the MVSOs.

$$F_i = \sum_{k=1}^{K} \sum_{s=1}^{S} \alpha_k \vartheta_k^s R_k^s \beta_{k,s} - \zeta \vartheta_k^s R_k^s \tag{6.17}$$

where α_k is the indicator variable for the acceptance of the k-th slice, ϑ_k^s is the offered price by the InP in terms of data rate as \$/Mbps unit, R_k^s is the cumulative data rate of slice k in satellite s in Mbps unit, $\beta_{k,s}$ indicates a binary resource association indicator where k-th

slice is allocated to satellite bandwidth resource on satellite s. The overhead cost incurred by the InP for leasing capacity for slice k, associated with satellite s, is represented as $\zeta\vartheta_k^s R_k^s$, where ζ is the InP overhead cost constant that satisfies $0 \leq \zeta \leq 1$.

The InP optimization problem is formulated as follows:

$$\underset{\vartheta_k^s, \beta_{k,s}}{\text{maximize}} \ F_i \tag{6.18}$$

subject to $C_1 - C_6$

The first constraint C_1 indicates the acceptance and admission of network SR k as α_k. Priority consciousness is configured where each SR is either of higher priority (H-P) or lower priority (L-P). SR priority is proportional to the maximum GBR of the slice, captured in the SR traffic class as ω. This provides identification for the types of resources that are accepted and rejected.

$$C_1 : \alpha_k = \begin{cases} 1, & \text{if slice is accepted;} \\ 0, & \text{otherwise.} \end{cases} \tag{6.19}$$

Constraint C_2 ensures that the required RAN capacity in terms of total bandwidth B_k^s in MHz for all accepted slices α_k, is not more than the available satellite bandwidth $\overline{B}_s$ in MHz of all satellites S. As a result, the bandwidth resources are not over-dimensioned per SR, allowing for the acceptance of additional SR into the network.

$$\mathbb{C}_2 : \sum_{k=1}^{K} \alpha_k B_k^s \leq \sum_{s=1}^{S} \overline{B}_s \tag{6.20}$$

Constraint C_3 ensures that the data rate R_k of slice k lies between a maximum (R_ω^{max}) and minimum (R_ω^{min}) limit, based on the traffic class ω of either URLLC or eMBB as agreed upon in the SLA.

$$\mathbb{C}_3 : \alpha_k R_\omega^{min} \leq \beta_{k,s}.R_k^s \leq \alpha_k R_\omega^{max} \quad \forall k \in K \quad \forall s \in S \tag{6.21}$$

The constraint on the end-to-end (E2E) delay limit requirement for slice k on satellite s is given in C_4. It also ensures that E2E delay D_k in ms, as per SLA, is guaranteed.

$$\mathbb{C}_4 : D_k \beta_{k,s} \leq D_k^{max} \ \forall k \in K \quad \forall s \in S \tag{6.22}$$

In this problem, the different slices $\forall k \in K$ have different traffic categories with varying QoS requirements, involving throughput and delay.

$$\mathbb{C}_5 : \sum_{s=1}^{S} \beta_{k,s} \leq \Omega \quad \forall k \in K \tag{6.23}$$

Constraints C_5 restricts the accepted slice α_k to utilize bandwidth resources from a maximum of Ω number of inter/intra orbital satellites, facilitating MC for user terminals. This allows the slice k to associate with only a limited number of satellites in RAN, preventing congestion or association rejection for other slice request.

$$C_6 : D_k^{max} = \begin{cases} \max\{D_k^{LEO}\} + T_{sig} \text{ if } \omega = URLLC \\ \max\{D_k^{GEO}, D_k^{MEO}, D_k^{LEO}\} + T_{sig} \\ \text{if } \omega = eMBB \\ 0 \ otherwise \end{cases} \tag{6.24}$$

Constraint C_6 further defines the actual maximum delay mapping for the traffic classes URLLC or eMBB, with respect to orbital satellite required to serve the traffic class in question. Here, $D_k^s(ms) = [\frac{d_k^s}{c}]$ [164], where d_k^s (in m) is the propagation distance through satellite s (LEO, MEO or GEO), and c is the speed of light in m/ms. Additionally, T_{sig} is the signal processing time in ms.

This is a non-convex combinatorial optimization problem with inequality constraints, which maximizes the variables ϑ_k^s and $\beta_{k,s}$.

6.3.2 MVSO Objective Function

The objective of this problem is to maximize MVSO revenue by enhancing the subscriber satisfaction index (ϱ_n) for all users N, which will motivate enhanced service patronage. The subscriber satisfaction index is a performance indicator determined by the user data rate, delay, number of users and unit price; it increases when rate increases and the delay reduces, among other factors. The function in (6.25) captures the net revenue of the MVSO, where the cost of leasing the infrastructure is deducted as $\vartheta_k^s R_{n,k}^u$, and gain from satisfaction index is presented as ϱ_n^2.

$$\overline{F}_m \ = \sum_{n=1}^{N} \sum_{k=1}^{K} \left((\varrho_n^2 + \vartheta_n^u R_{n,k}^u) - \vartheta_k^s R_{n,k}^u \right) \tag{6.25}$$

where $R_{n,k}^u$ is the achievable rate of subscriber n in Mbps mapped to slice k, ϑ_n^u is the unit price offered by MVSO to subscribers in \$/Mbps. We assume each MVSO represents a slice k, and multiple users N are admitted into slice K.

The objective function is to maximize variables ϱ_n and ϑ_n^u, while considering constraints. This is a mixed integer nonlinear programming (MINLP) optimization sub-problem.

$$\underset{\varrho_n, \vartheta_n^u}{\text{maximize}} \ \overline{F}_m \tag{6.26}$$

subject to $C_7 - C_{11}$

The first constraint C_7 ensures that the bandwidth B_n^u in MHz allocated to UT n does not exceed the total available leased bandwidth B_k^s in MHz for slice K.

$$\mathbb{C}_7 : \sum_{n=1}^{N} B_n^u \leq \sum_{k=1}^{K} \alpha_k B_k^s \ \ \forall n \in N \tag{6.27}$$

Constraint C_8 ensures that the user GBR R_n^u for all users N by the MVSO is less than or equal to the GBR of the slice R_k^s offered by the InP in the SLA. The eMBB users may use MC to achieve the GBR.

$$\mathbb{C}_8 : \sum_{n=1}^{N} R_{n,k}^u \leq \sum_{k=1}^{K} \alpha_k R_k^s \ \ \forall k \in K \tag{6.28}$$

Constraint C_9, inspired from [165], ensures ϱ_n increases as $R_{n,k}^u$ increases, and reduces when N_k^u or ϑ_n^u or the delay of the user $D_{n,k}^u$ increases. This constraint is vital as it captures the subscriber's quality of experience (QoE), which depends on the variables mentioned above, impacting the MVSO revenue, especially in the long term.

$$\mathbb{C}_9 : \varrho_n = \frac{R_{n,k}^u}{(N_k^u + \vartheta_n^u + D_{n,k}^u)} \ \forall n \in N \tag{6.29}$$

To enable the MVSO to profit from the leased bandwidth capacity of the InP, constraint C_{10} ensures that the unit price ϑ_n^u set by the MVSO to the user is greater than the unit price

ϑ_k^s set by the InP to the MVSO.

$$\mathbb{C}_{10} : \vartheta_k^s < \vartheta_n^u \tag{6.30}$$

Constraint C_{11} ensures that the delay for user n matches the delay of the slice k it is mapped to.

$$\mathbb{C}_{11} : D_{n,k}^u = D_k \quad \forall n \in N \quad \forall k \in K \tag{6.31}$$

All the constraints in this Chapter are equality and inequality constraints.

6.3.3 Multi-objective Problem Formation

The two objectives in (6.20) and (6.18) are combined to form the MOOP in (6.26), which is solved in Chapter 6.4.

$$\max_{\vartheta_k^s, \beta_{k,s}, \varrho_n, \vartheta_n^u} (F_i, \overline{F}_m) \tag{6.32}$$

subject to $C_1 - C_{11}$.

The variables common to F_i and $\overline{F}_m$ are R_k^s, B_k^s, α_k, D_k and ϑ_k^s. The variables unique to F_i are $\beta_{k,s}$ and $\overline{B}_s$, while those unique to $\overline{F}_m$ are ϱ_n, ϑ_n^u, B_n^u, $R_{n,k}^u$ and $D_{n,k}^u$.

6.4 Proposed Solution Strategy for MOOP

The revenue maximization with efficient resource utilization by network slicing for the two objective functions $\overline{F}_m$ and F_i is a MOOP along with the equality and inequality constraints C_1 to C_{11}. Each objective problem function involves maximizing operations with respect to their respective variables $\vartheta_k^s, \beta_{k,s}, \varrho_n$ and ϑ_n^u. These are also combinatorial problems, as $\overline{F}_m$ evaluates to determine combinations of variables, including the slice and satellite allocation (K and S), while F_i similarly searches for combinations of the user and satellite association (N and K) variables.

Solving the MOOP in (6.32) poses a significant challenge. Therefore, the solution strategy is subdivided into three parts: pricing mechanism, AC, and traffic prediction. Each of these components is addressed using different techniques and algorithms to arrive at a comprehensive solution.

6.4.1 Pricing Mechanism Solution

The pricing optimization within the MOOP is addressed through a comprehensive strategy involving three distinct approaches, each outlined below. These approaches include the utilization of advanced algorithms such as non-dominated sorting genetic algorithm, multi-objective reinforcement learning approach, and a developed heuristic approach discussed in Chapter 6.5.2. Each of these methods brings unique advantages to the optimization process, contributing to a robust solution framework.

Non-dominated Sorting Genetic Algorithm II

The pricing aspect of the MOOP problem for joint NTN slicing and AC can be solved using the NSGA-II algorithm. The objective of solving (6.32) is to maximise ϑ_k^s, $\beta_{k,s}$, ϱ_n and ϑ_n^u. The NSGA-II algorithm is considered due to its comparatively lower complexity, faster convergence, scalability, and ability to provide solutions that are very close to optimal, as compared to other solvers or algorithms for MOOPs [166]. The following will discuss the methodology of NSGA-II algorithm from [167] [168] [169]; firstly technical parameters will be explained for better understanding.

An individual or genome is any point to which a fitness function can be applied. A fitness function is a measure intended to be optimized. An array of individuals is considered a population or generation, and the average distance between individuals that make up a population is known as diversity, an important factor in the algorithm as it allows for search over a certain area. A fitness value is the value of the fitness function for a particular individual. The algorithm creates the next generation by selecting special individuals with the best fitness values in the current population, known as parents, which are used to create the next generation of individuals referred to as children. An individual point r can dominate another point v when the following conditions are satisfied in a vector-valued function f.

$$f_i(r) \leq f_i(v) \;\forall\; i \;; \quad f_j(r) < f_j(v) \text{ for some } \; j \tag{6.33}$$

A non-dominated set of points consist of points that do not have any other point dominating them. The algorithm uses *rank* to select the parents, with the rank of an individual indicating its level of dominance. Individuals with rank 1 are not dominated by any other individuals, while rank 2 individuals are dominated only by those in rank 1. Further, crowd-

ing distance (Dis) is a technique used to evaluate the distance between an individual and its closest neighbour. The NSGA-II algorithm evaluates this distance in a decision variable space x for individuals of similar rank. This distance is measured as a summation over the normalized distances between the individuals i and their corresponding neighbours within a sorted dimension (q).

$$Dis(i) = \sum_{q}^{Q} (x(q, i+1) - x(q, i-1)) \ \forall q \tag{6.34}$$

Spread is a measure of the extent to which the Pareto set moves. It is calculated by first computing the standard deviation (δ) of the crowding distance measurement for the points on the Pareto front with finite distances. The spread can be evaluated as follows:

$$spread = \frac{\varphi + \delta}{\varphi + N_p \Delta} \tag{6.35}$$

where N_p is the number of points, Δ is the average measure of distance between the points, and φ is the calculated summation across the objective function indices of the norm. This norm represents the difference between the current minimum Pareto point associated with that index and the corresponding minimum point from the previous iteration.

Hence, the NSGA-II implemented here follows the procedure outlined below. The chromosome (solution) structure in the NSGA-II, as it relates to this problem, includes the following variables: $\vartheta^s k$, $\vartheta^u n$, ϱ, and $\beta_{k,s}$. The algorithm starts by generating the initial population and determining the number of the individuals. In this problem, the number of population is $[(N \times K) + (S \times K)]$. This population is generated based on feasibility with respect to upper/lower bounds and the constraints given in C_1 - C_{11}. Next, the population is sorted by non-domination, and each individual is assigned a rank/fitness corresponding to the non-dominated level. The fitness function in this case is (6.32). Crowding distance analysis is performed for the individuals using (6.34), ensuring diversity is maintained in the population. Parent selection occurs, constituting the next generation from the current population using a combination of crowding distance and ranking. Subsequently, crossover and mutation operations are performed on the parents to create the new generation of children. The encoding process used for chromosome creation allows the algorithm to explore different combinations through selection, crossover, and mutation to obtain the optimal solution.

Multi-objective Reinforcement Learning Approach

Reinforcement learning (RL) is a form of ML algorithm that learns by interacting with the environment on a trial and error basis. The RL agent searches for actions based on set goals that optimize the reward while changing states to satisfy predefined goals [170]. When there are multiple objective functions in a related MOOP, the RL application in that scenario becomes a MORL.

- Multi-Objective Markov Decision Process: A RL problem is modelled as a Markov Decision Process (MDP) involving sequential decision-making, where the agent chooses actions to transition from one state to another, operating with uncertain probabilities and rewards. The outcome of actions taken is the reward. In MORL, the MDP becomes a multi-objective MDP (MO-MDP), where the single reward vector transforms into multi-objective reward vectors [149]. The MO-MDP of the MORL can be represented by a tuple ($S'_{s'}$,$A_{s'}$, $P_{s'}(S'_{t+1}|S'_t, a_t)$, $R_{s'}$), where $S'_{s'}$ is the set of states, $A_{s'}$ is the set of actions taken by the agents InP and MVSO, $P_{s'}(S'_{t+1}|S'_t, a_t)$ is the set of transition probabilities after actions $A_{s'}$ are executed in state $S'_{s'}$, and $R_{s'}$ represents the reward sets from the executed action $A_{s'}$ [139, 171].

- Policy: The policy adopted here is epsilon-greedy, which operates with epsilon ϵ initially as 1 to choose actions randomly (by exploration) with higher probability, especially in early training phase, along with an epsilon-decay rate of 0.995 that decreases ϵ by the epsilon-decay rate after each action selection, leading to exploitation as ϵ reduces to choose best-learned actions that yields the maximum reward.

- Q-Learning: The RL algorithm adopted to solve this MOOP is the Q-Learning algorithm. In the Q-Learning algorithm, the agent chooses actions a_t at time t in state S'_t to transition to the next state S'_{t+1}, and then receives a reward r_{t+1} from the environment [172, 173]. The state space is defined as S'_t = {1, 2, ...N_a}, where N_a is number of actions taken by the agent, and the environment is composed of the ϱ_n, $R^u_{n,k}$, R^s_k, α_k, N, $\beta_{k,s}$ and ζ in this chapter. In this MO-MDP, there are two agents for the InP and MVSO that take separate actions discretely, which involves choosing values of ϑ^s_k = $\{1_{\vartheta^s_k}, 2_{\vartheta^s_k}, ..N_{\vartheta^s_k}\}$ and $\vartheta^u_n = \{1_{\vartheta^u_n}, 2_{\vartheta^u_n}, ...N_{\vartheta^u_n}\}$ respectively. Hence, the state space and the action space are similar, as implemented in [171]. The action function, as represented in [173], is given below:

For InP agent with Q-table 1 (Q_1):

$$\text{action\_}Q_1(t) = \begin{cases} \text{random action } (N_{\vartheta_k^s}), \text{if probability } \epsilon \\ \text{argmax}(Q_1[S'_t, a_t]), \text{probability } 1-\epsilon \end{cases} \tag{6.36}$$

For MVSO Agent with Q-table 2 (Q_2):

$$\text{action\_}Q_2(t) = \begin{cases} \text{random action } (N_{\vartheta_n^u}), \text{if probability } \epsilon \\ \text{argmax}(Q_2[S'_t, a_t]), \text{probability } 1-\epsilon \end{cases} \tag{6.37}$$

where $N_{\vartheta_k^s}$ and $N_{\vartheta_n^u}$ represent the number of ϑ_k^s and ϑ_n^u actions, respectively. This action function operates with two condition described in the policy above. The first is random action selection with probability ϵ, while the second condition is dependent on exploitation, selecting the maximum action from the Q-table. Further, the action selection by the agents leads to the result, and since the MOOP in this chapter involves two objectives, the corresponding rewards are two (R_1 and R_2) presented below, which are equated to the objective function expressions of InP and MVSO respectively.

$$R_1 = \sum_{k=1}^{K} \sum_{s=1}^{S} \alpha_k \vartheta_k^s R_k^s \beta_{k,s} - \zeta \vartheta_k^s R_k^s \tag{6.38}$$

$$R_2 = \sum_{n=1}^{N} \sum_{k=1}^{K} \left((\varrho_n^2 + \vartheta_n^u R_{n,k}^u) - \vartheta_k^s R_{n,k}^u \right) \tag{6.39}$$

The training of the agents is performed over episodes with a defined number of iterations. In order to maximize the Q-values of each state, the agents must select the appropriate action, based on an exploration-exploitation strategy for this work. During the testing phase, the agents exploit learned policies to choose actions without exploration. Hence, the Q-value function operates based on action selection in state so as to maximize the total reward in the environment [174]. The rewards are obtained based on constraint satisfaction, especially C_{10}. Consequently, the Q-values for agents is updated

using

$$\begin{aligned} Q(S_t^{'}, a_t) &= Q(S_t^{'}, a_t)(1-\delta) + \delta[r_{t+1} \\ &\quad +\gamma \max_a Q(S_{t+1}^{'}, a_t)] \end{aligned} \tag{6.40}$$

where δ and γ are the learning rate and discount factor, respectively.

The Q-table space is composed of rows and columns representing states and action, respectively. For this problem, the Q-table is a matrix of dimension $\{N_a$ by $N_{\vartheta_k^s}\}$ or $\{N_a$ by $N_{\vartheta_n^u}\}$ depending on the particular Q-table. Since we have two agents in this MO-MDP scenario, two Q tables (Q_1 and Q_2) are required, one for each agent.

6.4.2 The Admission Control Mechanism

We consider a proposed AC algorithm, explained in this Chapter. The *revenue maximization (Rev-Max) algorithm* is presented as a novel AC approach. Two other benchmark approaches are discussed in Chapter 6.5.3, which include the *max-min fairness algorithm*, and the *Round Robin approach*. Each of these approaches is designed to handle the acceptance of SRs with differing objectives and mechanisms.

Admission using Revenue Maximization Algorithm

The Rev-Max algorithm operates by admitting SRs with a preference for high subscription traffic classes, specifically prioritizing eMBB traffic over URLLC in this chapter. The eMBB traffic is considered and satisfied first before URLLC, as the objective is to maximize revenue by admitting as many premium slices as possible before the lower-premium ones.

6.4.3 Optimization of Capacity Prediction with Deep Learning

The objective is to minimize the loss function, specifically the MAE of the predicted traffic ($\widehat{R_{k,p}^s}$) as compared to the actual traffic ($R_{k,a}^s$). This objective is given as:

$$\min_{\theta_d} \frac{1}{T} \sum_{t=1}^{T} R_{k,a}^s - \widehat{R_{k,p}^s} \tag{6.41}$$

This loss function is optimized by modifying the neural network design and training parameters θ_d, which include batch size, epoch, neural network optimizer and activation type. The

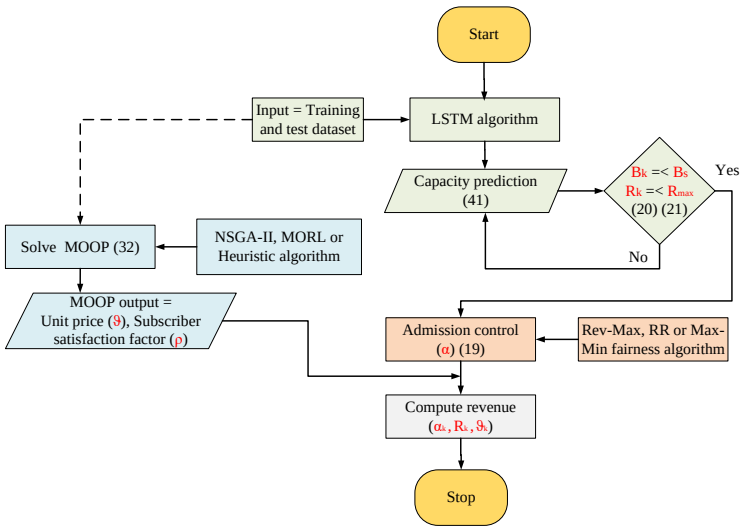

Figure 6.4: The schematic flow design of proposed NAC-Rev-Max Algorithm

trade-off with these parameter changes is that they introduce additional complexity to the neural network. This is further discussed in Chapter V.

6.4.4 Proposed Algorithm

Our proposed algorithm, referred to as the Network Slicing with Admission Control for Revenue Maximization (NAC-Rev-Max) algorithm, consists of three distinct aspects presented by colors (green, blue, and orange) as depicted in Fig. 6.4. This flowchart illustrates the joint operation of network slicing and AC, aimed at maximizing revenue.

NAC-Rev-Max begins with traffic prediction, wherein the LSTM algorithm independently forecasts the eMBB and URLLC traffic after receiving and processing the dataset in according to the procedure outlined in Algorithm 9. These predicted traffic patterns provide the dynamic demand for eMBB and URLLC, incorporating variables S_w and R_k^s, which subsequently serve as essential inputs for the AC aspect highlighted in orange. This AC mechanism is designed to maximize revenue for both the InP and MVSO.

Following the prediction, NAC-Rev-Max addresses the pricing component of the MOOP using either NSGA-II (Algorithm 7), MORL (Algorithm 8) or the heuristic approach described in Chapter 6.5.2. The NSGA-II algorithm accepts input variables from the dataset features, defines the two objective functions along with the inequality constraints, and performs optimization to arrive at maximized values of unit prices ϑ_k^s and ϑ_n^u.

Alternatively, the MOOP pricing can be solved using the MORL Algorithm 8. This

Algorithm 7: NSGA-II algorithm to obtain ϑ_k^s, ϑ_n^u and ϱ_n

Input: Number of satellites = S; Number of slices = K; Number of User = N; Satellite orbits & satellites limit = Ω; Total available Bandwidth = $\overline{B}_s$; User bandwidth = B_n^u; GBR range per user = $R_{n,k}^u$; GBR range per slice = R_k^s

Call the functions to solve optimization
Solve the MOOP in (6.32) by calling functions below with NSGA-II to obtain ϑ_k^s, ϑ_n^u, ϱ_n and $\beta_{k,s}$
Define InP function (6.17):
Function `Fi_InfraPro(`*num_inputs*`):`
  for $k \leq K$ **do**
    for $s \leq S$ **do**
      $F_i = \sum_{k=1}^{K} \sum_{s=1}^{S} \alpha_k \vartheta_k^s R_k^s \beta_{k,s} - \zeta \vartheta_k^s R_k^s$; `// (`F_i`:To maximize` ϑ_k^s `and` $\beta_{k,s}$`)`
    end
  end
  return F_i
Define MVSO function (6.25):
Function `Fm_MVSO(`*num_inputs*`):`
  for $n \leq N$ **do**
    for $k \leq K$ **do**
      $\overline{F}_m = \sum_{n=1}^{N} \sum_{k=1}^{K} \left((\varrho_n^2 + \vartheta_n^u R_{n,k}^u) - \vartheta_k^s R_{n,k}^u\right)$; `// (`$\overline{F}_m$`:To maximize` ϑ_n^u `and` ϱ_n`)`
    end
  end
  return F_2
Define Constraint function for C_1 to C_{11}:
Function `constraint_ceq(`*num_inputs*`):`
  constraints **return** *Concatenation of constraints*
End

Algorithm 8: MORL with Q-Learning Multi-Agent Algorithm to obtain ϑ_k^s and ϑ_n^u

Initialize environment parameters: K, S, N, ζ, ϱ_n, ϑ_k^s, ϑ_n^u, β, δ, γ, ϵ, ϵ_decay, $max\_episodes$, $max\_episodes\_test$, max_step;
Initialize environment *env* **with parameters**;
Initialize the agent $Q - agent$ **with parameters**;
Training Procedure:
for $i \leftarrow 1$ *to* $max\_episodes$ **do**
  Randomly select initial state $state0$;
  for $w \leftarrow 1$ *to* max_step **do**
    Choose actions $action\_Q_1$, $action\_Q_2$ **using epsilon-greedy policy**;
    Receive rewards $R1$ **and** $R2$ **by taking actions**;
    Update Q-values for both agents using (6.40);
    $Q(S_t^{'}, a_t) = Q(S_t^{'}, a_t)(1-\delta) + \delta[r_{t+1} + \gamma \max_a Q(S_{t+1}^{'}, a)]$;
    Decay exploration rate ϵ;
  end
end
Testing Procedure:
for $i \leftarrow 1$ *to* $max\_episodes\_test$ **do**
  Get the state from the environment $state0 =$ *env.get_state*();
  for $w \leftarrow 1$ *to* max_step **do**
    Choose actions $action\_Q_1$, $action\_Q_2$ **using learned policies**;
    Receive rewards $R1$, $R2$ **by taking actions while considering** C_{10} $[\vartheta_k^s < \vartheta_n^u]$;
  end
end
Export points for $\vartheta_k^s, \vartheta_n^u$;
Plot rewards results: *Using matplotlib.pyplot*

algorithm starts by initializing the environment and Q-agent parameters, then trains the agents over a defined number of time steps and episodes, accumulating rewards for every action taken by the agents as the state changes. The Q-values for both agents are updated using (6.40). During the testing phase, the procedure is performed over define time steps and episodes, with agents taking actions using the learned policies to obtain the resultant rewards. For the AC aspect, three algorithms are explored: the Max-Min fairness, round robin (RR) and the proposed Rev-Max AC algorithm. These three sub-algorithms are presented in Algorithm 10, where the syntax of the operation is outlined, and their objectives are described in Chapters 6.4.2 and 6.5.3. Once the AC operation is completed and the unit price in \$/Mbps (from NSGA-II, MORL, or the heuristic approach) with the admitted slice capacity (predicted in part as demand by LSTM) in Mbps is derived, the revenue can be calculated. The revenue earned from the sliced network resources based on the dynamic traffic demand from all MVSOs is computed for the InP.

Algorithm 9: LSTM for traffic prediction of R_k^s and $R_{n,k}^u$

Data: Perform data preprocessing by separating the training and test set of the dataset.
Import necessary Keras libraries and load the training set;
Perform feature scaling: *Scale using MinMaxScaler on training data of eMBB and URLLC*;
Build LSTM-based RNN model;
Define parameters: *Epochs* = E_p; *batch-size* = B_{size}; *activation function = Relu; optimizer = Nadam*;
for $t \leq E_p$ **do**
  for $q \leq B_{size}$ **do**
    Extract a mini-batch of eMBB and URLLC data samples;
    Forward pass;
      Pass the mini-batch through the LSTM network;
      Calculate the predicted traffic probabilities;
    Backward pass;
      Compute the prediction error with mean-absolute-error loss function (6.41);
      Update LSTM weights using backpropagation through time (BPTT);
  end
end
Prediction: *Import test-set and make prediction using the trained RNN model*;
Display results: *Visualize the results for eMBB and URLLC using matplotlib.pyplot*

6.4.5 Complexity Analysis

The total complexity cost involved in solving problem (6.32) depends on the combined complexity of the NSGA-II, or MORL with Q-learning, LSTM, and AC algorithms. The initial non-dominated sorting genetic algorithm (NSGA) utilized a non-elitism approach, resulting in a high complexity of $O(MW^3)$, where M is the number of objective functions and W

Algorithm 10: Admission control with Rev-Max, Round Robin and Max-Min Fairness

Input: Total satellite capacity(GEO/MEO/LEO) = $Total\_C$; URLLC Demand = $urllc\_demand$; eMBB Demand = $embb\_demand$; URLLC S_w = $urllc\_slice\_weight$; eMBB S_w = $embb\_slice\_weight$;

Call the AC functions ($Rev - Max$ *result output*) ← Rev_max_allocation(*input*)
($Max - Min$ *fairness result output*) ← Max_min_fairness_allocation(*input*)
(*RR result output*) ← Round_Robin_allocation(*input*)

Function `Rev_Max_allocation(`*inputs*`):`
  for $embb\_demand \leq Total\_C$ **do**
    First allocate capacity to highest priority service (which is eMBB) based on S_w *and available capacities (starting with* $GEO -> MEO -> LEO$*)*
  end
  for $urllc\_slice\_weight \leq (Total\_C - embb\_demand)$ **do**
    Allocate remaining capacity (of LEO) to URLLC based on S_w
  end
  return $Rev\_max\_urllc, Rev\_max\_embb,$
  $Rev\_max\_un\_allocated\_capacity$

Function `max_min_fairness_allocation(`*inputs*`):`
  Ensure that minimum demand (URLLC) is satisfied first based on S_w *and available capacities (starting with* $LEO -> MEO -> GEO$*). Then allocate remaining capacity to eMBB based on* S_w
  return $Max\_min\_urllc, Max\_min\_embb,$
  $Max\_min\_un\_allocated\_capacity$

Function `Round_Robin_allocation(`*inputs*`):`
  Allocate resources to eMBB and URLLC SR in sequential order without preference, until available resources is utilized, while considering the S_w*.*
  return $RR\_urllc, RR\_embb, RR\_un\_allocated\_capacity$

End

Display allocation results $print(Allocation; Un\_allocated; Un\_met\_demand; Penalty)$

Table 6.2: Network Slicing and Admission Control Simulation Parameters

Items	Parameter at 17:00hr	Parameter at 2:00hr
URLLC S_w (Mbps)	400	350
eMBB S_w (Mbps)	930	730
URLLC demand (Mbps)	1,600	1,400
eMBB demand (Mbps)	4,650	3,650
URLLC maximum $R^u_{n,k}$ (Mbps)	47	47
eMBB maximum $R^u_{n,k}$ (Mbps)	115	115
URLLC B^u_n @ 2bps/Hz (MHz)	24	24
eMBB B^u_n @ 2bps/Hz (MHz)	58	58
Total available capacity (Mbps)	5,100	4,300
LEO percentage of total capacity (%)	20	20
MEO percentage of total capacity (%)	40	40
GEO percentage of total capacity (%)	40	40

represents the population size. However, in this work, a faster non-dominated sorting mechanism known as NSGA-II is used. NSGA-II converges faster, employs an elitist approach with reduced complexity, and finds a better spread of solutions near the Pareto-optimal front. The complexity of NSGA-II in solving the MOOP is $O(MW^2)$ [167], where M is two in this chapter, and W, the population size is equal to $[(N \times K) + (S \times K)]$ as discussed in Chapter 6.4.1. Hence, as M and W increase, the execution time and complexity of the NSGA-II also increase.

For MORL with Q-learning, the complexity of the algorithm depends on several parameters, such as the size of action space and the length of the time step (T_s) in the defined max episode (M_e). Since there are two agents in Algorithm 8, the action space is of size $N_{\vartheta^s_k}$ for the InP agent and $N_{\vartheta^u_n}$ for the MVSO agent. With L as the number of multiplication operations in the neural network, it can be assumed that the complexity of training for one experience is $O(L)$. Hence, the complexity of this MORL is $O(LT_s[N_{\vartheta^s_k} + N_{\vartheta^u_n}]M_e)$ [175]. Further, the complexity of LSTM per weight and time step can be represented as $O(W_t)$, where W_t is the weight/length of the input sequence [152]. LSTM complexity can also be derived, following [154], in terms of real value operations performed by the four gates that depend on the LSTM hidden state size Z and the input sequence length W_t. Each gate implements $3Z + W_t - 2$ summation and $Z^2 + ZW_t$ multiplication, resulting in the overall LSTM cost:

$$L_{Cost} = 4(Z^2 + ZW_t + 3Z + W_t - 2) + 4Z \tag{6.42}$$

The complexity of the AC algorithms, as described in [176], for the proposed priority-

based Rev-Max algorithm results in an overall complexity derived from the SR acceptance feasibility checking based on available resources. The complexity of the admission is $O(K \times S) + \sum_{k=1}^{K} O(S^3) = O(S^3 + KS)$. Hence, the complexity increases as K (number of SRs) and S (number of satellites impacting capacity) increase.

6.5 Performance Evaluation

In this Chapter, the simulation configurations and the performance analysis of the proposed algorithm are discussed, and evaluated against other state-of-the-art algorithms.

6.5.1 Simulation Setup

The simulation is first setup to solve the pricing strategy of the MOOP described in Chapter 6.3.3 using NSGA-II, MORL and the heuristic approach. The NSGA-II algorithm is configured in the MATLAB simulation environment along with the Heuristic approach, while the MORL algorithm is configured in Python using the same values of ϱ_n as in NSGA-II. The system used runs Windows 10 with 32GB of RAM and 16 x Intel 2.40GHz cores. Specifically, Python 3.9.18 and MATLAB R2023b were employed for the simulations. The heuristic approach mentioned in Chapter 6.5.2 is simulated, where the required iterated value of ϱ_n is adopted from that of NSGA-II to create a basis for comparison. Similarly, for MORL algorithm, the same values of R_n^u, R_k^s, and ϱ as in NSGA-II are used for the basis of comparison. In this chapter, the number of actions, N_a, for each agent is configured as 15, and the maximum defined values of ϑ_k^s and ϑ_n^u for the MORL agents of InP and MVSO, are 9 \$/Mbps and 10 \$/Mbps, respectively. Precisely, the InP agent is configured to generate N_a number of values between $\frac{\vartheta_k^s}{N_a}$ and ϑ_k^s, leading to the actual range of discretize values of {0.6, 1.2, 1.8, 2.4, 3, 3.6, 4.2, 4.8, 5.4, 6, 6.6, 7.2, 7.8, 8.4, 9.0 \$/Mbps}. Similarly, the MVSO agent is configured to generate N_a number of values between $\frac{\vartheta_n^u}{N_a}$ and $N_{\vartheta_k^s}$, leading to the actual range of discretize values of {0.67, 1.33, 2.00, 2.67, 3.33, 4.00, 4.67, 5.33, 6.00, 6.67, 7.33, 8.00, 8.67, 9.33, 10.00 \$/Mbps}.

Further, the LSTM traffic prediction of eMBB and URLLC is simulated using python development environment in the Anaconda navigator suite, with configurations implemented with the keras library; the dataset pre-processing is done using MS Excel. For the traffic prediction optimization described in Chapter 6.4.3, the neural network is designed by considering different parameters to arrive at a suitable configuration with minimal loss function.

In Fig. 6.5 (a), the LSTM loss is evaluated with different deep learning optimizer including NADAM, ADAM, RMSPROP and SGD. The performance shows that NADAM achieved a loss of 0.0894 at epoch 100, while ADAM, RMSPROP, and SGD performed at 0.0900, 0.0908, and 0.0917, respectively. This indicates that NADAM offers the best performance over ADAM, RMSPROP, and SGD by 0.67%, 1.55%, and 2.54%, respectively. Further, the performance of loss with respect to epoch is shown in Fig. 6.5 (b). When different activation functions are considered, Relu shows the best performance with a value of 0.0894 at 100 epochs, while softplus and softmax are 0.0917 and 0.0922, respectively, indicating that Relu outperformed softplus and softmax by 2.54% and 3.08%, respectively. Similarly, when different batch sizes were considered in Fig. 6.5 (c), batch size 32 offers the best loss performance of 0.0894 at 100 epochs, while batch sizes 64 and 128 performed at 0.0927 and 0.0955, respectively, showing that batch size 32 outperforms batch sizes 64 and 128 by 3.62% and 6.59%, respectively. Hence, the LSTM network is configured using NADAM, Relu and batch size 32, resulting in the predicted eMBB and URLLC traffic shown in Fig. 6.5 (d). The predicted traffic shows a varying daily trend, with lower traffic from 1:00 hr to 6:00 hr, indicating less demand during these idle hours. The traffic trend at 2:00hr and 17:00hr is considered for low and high demand periods in this analysis, using 1,600 Mbps and 4,650 Mbps as the traffic demands from the prediction at 17:00hrs for URLLC and eMBB, respectively. The simulation is setup as mention above for the proposed algorithm using the parameters outlined in Table 6.2, mostly derived from the dataset and LSTM traffic prediction, and this is compared with other state-of-the-art algorithms in terms of unit price, capacity allocation, revenue and peak delay.

6.5.2 Pricing Mechanism Benchmark

Heuristic Approach

This approach obtains ϑ_k^s using (6.46), while assuming ϱ. The exercise is then subsequently repeated iteratively for different values of ϱ_n until a suitable solution for ϑ_k^s is obtained. The details of the derivation of ϑ_k^s are presented as follows.

The Heuristic approach for solving ϑ_k^s is provided along with the details of the mathematical

derivation, starting from constraint C_9. Recall that ϱ_n in (6.29) is given as

$$\varrho_n = \frac{R^u_{n,k}}{(N^u_k + \vartheta^u_n + D^u_{n,k})}$$

If satisfaction index (ϱ_n) is assumed and other related variables are known, then ϑ^u_n can be obtained. Making ϑ^u_n the subject in (6.29), multiply both sides by $(N^u_k + \vartheta^u_n + D^u_{n,k})$, which yields

$$\varrho_n.(N^u_k + \vartheta^u_n + D^u_{n,k}) = R^u_{n,k} \tag{6.43}$$

Expand the right and subtract $\varrho_n.\vartheta^u_n$ from both sides.

$$\varrho_n.\vartheta^u_n = R^u_{n,k} - \varrho_n.N^u_k - \varrho_n.D^u_{n,k} \tag{6.44}$$

Then ϑ^u_n is obtained as shown below:

$$\vartheta^u_n = \frac{R^u_{n,k} - \varrho_n.N^u_k - \varrho_n.D^u_{n,k}}{\varrho_n} * N_f \tag{6.45}$$

Note: A normalization factor N_f is included to normalize the resultant price accordingly. Further, recalling constraint C_{10}, which states $\vartheta^s_k < \vartheta^u_n$, this leads to the final outcome of

$$\vartheta^s_k < \frac{R^u_{n,k} - \varrho_n.N^u_k - \varrho_n.D^u_{n,k}}{\varrho_n} * N_f \tag{6.46}$$

6.5.3 Admission Control Benchmark

Admission using Max-Min Fairness Algorithm

The max-min fairness algorithm operates by admitting SRs with the minimum demand first, and subsequently admitting demands from other traffic classes using a similar proportion based on the number of accepted SRs while considering the remaining available resources [177]. The objective is to fairly admit as many SRs, irrespective of the traffic type, in an equal manner.

Admission using Round Robin Algorithm

The RR algorithm admits SRs by allocating the resources of URLLC and eMBB demands in sequential order based on the S_w magnitude for each, admitting without bias and preference

until available resource is exhausted [178]. A S_w is the unit of SR per individual MVSO request, out of the total SR in that traffic category. The objective is to admit as many S_w units of the SRs sequentially as they arrive the network.

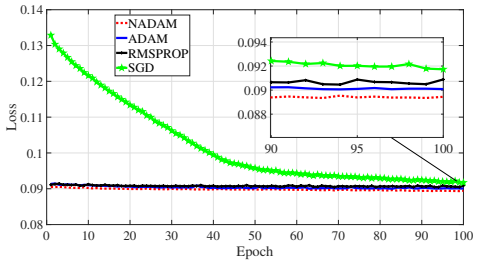

(a) Evaluation for the different deep learning optimizers.

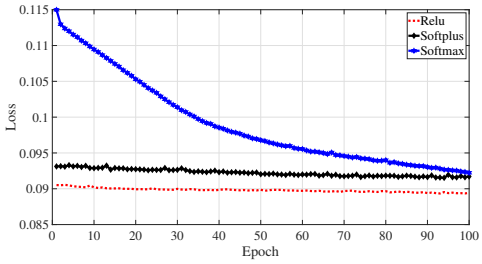

(b) Evaluation for the different activation functions.

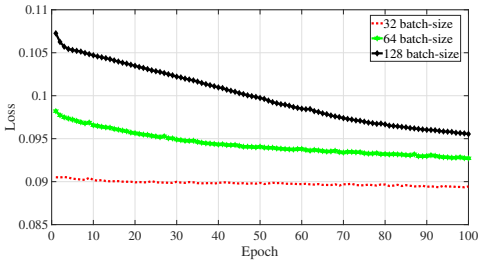

(c) Evaluation for the different batch sizes.

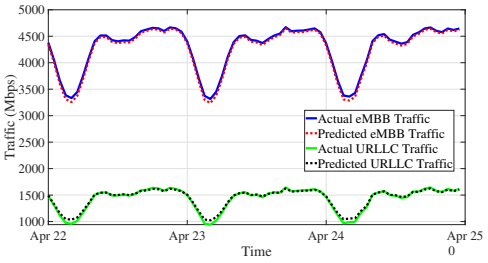

(d) Evaluation for the predicted eMBB and URLLC Traffic.

Figure 6.5: Evaluation of LSTM RNN-model with respect to different optimizers, activation functions and batch sizes.

6.5.4 Performance Analysis

The objective of this work is to maximize revenue for the InP, which leases NTN resources dynamically through slicing to MVSOs with SLAs guaranteeing varying demanded QoS, to achieve high subscriber satisfaction and ensure efficient utilization of network resources. To achieve this objective, the unit prices of ϑ_k^s and ϑ_n^u in the MOOP are maximized for each of the objective functions in (6.18) and (6.26), respectively. Here, the InP and the MVSO achieve correspondingly satisfactory unit prices based on defined constraints. Specifically, the MVSO derives a unit price for the subscriber that can cover the cost of leasing from the InP and still make marginal profit, while the InP operates the leasing of resources with a commensurate compensation in the form of a defined unit price for the MVSO as a fee to cover the cost of resources offered. The InP and MVSO unit prices are obtained from optimization and bound by a condition stated in constraint c_{10} (6.30). This is done using three approaches: NSGA-II optimization, MORL with Q-Learning, and a Heuristic approach, where the Pareto points

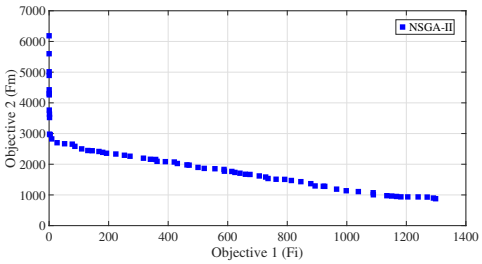

(a) Pareto front points from NSGA-II.

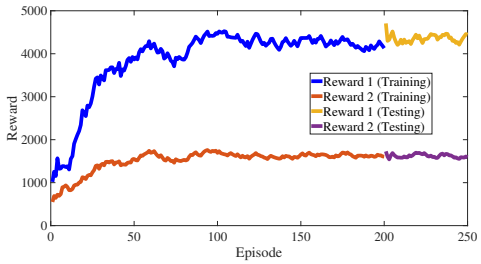

(b) MORL rewards analysis under training and testing phases.

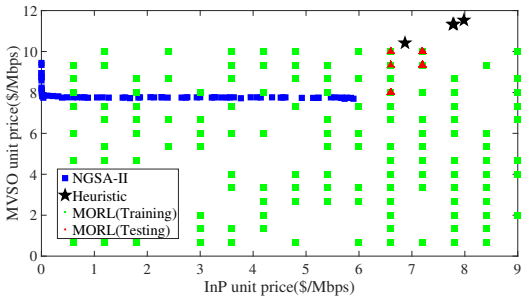

(c) Resultant unit prices for NSGA-II, MORL and Heuristic.

Figure 6.6: Evaluation of the Pareto front and resultant unit price for NSGA-II, MORL and Heuristic approach.

are obtain for ϑ_k^s and ϑ_n^u.

In Fig. 6.6 (a), the Pareto front points are shown for objective functions F_i and $\overline{F}_m$, with the resultant point for $\overline{F}_m$ mapped onto that of F_i on the Pareto front while using the NSGA-II algorithm. Similarly, the MORL with Q-Learning algorithm is used to analyze the rewards R_1 and R_2 for F_i and $\overline{F}_m$, respectively, under training and testing phases, to evaluate the optimization performance in Fig. 6.6 (b).

Further, the optimization results of the unit prices of ϑ_k^s and ϑ_n^u in \$/Mbps are displayed in Fig. 6.6 (c) for the three approaches of NSGA-II, MORL and Heuristic. The NSGA-II optimization yields several unit prices, but what is considered are the optimized unit prices of 5.89 \$/Mbps and 7.69 \$/Mbps for ϑ_k^s and ϑ_n^u, respectively. This is achieved by considering the highest optimized unit price for the InP first and then its corresponding MVSO pair. For MORL, the testing phase results are considered, resulting in different pairs of unit prices (ϑ_k^s and ϑ_n^u) based on the defined state space. The unit price combination adopted for MORL is 7.19 \$/Mbp and 10.00 \$/Mbp for ϑ_k^s and ϑ_n^u, respectively, as this pair yields the highest optimized InP price. The Heuristic approach produces a linear trend of different unit prices. Here, what is considered are the unit prices of 7.98 \$/Mbps and 11.52 \$/Mbps for ϑ_k^s and ϑ_n^u, respectively. The maximum value with reference from ϑ_k^s is selected and then mapped to the corresponding ϑ_n^u value. These results show that NSGA-II offers a more cost-effective price

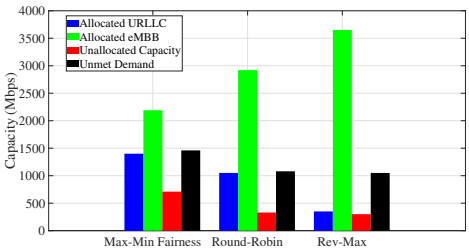

(a) Evaluation for the AC algorithms at 2:00hr.

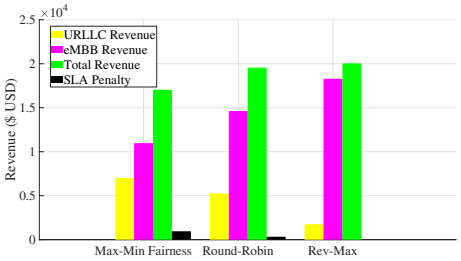

(b) Evaluation of the resultant InP revenue for 2:00hr.

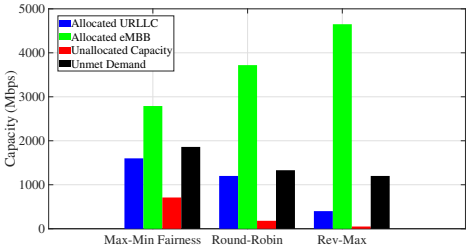

(c) Evaluation for the AC algorithms at 17:00hr.

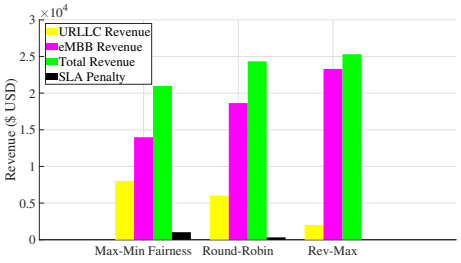

(d) Evaluation of the resultant InP revenue for 17:00hr.

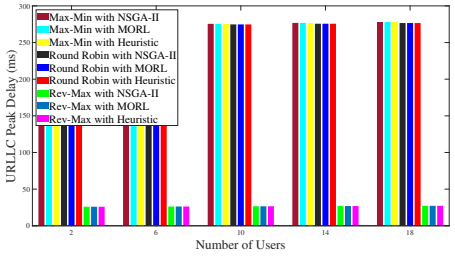

(e) Evaluation of URLLC peak delay and impact on penalty.

Figure 6.7: Evaluation of cognitive behaviour of the admission control algorithms with respect to slice allocated capacity, un-allocation, unmet demand, achieved revenue and penalty imposed.

to the subscribers at 7.69 $/Mbps compared to MORL at 9.33 $/Mbps and the Heuristic at 11.52 $/Mbps, representing a 19.27% improvement over MORL and a 39.87% improvement over the Heuristic.

Further, the three AC mechanisms adopted are the Max-Min fairness AC, RR AC, and the proposed Rev-Max AC, as outlined in Algorithm 10. In Fig. 6.7 (a), the AC performance is shown with respect to capacity allocation in Mbps for the lowest demand in the day at 2:00hr. The Max-Min fairness algorithm allocates 1,400 Mbps for URLLC and 2,190 Mbps for eMBB, indicating that all URLLC demands are met while only a portion of the eMBB demands are satisfied. Specifically, 710 Mbps remains unallocated from the total available 4,300 Mbps capacity. As the unallocated capacity of 710 Mbps falls short of the required eMBB S_w of 730 Mbps, it cannot be utilized for the eMBB slice and therefore remains unutilized. The chart also shows the unmet demand of 1,460 Mbps, which is mostly from the total eMBB

demand of 3,650 Mbps. Similarly, at 2:00hr, the RR AC algorithm allocates 1,050 Mbps for URLLC and 2,920 Mbps for eMBB, leaving 330 Mbps unallocated and an unmet demand of 1,080 Mbps. In contrast, the proposed AC algorithm of Rev-Max shows eMBB allocation of 3,650 Mbps, which is the total eMBB demand, and URLLC allocation of 350 Mbps based on available capacity. The unallocated capacity is 300 Mbps, and the unmet demand of URLLC is 1,050 Mbps. This performance shows that Rev-Max admitted a cumulative of 4,000 Mbps slice traffic while RR and Max-Min admitted only 3,970 Mbps and 3,590 Mbps slice traffic, indicating Rev-Max admitted 0.75% and 10.80 % more than RR and Max-Min algorithms, respectively. Further, Rev-Max has the lowest unmet demand, which is 2.81% and 32.66% less than RR and Max-Min, respectively, including the lowest unallocated capacity, which is 9.52% and 81.18% less than that of RR and Max-Min fairness, respectively. The reason for the unmet demand is that the available capacity is less than traffic demand, as shown in Table 6.2. Hence, the capability of the AC algorithms is evaluated to ascertain the superior AC algorithm that yields the lowest unmet demand.

The InP revenue for the slices admitted at 2:00hr is shown in Fig. 6.7 (b). The Max-Min fairness AC yielded $ 7,015.80 and $ 10,974.70 from URLLC and eMBB slice traffic, respectively. However, a penalty of $ 955.09 awarded against the InP for URLLC slices allocated on MEO and GEO satellites because the capacity for LEO is only 20% of the total available capacity, and LEO is the only NTN layer that is used for URLLC services. This penalty is assumed as 30% of the income from the capacity wrongly allocated as per SLA, hence the total revenue earned by Max-Min fairness is $ 17,035.40 after penalty deduction. Similarly, RR yields $ 5,261.85 from URLLC and $ 14,632.90 from eMBB, with a SLA violation penalty of $ 336.05, resulting in a cumulative revenue of $ 19,558.70 after penalty deduction. In the same figure, the performance of Rev-Max is seen to yield $ 1,753.95 and $ 18,291.20 for URLLC and eMBB, respectively, resulting in a cumulative revenue of $ 20,045.10 without any penalty deductions since all slices were allocated to the correct orbital satellite as per SLA. Evidently, the Rev-Max achieved a significant revenue advantage over both RR and Max-Min, generating 2.45% more revenue than RR and 16.23% more than Max-Min. This is primarily due to Rev-Max's ability to avoid penalties and accommodate a higher volume of eMBB slice traffic.

Fig. 6.7 (c) presents the AC performance at 17:00hr with respect to capacity allocation in Mbps. Specifically, Max-Min fairness algorithm allocates 1,600 Mbps for URLLC and 2,790

Mbps for eMBB, indicating that all URLLC demand is satisfied, while only part of eMBB is satisfied, leaving the 710 Mbps unallocated from the total available 5,100 Mbps capacity. Since the available capacity of 710 Mbps is less than the required eMBB S_w of 930 Mbps, the remaining capacity cannot be used for eMBB slice traffic. The chart further reveals an unmet demand of 1,860 Mbps, mostly from the total eMBB demand of 4,650 Mbps. Similarly, at 17:00hr, RR AC algorithm allocates 1,200 Mbps for URLLC and 3,720 Mbps for eMBB, with unallocated capacity of 180 Mbps and unmet demand of 1,330 Mbps. The proposed AC algorithm of Rev-Max shows eMBB allocation of 4,650 Mbps, which is the total eMBB demand, and URLLC allocation of 400 Mbps based on available capacity. As the remaining unallocated capacity (50 Mbps) falls short of the required S_w for URLLC traffic (400 Mbps), it remains unused. The unmet demand of URLLC slices is 1,200 Mbps. This performance shows that Rev-Max admitted a cumulative total of 5,050 Mbps slice traffic while RR and Max-Min admitted only 4,920 Mbps and 4,390 Mbps slice traffic, respectively. This indicates Rev-Max admitted 2.60% and 13.98% more than RR and Max-Min algorithms, respectively. Rev-Max also has the lowest unmet demand, which is 10.27% and 43.13% less than RR and Max-Min, respectively, including the lowest unallocated capacity, which is 113.04% and 173.68% less than that of RR and Max-Min fairness, respectively.

The resultant InP revenue from the 17:00hr can be seen in Fig. 6.7 (d), where Max-Min fairness yields $ 8,018.05 and $ 13,981.50 from URLLC and eMBB slice allocation, respectively. A penalty of $ 1025.84 is awarded against InP as a result of the wrongly allocated URLLC traffic on other orbits other than LEO as per SLA. This penalty is 30 % of the income from the wrongly allocated URLLC slice traffic, resulting in a total revenue of $ 20,973.70 after the penalty deductions. Similarly, RR yields $ 6,013.54 from URLLC and $ 18,642.00 from eMBB, with a SLA violation penalty of $ 318.36 resulting in a cumulative revenue of $ 24,337.10 after penalty deduction. Additionally, Rev-Max AC yields $ 2,004.51 and $ 23,302.50 from admitted URLLC and eMBB slices, respectively, with a cumulative revenue of $ 25,307 without any incurred penalty. This shows that Rev-Max outperformed RR and Max-Min by 3.91% and 18.73% in total earned revenue, respectively.

In Fig. 6.7 (e), the reason for the penalty on Max-Min and RR is confirmed, as NSGA-II, MORL, and Heuristic approaches for Max-Min fairness AC show a peak delay performance of 275.50 ms, and that of RR AC with NSGA-II, MORL and Heuristic is 274.72 ms when the number of users is 10 for URLLC slices. In contrast, Rev-Max with any of NSGA-II, MORL

and Heuristic approach shows a peak delay performance of 26.61 ms with 10 users for URLLC admitted slices. Particularly, Rev-Max demonstrates superiority in URLLC peak delay with 164.67% and 164.76% improvements over RR and Max-Min fairness AC, respectively. This is achieved by intelligently limiting URLLC admissions below the available capacity and strategically allocating slices in a way that optimizes orbital resources while ensuring SLA compliance. Further, the impact of the subscriber satisfaction index is discuss with the

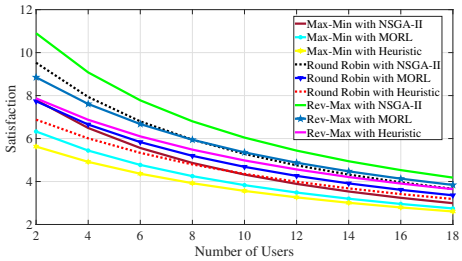

(a) Evaluation for satisfaction with number of users.

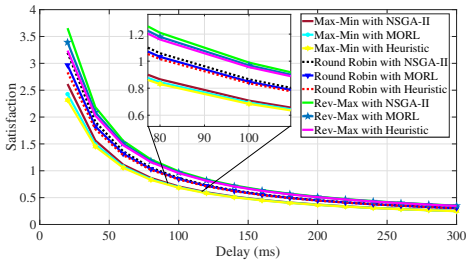

(b) Evaluation for satisfaction with delay.

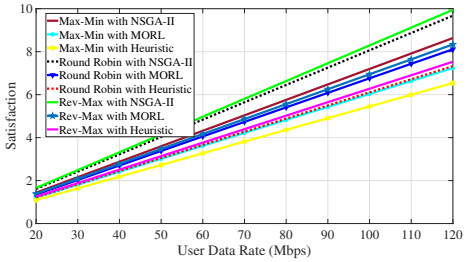

(c) Evaluation for satisfaction with user data rate.

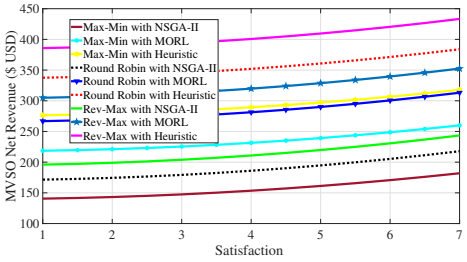

(d) Evaluation of MVSO net revenue.

Figure 6.8: Evaluation of the subscriber satisfaction index with respect to number of users, delay, data rate and MVSO net revenue for the different AC algorithms.

dependant variables, which is important as the QoE can impact subscriber patronage and revenue for the MVSOs in the long term.

In Fig. 6.8 (a), the performance indicates that ϱ decreases as the number of users increases. This observation aligns with our theoretical analysis presented in (6.29), where ϱ_n is inversely proportional to the number of users due to the possibility of resource congestion. Additionally, Rev-Max with NSGA-II achieves ϱ of 6.04 with 10 numbers of users, which is higher than Rev-Max with MORL at 5.35 and Rev-Max with Heuristic at 4.98 because Rev-Max with NSGA-II offers a lower unit price that is 26.11% and 39.87% less than the MORL and Heuristic. The trend also shows that at 10 numbers of users while analyzing for different AC algorithms operating the same pricing optimization, Rev-Max with NSGA-II achieves a higher ϱ compared to RR with NSGA-II at 5.28 and Max-Min with NSGA-II at 4.32. Similarly,

Rev-Max with MORL achieves higher ϱ than RR with MORL at 4.68 and Max-Min with MORL at 3.83. Likewise, Rev-Max with Heuristic yields a higher ϱ compared to RR with Heuristic at 4.35 and Max-Min with Heuristic at 3.56. This is because Rev-Max will always allocate slices to the appropriate orbital resources without violating SLA, whereas Max-Min violates SLA by allocating slices to wrong orbital satellites, especially URLLC slices, thereby impacting user satisfaction.

Similarly in Fig. 6.8 (b), it shows that as delay increases, the subscriber satisfaction reduces. At 100 ms delay, Rev-Max with NSGA-II shows the best ϱ performance of 0.98, while Rev-Max with MORL and Heuristic are 0.96 and 0.95, respectively, because Rev-Max with MORL and Heuristic offers higher unit prices. The same trend applies to RR and Max-Min with there different pricing optimization algorithms. While analyzing across the different AC algorithms with the same pricing optimization algorithm, it can be observed that Rev-Max with NSGA-II achieves higher ϱ at 100 ms compared to RR with NSGA-II at 0.86 and Max-Min with NSGA-II at 0.70. The same trend applies to Rev-Max with MORL, which yields higher ϱ at 100 ms than RR with MORL at 0.84 and Max-Min with MORL at 0.69. This is because RR and Max-Min allocate some URLLC slices to the wrong orbital satellites, potentially leading to SLA violations.

Fig. 6.8 (c) shows that as the data rate increases, sometimes with MC for eMBB traffic, the satisfaction of the users also increases because throughput is directly proportional to ϱ in (6.29). At 90 Mbps while analyzing for different AC with the same pricing optimization strategy, Rev-Max with NSGA-II shows a higher performance of 7.46 ϱ, while RR with NSGA-II yields 7.25 and Max-Min with NSGA-II achieves 6.47. This is because RR with NSGA-II and Max-Min with NSGA-II wrongly allocates resources to slices, which violates SLA, especially URLLC slices, while the former ensures all admitted slices are allocated to the right orbital satellites. The same trend applies to RR and Max-Min with their respective pricing strategies. Similarly, while analyzing performance across the same AC with different pricing strategy at 90 Mbps, it is observed that Rev-Max with NSGA-II yields a higher ϱ compared to Rev-Max with MORL at 6.25 and Rev-Max with Heuristic at 5.64. The same trend applies to RR and Max-Min with the different pricing strategies. This is due to the lower unit price offered by NSGA-II compared to MORL and Heuristic algorithms. This confirms that Rev-Max with NSGA-II is superior in offering the highest user satisfaction, being 2.85%, 14.21%, 17.65%, 20.38%, 27.78%, 30.42%, 31.67% and 41.42% better than RR with NSGA-II,

Max-Min with NSGA-II, Rev-Max with MORL, RR with MORL, Rev-Max Heuristic, RR with Heuristic, Max-Min with MORL and Max-Min with Heuristic, respectively.

In Fig. 6.8 (d), the performance of MVSO net revenue is displayed for all scenarios of admission control algorithms. When all AC scenarios operate with the same ϱ of 5, the Rev-Max with Heuristic achieves $ 409.54, while RR with Heuristic, Rev-Max with MORL, Max-Min with Heuristic, RR with MORL, Max-Min with MORL, Rev-Max with NSGA-II, RR with NSGA-II and Max-Min with NSGA-II achieve $ 360.70, $ 328.66, $ 297.11, $ 289.95, $ 239.21, $ 219.75, $ 194.68 and $ 161.24, respectively. This indicates that Rev-Max with Heuristic and RR with Heuristic are the top two performers because they admit more eMBB slices, which have higher S_w and subscription value than the URLLC slices. Consequently, Rev-Max with Heuristic is 60.31% higher than Rev-Max with NSGA-II due to the former's higher unit price. However, in the long term, the potential drawback of Rev-Max with Heuristic over Rev-Max with NSGA-II is that subscribers might gradually migrate to the latter since it offers the same QoS/QoE at a moderate/lower unit price.

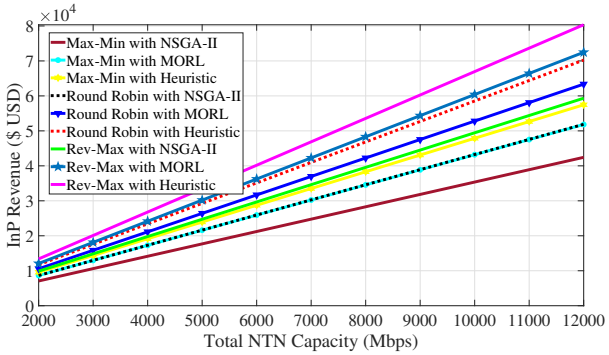

Figure 6.9: Evaluation of impact of the leased network capacity on infrastructure provider net revenue.

Finally, in Fig. 6.9 the performance of InP revenue is assessed for all AC algorithms. It reveals that as the available NTN capacity for lease to MVSOs increases, the InP earns more revenue. Rev-Max with Heuristic achieves $ 66,951.60 when leased NTN capacity is 10,000 Mbps, while the Rev-Max with MORL, RR with Heuristic, RR with MORL, Rev-Max with NSGA-II, Max-Min with Heuristic, RR with NSGA-II, Max-Min with MORL and Max-Min NSGA-II achieve $ 60,387.00, $ 58,539.00, $ 52,799.30, $ 49,447.10, $ 47,877.70, $ 43,234.00, $ 43,183.30, and $ 35,360.10, respectively at 10,000 Mbps capacity lease. This demonstrates that Rev-Max with Heuristic outperforms Rev-Max with MORL, RR with Heuristic, and Rev-Max with NSGA-II algorithms by 10.31%, 13.41% and 30.07%, respectively, because

it admits more of eMBB slices with bigger S_w and higher subscription value than other configurations and offers a higher unit price ϑ_s^k than the other pricing algorithms.

Accordingly, it can be confirmed that Rev-Max AC with Heuristic algorithm yields higher revenue for InP compared to the other algorithms. Similarly, in terms of the MSVOs' net revenue, Rev-Max with Heuristic algorithm offers the highest value when compared to the other algorithms. While Rev-Max with a Heuristic approach initially delivers a higher net revenue compared to Rev-Max with NSGA-II, the latter might offer sustainable long-term benefits through higher subscriber satisfaction. This is because Rev-Max with NSGA-II prioritizes a moderate unit price while maintaining the same QoS/QoE and adhering to SLAs. This strategy can enhance customer loyalty and potentially lead to more stable revenue growth in the long run compared to the potentially short-term gains of the Rev-Max with Heuristic algorithm.

6.6 Conclusions

This chapter presents a model of integrated service delivery, wherein users subscribe to MVSOs who lease NTN infrastructure from satellite InPs. A novel NTN slicing architecture was proposed, incorporating multi-layer satellites, including LEO, MEO, and GEO constellations, with an HGS adapted to the 3GPP NFV reference architecture. To this end, an MOOP was formulated for InPs and MVSOs, aiming at revenue maximization while minimizing SLA violations and ensuring QoS guarantees for subscribers. The solution to the MOOP is obtain in three parts, where the MOOP pricing optimization part was solved using different approaches: NSGA-II algorithm, MORL, and a heuristic process. These approaches yielded maximized variable vectors for the MOOP, represented as Pareto front points. The proposed algorithm (NAC-Rev-Max) has addressed the joint slicing and AC requirements through three sub-algorithms: unit price optimization, LSTM-based traffic prediction, and AC algorithm (Rev-Max). Specifically, NAC-Rev-Max prioritized admission of high-value slices, i.e. eMBB, over slices with lower subscription value, that is URLLC. Additionally, it intelligently allocated dynamic slices based on LSTM traffic prediction information.

Our proposed algorithm outperformed state-of-the-art algorithms (RR and Max-Min fairness approaches) in terms of subscriber satisfaction index, throughput, peak delay, MVSO revenue, and InP revenue. Precisely, in terms of peak revenue, the proposed algorithm out-

performed RR and Max-Min fairness approaches by 3.91% and 18.73%, respectively. In short, our proposed model of integrated service delivery contributes to revolutionizing telecommunications ecosystems by empowering users to seamlessly access advanced services through leveraging satellite infrastructure, thereby enhancing connectivity and expanding network coverage in remote or underserved areas.

Chapter 7

Conclusions and Future Work

This chapter presents the main conclusions of the thesis and suggests potential directions for future research.

7.1 Main conclusions

This thesis investigates challenges in multi-orbital architecture and resource management, presenting proposed solution strategies in response. In Chapter 2, the NTN is designed to incorporate both MEO and GEO orbits, with a focus on their simultaneous use for resource management, specifically DC. The design accounts for orbital differences such as Doppler shift and packet arrival time. Further, a resource allocation algorithm is developed to optimize both delay and capacity. Chapter 3 introduces a UE RF design and includes link budget analysis, along with a resource optimization mechanism known as multi-connectivity, aimed at optimizing capacity. An algorithm is proposed within a multi-layer NTN resource scheduling architecture, which incorporates a software-defined network-layer dispatcher for classifying and differentiating packets based on terminal types, specifically IoT and VSAT terminals.

In Chapter 4, uplink resource management is analyzed with a focus on UE traffic demands across various traffic classes, including eMBB, URLLC, and mMTC. A resource management architecture is proposed for multi-tier NTNs, adapted to the 3GPP 5G protocol stack. Additionally, an energy-efficient service-aware multi-connectivity scheduling algorithm is presented. This algorithm utilizes available radio resources and propagation data to establish a dynamic resource allocation pattern that minimizes UE energy consumption while maximizing QoS. The algorithm employs both optimization and heuristic approaches for resource

allocation. Specifically, in the optimization approach, the interior point method is applied for joint route and power allocation, while path matching for the respective traffic classes is performed using the Hungarian algorithm.

Chapter 5 examines the challenge of managing heterogeneous networks to meet dynamic traffic demands in time-varying environments. This challenge is addressed through dynamic beam and resource allocation techniques, aimed at improving the capacity of multi-tier NTNs over stochastic downlink channels. An iterative algorithm is employed for dynamic beam allocation, while a MADRL-aided resource allocation algorithm is used for joint power and bandwidth allocation. This algorithm establishes resource allocation patterns based on CQI, leveraging multi-connectivity to maximize capacity while operating various waveforms, including 5G NR and DVB-S2X.

Chapter 6 introduces a novel service delivery model in which InPs lease NTN resources as slices to MVSOs, who then offer these resources to subscribers, promoting efficient NTN resource utilization within the telecommunications ecosystem. The model integrates an NTN slicing architecture with multi-layer satellites, including HGS, tailored to the virtualization framework specified by 3GPP. In this context, an algorithm is proposed for joint network slicing and admission control, using techniques such as NSGA-II, MORL, and a heuristic approach. Additionally, the algorithm enhances admission control through an LSTM-based deep learning model that predicts traffic demand for URLLC and eMBB users, thereby preventing SLA violations.

7.2 Future work

The findings presented in this thesis demonstrate the promise of the proposed architecture and resource management strategies for multi-orbital NTN incorporating LEO, MEO, and GEO satellite constellations. Nonetheless, there remain numerous opportunities to broaden its scope. This section explores potential avenues for future research to build upon this work.

- **Artificial Intelligent Driven Resource Management Optimization**: In this thesis, we developed a dynamic time-series prediction model using the LSTM algorithm to predict URLLC and eMBB traffic. Additionally, we designed a robust, intelligent resource allocation system employing multi-agent deep reinforcement learning.

  However, further investigation is needed into the implementation of AI/ML in dynamic

gateway selection, as a multi-orbital NTN constellation will involve numerous gateways. There is also a need to evaluate the impact of AI/ML on both intra- and inter-orbital handovers.

- **Space Inter-Orbital Satellite Link Mesh Design**: This research explored the use of inter-satellite links to enable dynamic beam allocation within NGSO constellations. Further investigation into the design, implementation, and potential advantages of both intra- and inter-orbital satellite links across LEO, MEO, and GEO constellations could be highly valuable for applications such as space-based caching and efficient traffic routing.

- **Interplay of Quantum Communications and Multi-Tier NTN For Secured SDN**: In this thesis, we explored network slicing and virtualization for multi-orbital NTNs. However, network security concerns remain, particularly regarding SDN and resource orchestration across multiple nodes that involve diverse subscribers with varying traffic demands. To ensure secure orchestration, accurate billing, and effective resource dimensioning, quantum communication could be investigated as a viable solution for securing multi-orbital NTNs.

- **Direct-to-Cell in Multi-Tier NTN**: This research evaluated RF design and link budget analysis for various UEs, ranging from IoT devices to VSATs. Further investigation could focus on scenarios involving Direct-to-Cell communication in multi-tier NTNs, with particular emphasis on link budget analysis and channel modeling.

Appendix A

The Hungarian Algorithm with Proof of Matching

This appendix, from literature, is provided for completeness. The Hungarian algorithm is explained for large application of path matching and this approached is followed as in [179]. With a weighted bipartite graph of $G' = \{U', E', W'\}$, a feasible labeling (ℓ) is one that is

$$\ell(u') + \ell(s') \geq W'(u', s') \quad \forall u' \in U', \forall s' \in S' \tag{1}$$

The equality graph with respect to ℓ is $G' = (V, E'_\ell)$, where

$$E'_\ell = (u', s') : \ell(u') + \ell(s') = W'(u', s') \tag{2}$$

If label (ℓ) is possible and M_p is a perfect matching in E_ℓ, it can then be said that M_p is a max-weight matching.

Proof. Defining edge $e \in E$ as $e = (e_u, e_s)$. Let M_p^* be any perfect matching in G. Since u $\in$ V is discovered exactly one time by M_p, it results that

$$w(M_p^*) = \sum_{e \in M_p^*} w(e) \leq \sum_{e \in M_p^*} (\ell(e_u) + (e_s)) = \sum_{v \in V} \ell(v) \tag{3}$$

Hence $\sum_{v \in V} \ell(v)$ is an upper-bound on the cost of any perfect matching. If M_p is the perfect matching in E_ℓ, then

$$w(M_p) = \sum_{e \in M_p} w(e) = \sum_{v \in V} \ell(v) \tag{4}$$

Therefore $w(M_p^*) \leq w(M_p)$ and M_p is optimal. □

Bibliography

[1] M. N. Dazhi, H. Al-Hraishawi, M. R. B. Shankar, and S. Chatzinotas, "Uplink Capacity Optimization for High Throughput Satellites using SDN and Multi-Orbital Dual Connectivity," in *IEEE Int. Conf. Commun. Workshops (ICC Workshops)*, May 2022, pp. 544–549.

[2] M. N. Dazhi, H. Al-Hraishawi, B. Shankar, and S. Chatzinotas, "Terminal-aware multi-connectivity scheduler for uplink multi-layer non-terrestrial networks," in *IEEE Globecom Workshops (GC Wkshps)*, 2022, pp. 1133–1139.

[3] 3GPP TR 38.821 V16.0.0, "3rd Generation Partnership Project; Technical Specification Group Radio Access Network; Solutions for NR to support non-terrestrial networks (NTN) (Release 16)," 3rd Generation Partnership Project, Tech. Rep., 2019.

[4] M. N. Dazhi, H. Al-Hraishawi, M. R. B. Shankar, S. Chatzinotas, and B. Ottersten, "Energy-Efficient Service-Aware Multi-Connectivity Scheduler for Uplink Multi-Layer Non-Terrestrial Networks," *IEEE Transactions on Green Communications and Networking*, vol. 7, no. 3, pp. 1326–1341, Sept 2023.

[5] M. Majamaa, "Toward multi-connectivity in beyond 5g non-terrestrial networks: Challenges and possible solutions," *IEEE Communications Magazine*, pp. 1–7, 2024.

[6] T. Yue, A. Liu, and X. Liang, "Block-Based Kalman Channel Tracking for LEO Satellite Communication With Massive MIMO," *IEEE Communications Letters*, vol. 27, no. 2, pp. 645–649, Feb 2023.

[7] J. Sedin, L. Feltrin, and X. Lin, "Throughput and Capacity Evaluation of 5G New Radio Non-Terrestrial Networks with LEO Satellites," in *IEEE Global Commun. Conf.*, 2020, pp. 1–6.

[8] ETSI TS 136 300, "Evolved universal terrestrial radio access (E–UTRA) and evolved universal terrestrial radio access network (E–UTRAN); Overall description; Stage 2," 3rd Generation Partnership Project (3GPP), Standard, Jun. 2012.

[9] Y. Rui, P. Cheng, M. Li, Q. T. Zhang, and M. Guizani, "Carrier aggregation for LTE-advanced: uplink multiple access and transmission enhancement features," vol. 20, no. 4, pp. 101–108, Aug. 2013.

[10] H. Lee, S. Vahid, and K. Moessner, "A survey of radio resource management for spectrum aggregation in LTE-advanced," vol. 16, no. 2, pp. 745–760, 2014.

[11] M. G. Kibria, E. Lagunas, N. Maturo, H. Al-Hraishawi, and S. Chatzinotas, "Carrier aggregation in satellite communications: Impact and performance study," *IEEE open j. Commun. Soc.*, vol. 1, pp. 1390–1402, 2020.

[12] H. Al-Hraishawi, N. Maturo, E. Lagunas, and S. Chatzinotas, "Scheduling Design and Performance Analysis of Carrier Aggregation in Satellite Communication Systems," vol. 70, no. 8, pp. 7845–7857, Aug. 2021.

[13] H. Al-Hraishawi, E. Lagunas, and S. Chatzinotas, "Traffic simulator for multibeam satellite communication systems," in *2020 10th Advanced Satellite Multimedia Systems Conference and the 16th Signal Processing for Space Communications Workshop (ASMS/SPSC)*, 2020, pp. 1–8.

[14] M. G. Kibria, H. Al-Hraishawi, E. Lagunas, S. Chatzinotas, and B. Ottersten, "Joint beam hopping and carrier aggregation in high throughput multibeam satellite systems," *IEEE Access*, vol. 10, pp. 122 125–122 135, 2022.

[15] F. Rinaldi, A. Raschella, and S. Pizzi, "5G NR system design: A concise survey of key features and capabilities," *Wireless Networks*, vol. 27, no. 8, pp. 5173–5188, 2021.

[16] G. Araniti, A. Iera, S. Pizzi, and F. Rinaldi, "Toward 6G non-terrestrial networks," *IEEE Network*, vol. 36, no. 1, pp. 113–120, 2021.

[17] H. Al-Hraishawi, H. Chougrani, S. Kisseleff, E. Lagunas, and S. Chatzinotas, "A survey on nongeostationary satellite systems: The communication perspective," vol. 25, no. 1, pp. 101–132, Aug. 2023.

[18] Q. Feng, J. Pang, M. Maso, M. Debbah, and W. Tong, "IDFT-VFDM for supplementary uplink and LTE-NR co-existence," vol. 19, no. 5, pp. 3435–3448, 2020.

[19] ITU-R. (2015, Sep) "IMT Vision-Framework and Overall Objectives of the Future Deployment of IMT for 2020 and Beyond". Accessed: 2024-07-28. [Online]. Available: https://www.itu.int/

[20] O. Kodheli, E. Lagunas, N. Maturo, S. K. Sharma, B. Shankar, J. F. M. Montoya, J. C. M. Duncan, D. Spano, S. Chatzinotas, S. Kisseleff, J. Querol, L. Lei, T. X. Vu, and G. Goussetis, "Satellite communications in the new space era: A survey and future challenges," *IEEE Communications Surveys Tutorials*, vol. 23, no. 1, pp. 70–109, 2021.

[21] L. Konstantinos, G. Alexander, S. Ray, S. Detlef, W. Simon, P. Georgia, E. Barry, W. Ning, V. Oriol, T. J. Boris, F. Michael, D. S. Salva, S. K. Pouria, and C. Nicolas, "Use cases and scenarios of 5g integrated satellite-terrestrial networks for enhanced mobile broadband: The sat5g approach," *International Journal of Satellite Communications and Networking*, vol. 37, no. 2, pp. 91–112, May 2018.

[22] Eutelsat Group. "OneWeb and BT sign agreement to explore rural connectivity solutions in the UK and beyond — OneWeb". Accessed: 2024-07-28. [Online]. Available: https://oneweb.net/resources/oneweb-and-bt-sign-agreement-explore-rural-connectivity-solutions-uk-and-beyond

[23] Spire Global. "Orbital Services - Spire: Global Data and Analytics". Accessed: 2024-07-28. [Online]. Available: Spire.https://spire.com/space-services/

[24] SES. "SES Government Solutions Releases New Unified Operational Network — SES". Accessed: 2024-07-28. [Online]. Available: https://www.ses.com/press-release/ses-government-solutions-releases-new-unified-operational-network

[25] GSMA and G. Intelligence. "Understanding 5G: Perspectives on future technological advancements in mobile". Accessed: 2024-07-23. [Online]. Available: https://www.gsma.com/solutions-and-impact/technologies/networks/wp-content/uploads/2015/01/Understanding-5G-Perspectives-on-future-technological-advancements-in-mobile.pdf

[26] Number of internet users worldwide from 2014 to 2029. Accessed: 2024-10-27. [Online]. Available: https://www.statista.com/forecasts/1146844/internet-users-in-the-world

[27] IoT connections outlook. Accessed: 2024-10-27. [Online]. Available: https://www.ericsson.com/en/reports-and-papers/mobility-report/dataforecasts/iot-connections-outlook

[28] Satellite Communications Market Size. Accessed: 2024-10-27. [Online]. Available: https://www.mordorintelligence.com/industry-reports/global-satellite-communication-market

[29] Telesat to Redefine Global Broadband Connectivity with Telesat Lightspeed, the World's Most Advanced Low Earth Orbit (LEO) Satellite Network. Accessed: 2023-10-11. [Online]. Available: https://www.telesat.com/press/press-releases/manufacturer-announcement/

[30] Eutelsat and OneWeb combination heralds new era in space connectivity as world's first GEO-LEO provider. Accessed: 2023-10-11. [Online]. Available: https://oneweb.net/resources/eutelsat-and-oneweb-combination-heralds-new-era-space-connectivity-worlds-first-geo-leo

[31] All Satellites. One Terminal. A New World of Multi-Orbit Services. Accessed: 2024-10-31. [Online]. Available: https://www.all.space/insights/all-satellites-one-terminal-a-new-world-of-multi-orbit-services

[32] G. Geraci, D. López-Pérez, M. Benzaghta, and S. Chatzinotas, "Integrating Terrestrial and Non-Terrestrial Networks: 3D Opportunities and Challenges," *IEEE Communications Magazine*, vol. 61, no. 4, pp. 42–48, Apr. 2023.

[33] Y. Lu, Y. Zhao, F. Sun, and H. Li, "A Survivable Routing Protocol for Two-Layered LEO/MEO Satellite Networks," *Wirel. Netw.*, vol. 20, no. 5, p. 871–887, Jul. 2014.

[34] M. A. Lema, E. Pardo, O. Galinina, S. Andreev, and M. Dohler, "Flexible dual-connectivity spectrum aggregation for decoupled uplink and downlink access in 5G heterogeneous systems," *IEEE J. Sel. Areas Commun.*, vol. 34, no. 11, pp. 2851–2865, 2016.

[35] C. Pupiales, D. Laselva, and I. Demirkol, "Capacity and congestion aware flow control mechanism for efficient traffic aggregation in multi-radio dual connectivity," *IEEE Access*, vol. 9, pp. 114 929–114 944, 2021.

[36] 3rd Generation Partnership Project (3GPP), "Study on small cell enhancements for E-UTRA and E-UTRAN: Higher layer aspects," Standard, Feb. 2014, TR 36.842.

[37] G. S. Park and H. Song, "Video quality-aware traffic offloading system for video streaming services over 5G networks with dual connectivity," vol. 68, no. 6, pp. 5928–5943, 2019.

[38] H. Al-Hraishawi, N. Maturo, E. Lagunas, and S. Chatzinotas, "Scheduling Design and Performance Analysis of Carrier Aggregation in Satellite Communication Systems," pp. 1–14, 2021.

[39] J. Du, C. Jiang, H. Zhang, Y. Ren, and M. Guizani, "Auction design and analysis for SDN-based traffic offloading in hybrid satellite-terrestrial networks," vol. 36, no. 10, pp. 2202–2217, Oct. 2018.

[40] A. J. Roumeliotis, C. I. Kourogiorgas, and A. D. Panagopoulos, "Optimal dynamic capacity allocation for high throughput satellite communications systems," vol. 8, no. 2, pp. 596–599, Apr. 2019.

[41] M. G. Kibria, E. Lagunas, N. Maturo, H. Al-Hraishawi, and S. Chatzinotas, "Carrier aggregation in satellite communications: Impact and performance study," *IEEE Open J. Commun. Soc.*, pp. 1390–1402, 2020.

[42] ETSI TR 102 376-2, "Digital Video Broadcasting (DVB): Implementation guidelines for the second generation system for broadcasting, interactive services, news gathering and other broadband satellite applications;part 2: S2 extensions (DVB-S2X)." European Telecommunications Standards Institute, Standard, 2015.

[43] O. N. C. Yilmaz, O. Teyeb, and A. Orsino, "Overview of LTE-NR dual connectivity," *IEEE Commun. Mag.*, vol. 57, no. 6, pp. 138–144, 2019.

[44] B. Elbert, *The Satellite Communication Ground Segment and Earth Station Handbook*, 2nd ed. Artech House, 2014.

[45] A. Al-Saegh, A. Sali, J. Mandeep, A. Ismail, A. Al-Jumaily, and C. Gomes, *Atmospheric Propagation Model for Satellite Communications.* IntechOpen, 2014, ch. 09, p. 28.

[46] V. Ramaswamy, J. T. Correia, and D. Swain-Walsh, "Modeling and analysis of multi-rat dual connectivity operations in 5g networks," in *2019 IEEE 2nd 5G World Forum (5GWF)*, 2019, pp. 484–489.

[47] H. Al-Hraishawi, N. Maturo, E. Lagunas, and S. Chatzinotas, "Perceptive packet scheduling for carrier aggregation in satellite communication systems," *IEEE Int. Conf on Commun. (ICC)*, pp. 1–6, Jun. 2020.

[48] L. Bertaux, S. Medjiah, P. Berthou, S. Abdellatif, A. Hakiri, P. Gelard, F. Planchou, and M. Bruyere, "Software defined networking and virtualization for broadband satellite networks," vol. 53, no. 3, pp. 54–60, Mar. 2015.

[49] H. Al-Hraishawi, H. Chougrani, S. Kisseleff, E. Lagunas, and S. Chatzinotas, "A Survey on Nongeostationary Satellite Systems: The Communication Perspective," vol. 25, no. 1, pp. 101–132, Aug. 2023.

[50] H. Al-Hraishawi, M. Minardi, H. Chougrani, O. Kodheli, J. F. M. Montoya, and S. Chatzinotas, "Multi-layer space information networks: Access design and softwarization," *IEEE Access*, 2021.

[51] T. Colin, T. Delamotte, and A. Knopp, "Filter Distortions in Ultra High-Throughput Satellites: Models, Parameters and Multicarrier Optimization," vol. 70, pp. 292–306, Dec. 2022.

[52] 3rd Generation Partnership Project (3GPP), "Technical Specification Group Radio Access Network; Study on New Radio (NR) to support non-terrestrial networks (Release 15)," Standard, Jun. 2019, TR 38.811.

[53] 3rd Generation Partnership Project (3GPP), "Evolved Universal Terrestrial Radio Access (E-UTRA) and NR; Multi-Connectivity; Stage 2," Standard, Sep. 2019, TS 37.340.

[54] H. Cui, J. Zhang, Y. Geng, Z. Xiao, T. Sun, N. Zhang, J. Liu, Q. Wu, and X. Cao, "Space-air-ground integrated network (SAGIN) for 6G: Requirements, architecture and challenges," vol. 19, no. 2, pp. 90–108, Feb. 2022.

[55] V. F. Monteiro, D. A. Sousa, T. F. Maciel, F. R. P. Cavalcanti, C. F. M. e. Silva, and E. B. Rodrigues, "Distributed RRM for 5G Multi-RAT Multiconnectivity Networks," vol. 13, no. 1, pp. 192–203, Mar. 2019.

[56] R. P. Antonioli, J. Pettersson, and T. F. Maciel, "Split Responsibility Scheduler for Multi-Connectivity in 5G Cellular Networks," vol. 34, no. 6, pp. 212–219, Nov. 2020.

[57] H. Al-Hraishawi, E. Lagunas, and S. Chatzinotas, "Traffic Simulator for Multibeam Satellite Communication Systems," in *10th Advanced Satellite Multimedia Syst. Conf. and the 16th Signal Process. for Space Commun. Workshop (ASMS/SPSC)*, Oct. 2020, pp. 1–8.

[58] A. Mahbas, H. Zhu, and J. Wang, "Trio-Connectivity for Efficient Uplink Performance in Future Mobile HetNets," vol. 69, no. 12, pp. 15 706–15 719, Dec. 2020.

[59] Z. Li, Y. Wang, M. Liu, R. Sun, Y. Chen, J. Yuan, and J. Li, "Energy Efficient Resource Allocation for UAV-Assisted Space-Air-Ground Internet of Remote Things Networks," *IEEE Access*, vol. 7, pp. 145 348–145 362, Oct. 2019.

[60] J. Zhang, B. Yu, C. Tang, Y. Zhang, L. Zhang, and S. Lu, "Joint Optimization of Energy Efficiency and Spectrum Efficiency of Single-station Multi-satellite MIMO Uplink System," in *IEEE Int. Conf. Signal Process., Commun. Comput. (ICSPCC)*, Aug. 2021, pp. 1–6.

[61] B. Zhao, G. Ren, X. Dong, and H. Zhang, "Spatial Group Based Optimal Uplink Power Control for Random Access in Satellite Networks," vol. 69, no. 7, pp. 7354–7365, Jul. 2020.

[62] S. Shi, G. Li, K. An, Z. Li, and G. Zheng, "Optimal Power Control for Real-Time Applications in Cognitive Satellite Terrestrial Networks," vol. 21, no. 8, pp. 1815–1818, Aug. 2017.

[63] ALL.SPACE, "ALL.SPACE's first-of-its-kind terminal completes simultaneous, full performance, multi-link trials across all orbits — ALL.SPACE." (Accessed: Sep. 15, 2022). [Online]. Available: œhttps://all.space/insights/isotropic-systems-first-of-its-kind-terminal-completes-simultaneous-full-performance-multi-link-tri

[64] U. J. Lewark, J. Antes, J. Walheim, J. Timmermann, T. Zwick, and I. Kallfass, "Link budget analysis for future E-band gigabit satellite communication links (71-76 and 81-84 Ghz)," *CEAS Space Journal*, vol. 4, no. 1-4, pp. 41–46, 2013.

[65] Y. Lee and J. P. Choi, "Performance evaluation of high-frequency mobile satellite communications," *IEEE Access*, vol. 7, pp. 49 077–49 087, 2019.

[66] L. Kleinrock, *Queueing Systems - Volume I: Theory.* USA: Wiley-Interscience, Jan. 1975.

[67] V. Gupta, M. Harchol Balter, K. Sigman, and W. Whitt, "Analysis of join-the-shortest-queue routing for web server farms," *Performance Evaluation*, vol. 64, no. 9, pp. 1062–1081, Oct. 2007.

[68] 3rd Generation Partnership Project (3GPP), "Technical Specification Group Radio Access Network; Solutions for NR to support non-terrestrial networks (NTN) (Release 16)," Standard, Jun. 2019, TR 38.821.

[69] F. Liu, K. Zheng, W. Xiang, and H. Zhao, "Design and Performance Analysis of An Energy-Efficient Uplink Carrier Aggregation Scheme," vol. 32, no. 2, pp. 197–207, Feb. 2014.

[70] M. Hosseinian, J. P. Choi, S.-H. Chang, and J. Lee, "Review of 5G NTN Standards Development and Technical Challenges for Satellite Integration With the 5G Network," vol. 36, no. 8, pp. 22–31, Aug. 2021.

[71] ETSI TR 103 352, "Satellite Earth Stations and Systems (SES); Energy efficiency of satellite broadband network." European Telecommunications Standards Institute, Standard, Jun. 2016.

[72] Z. Zhang, W. Zhang, and F.-H. Tseng, "Satellite Mobile Edge Computing: Improving QoS of High-Speed Satellite-Terrestrial Networks Using Edge Computing Techniques," vol. 33, no. 1, pp. 70–76, Jan. 2019.

[73] F. Heliot and R. Tafazolli, "Optimal Energy-Efficient Source and Relay Precoder Design for Two-Way MIMO-AF Relay Systems," *IEEE Trans. Green Commun. Netw.*, vol. 4, no. 3, pp. 759–773, Sep. 2020.

[74] H. Al-Hraishawi, S. Chatzinotas, and B. Ottersten, "Broadband Non-Geostationary Satellite Communication Systems: Research Challenges and Key Opportunities," in *IEEE Int. Conf. Commun. Workshops (ICC Workshops)*, Jun. 2021, pp. 1–6.

[75] D. Wang, M. Giordani, M.-S. Alouini, and M. Zorzi, "The potential of multilayered hierarchical nonterrestrial networks for 6G: A comparative analysis among networking architectures," vol. 16, no. 3, pp. 99–107, Jul. 2021.

[76] G. S. Kesava and N. B. Mehta, "Multi-Connectivity for URLLC and Coexistence with eMBB in Time-Varying and Frequency-Selective Fading Channels," pp. 1–14, Nov. 2022.

[77] I. Leyva-Mayorga, R. Torre, V. Pla, S. Pandi, G. T. Nguyen, J. Martinez-Bauset, and F. H. P. Fitzek, "Network-Coded Cooperation and Multi-Connectivity for Massive Content Delivery," *IEEE Access*, vol. 8, pp. 15 656–15 672, Jan. 2020.

[78] J. Ostrometzky, G. Rafalovich, B. Kagan, and H. Messer, "Stand-Alone, Affordable IoT Satellite Terminals and Their Opportunistic Use for Rain Monitoring," *IEEE Internet of Things Magazine*, vol. 5, no. 4, pp. 100–105, Dec. 2022.

[79] A. Guterres, "Carbon neutrality by 2050: the world's most urgent mission," Dec. 2020, (accessed Mar.1, 2023). [Online]. Available: "https://www.un.org/sg/en/content/sg/articles/2020-12-11/carbon-neutrality-2050-the-world's-most-urgent-mission"

[80] M. N. Dazhi, H. Al-Hraishawi, B. Shankar, and S. Chatzinotas, "Terminal-Aware Multi-Connectivity Scheduler for Uplink Multi-Layer Non-Terrestrial Networks," in *2022 IEEE Globecom Workshops*, Dec. 2022, pp. 1133–1139.

[81] 3rd Generation Partnership Project (3GPP), "TS 138 300 - V17.0.0 - 5G; NR and NG-RAN Overall description; Stage-2 (3GPP TS 38.300 version 17.0.0 Release 17)," May 2022, TS 138 300 .

[82] GSMA, "Energy Efficiency: An Overview," May 2019, (accessed Feb.28, 2023). [Online]. Available: "https://www.gsma.com/futurenetworks/wiki/energy-efficiency-2/"

[83] ITU-R, "Recommendation ITU-R P.676-13 Attenuation by atmospheric gases and related effects P Series Radiowave propagation," vol. 13, Aug. 2022.

[84] ITU-R, "Recommendation ITU-R P.618-13 Propagation data and prediction methods required for the design of Earth-space telecommunication systems P Series Radiowave propagation," vol. 13, Dec. 2017.

[85] A. Guidotti, A. Vanelli-Coralli, A. Mengali, and S. Cioni, "Non-Terrestrial Networks: Link Budget Analysis," in *IEEE Int. Conf. Commun. (ICC)*, Jun. 2020, pp. 1–7.

[86] L. You, K.-X. Li, J. Wang, X. Gao, X.-G. Xia, and B. Ottersten, "Massive MIMO Transmission for LEO Satellite Communications," vol. 38, no. 8, pp. 1851–1865, Aug. 2020.

[87] B. Clerckx and O. Claude, *MIMO wireless networks : channels, techniques and standards for multi-antenna, multi-user and multi-cell systems*, 2nd ed. Oxford [U.K.]: Academic Press, Feb. 2013.

[88] M. Chen, R. Chai, and Q. Chen, "Joint Route Selection and Resource Allocation Algorithm for Data Relay Satellite Systems Based on Energy Efficiency Optimization," in *11th Int. Conf. Wireless Commun. and Signal Process. (WCSP)*, Oct. 2019, pp. 1–6.

[89] W. Yan, F. Liu, C. Chung, and K. Wong, "A hybrid genetic algorithm-interior point method for optimal reactive power flow," vol. 21, no. 3, pp. 1163–1169, Aug. 2006.

[90] N. Ploskas and N. Samaras, *Linear Programming Using MATLAB®*. Springer International Publishing, Oct. 2017.

[91] MathWorks, "Constrained Nonlinear Optimization Algorithms," 2016, (Accessed: Oct. 23, 2022). [Online]. Available: "https://nl.mathworks.com/help/optim/ug/constrained-nonlinear-optimization-algorithms.html"

[92] R. H. Byrd, J. C. Gilbert, and J. Nocedal, "A trust region method based on interior point techniques for nonlinear programming," *Mathematical Programming*, vol. 89, pp. 149–185, Nov. 2000.

[93] R. H. Byrd, M. E. Hribar, and J. Nocedal, "An Interior Point Algorithm for Large-Scale Nonlinear Programming," *SIAM Journal on Optimization*, vol. 9, no. 4, pp. 877–900, Apr. 1999.

[94] R. Waltz, J. Morales, J. Nocedal, and D. Orban, "An interior algorithm for nonlinear optimization that combines line search and trust region steps," *Mathematical Programming*, vol. 107, no. 3, pp. 1436–4646, Jul. 2006.

[95] S. Boyd and L. Vandenberghe, *Convex Optimization*. Cambridge, UK: Cambridge Univ. Press, 2004.

[96] G. H. Golub and C. V. Loan, "Matrix Computations, Third Edition." Johns Hopkins University Press, Oct. 1996.

[97] R. Almesaeed, A. S. Ameen, E. Mellios, A. Doufexi, and A. R. Nix, "A proposed 3D extension to the 3GPP/ITU channel model for 800 MHz and 2.6 GHz bands," in *The 8th Eur. Conf. Antennas and Propag. (EuCAP 2014)*, Apr. 2014, pp. 3039–3043.

[98] 3rd Generation Partnership Project (3GPP), "TS 138 101-1- V15.2.0 - 5G; NR; User Equipment (UE) radio transmission and reception; Part 1: Range 1 Standalone (3GPP TS 38.101-1 version 15.2.0 Release 15)," Jul. 2018, TS 138 101 .

[99] A. Kyrgiazos, B. Evans, P. Thompson, P. T. Mathiopoulos, and S. Papaharalabos, "A terabit/second satellite system for European broadband access: a feasibility study," *Int. J. of Satellite Commun. and Netw.*, vol. 32, no. 2, pp. 63–92, Jan. 2014.

[100] N. Chakraborty, J. Peng, S. Akella, and J. E. Mitchell, "Proximity Queries Between Convex Objects: An Interior Point Approach for Implicit Surfaces," vol. 24, no. 1, pp. 211–220, Feb. 2008.

[101] M. E. Ghami, I. D. Ivanov, C. Roos, and T. Steihaug, "A polynomial-time algorithm for LO based on generalized logarithmic barrier functions," *Int. J. Appl. Math.*, vol. 21, p. 99–115, Jan. 2008.

[102] Y.-J. Choi and S. Bahk, "Multichannel wireless scheduling under limited terminal capability," vol. 7, no. 2, pp. 611–617, Feb. 2008.

[103] S. Mahboob and L. Liu, "Revolutionizing future connectivity: A contemporary survey on AI-empowered satellite-based non-terrestrial networks in 6G," vol. 26, no. 2, pp. 1279–1321, 2024.

[104] M. N. Dazhi, H. Al-Hraishawi, M. B. Shankar, S. Chatzinotas, and J. Grotz, "Joint NTN Slicing and Admission Control for Infrastructure-as-a-Service: A Deep Learning Aided Multi-objective Optimization," *IEEE Transactions on Cognitive Communications and Networking*, pp. 1–16, Sep. 2024.

[105] Z. Xiao, Z. Han, A. Nallanathan, O. A. Dobre, B. Clerckx, J. Choi, C. He, and W. Tong, "Antenna array enabled space/air/ground communications and networking for 6G," vol. 40, no. 10, pp. 2773–2804, 2022.

[106] D. Zhou, M. Sheng, Y. Wang, J. Li, and Z. Han, "Machine learning-based resource allocation in satellite networks supporting internet of remote things," *IEEE Transactions on Wireless Communications*, vol. 20, no. 10, pp. 6606–6621, 2021.

[107] E. Zedini, A. Kammoun, and M.-S. Alouini, "Performance of Multibeam Very High Throughput Satellite Systems Based on FSO Feeder Links With HPA Nonlinearity," *IEEE Transactions on Wireless Communications*, vol. 19, no. 9, pp. 5908–5923, Sep. 2020.

[108] Y. Kawamoto, T. Kamei, M. Takahashi, N. Kato, A. Miura, and M. Toyoshima, "Flexible resource allocation with inter-beam interference in satellite communication systems with a digital channelizer," *IEEE Transactions on Wireless Communications*, vol. 19, no. 5, pp. 2934–2945, 2020.

[109] M. Takahashi, Y. Kawamoto, N. Kato, A. Miura, and M. Toyoshima, "DBF-Based Fusion Control of Transmit Power and Beam Directivity for Flexible Resource Allocation in HTS Communication System Toward B5G," *IEEE Transactions on Wireless Communications*, vol. 21, no. 1, pp. 95–105, Jan. 2022.

[110] B. Zhao, X. Dong, G. Ren, and J. Liu, "Optimal User Pairing and Power Allocation in 5G Satellite Random Access Networks," *IEEE Transactions on Wireless Communications*, vol. 21, no. 6, pp. 4085–4097, Jun. 2022.

[111] Z. Lin, Z. Ni, L. Kuang, C. Jiang, and Z. Huang, "Satellite-Terrestrial Coordinated Multi-Satellite Beam Hopping Scheduling Based on Multi-Agent Deep Reinforcement Learning," *IEEE Transactions on Wireless Communications*, vol. 23, no. 8, pp. 10 091–10 103, Aug. 2024.

[112] M. N. Dazhi, H. Al-Hraishawi, B. Shankar, and S. Chatzinotas, "Terminal-Aware Multi-Connectivity Scheduler for Uplink Multi-Layer Non-Terrestrial Networks," in *IEEE Globecom Workshops (GC Wkshps)*, Dec. 2022, pp. 1133–1139.

[113] E. T. Michailidis, P. Theofilakos, and A. G. Kanatas, "Three-Dimensional Modeling and Simulation of MIMO Mobile-to-Mobile via Stratospheric Relay Fading Channels," *IEEE Transactions on Vehicular Technology*, vol. 62, no. 5, pp. 2014–2030, Jun 2013.

[114] M. Takahashi, Y. Kawamoto, N. Kato, A. Miura, and M. Toyoshima, "Adaptive Power Resource Allocation With Multi-Beam Directivity Control in High-Throughput Satellite Communication Systems," *IEEE Wireless Communications Letters*, vol. 8, no. 4, pp. 1248–1251, Aug 2019.

[115] G. Maral, M. Bousquet, and Z. Sun, *Satellite Communications System: Systems Techniques and Technology.* New York, NY, USA: Wiley, Aug. 2011.

[116] J. Choi and V. Chan, "Optimum power and beam allocation based on traffic demands and channel conditions over satellite downlinks," *IEEE Transactions on Wireless Communications*, vol. 4, no. 6, pp. 2983–2993, Nov 2005.

[117] N. Okati, T. Riihonen, D. Korpi, I. Angervuori, and R. Wichman, "Downlink coverage and rate analysis of low earth orbit satellite constellations using stochastic geometry," *IEEE Transactions on Communications*, vol. 68, no. 8, pp. 5120–5134, Aug 2020.

[118] European Telecommunications Standards Institute (ETSI), "Digital Video Broadcasting (DVB): Second generation framing structure, channel coding and modulation systems for broadcasting, interactive services, news gathering and other broadband satellite applications; part 2: DVB-S2X." Standard, Aug 2020, EN 302 307-2.

[119] 3rd Generation Partnership Project (3GPP), "5G NR; Physical layer procedures for data (version 16.2.0 Release 16)," Standard, Jul. 2020, TS 38.214.

[120] D.-D. Tran, S. K. Sharma, V. N. Ha, S. Chatzinotas, and I. Woungang, "Multi-agent drl approach for energy-efficient resource allocation in urllc-enabled grant-free noma systems," *IEEE Open Journal of the Communications Society*, vol. 4, pp. 1470–1486, Jul. 2023.

[121] N. Zhao, Y.-C. Liang, D. Niyato, Y. Pei, M. Wu, and Y. Jiang, "Deep Reinforcement Learning for User Association and Resource Allocation in Heterogeneous Cellular Networks," *IEEE Transactions on Wireless Communications*, vol. 18, no. 11, pp. 5141–5152, Nov. 2019.

[122] H. v. Hasselt, A. Guez, and D. Silver, "Deep reinforcement learning with double q-learning," in *Proceedings of the Thirtieth AAAI Conference on Artificial Intelligence*, ser. AAAI'16. AAAI Press, Feb. 2016, p. 2094–2100.

[123] K. Tan, D. Bremner, J. Le Kernec, Y. Sambo, L. Zhang, and M. A. Imran, "Intelligent Handover Algorithm for Vehicle-to-Network Communications With Double-Deep Q-Learning," *IEEE Transactions on Vehicular Technology*, vol. 71, no. 7, pp. 7848–7862, Jul 2022.

[124] Z. Lin, Z. Ni, L. Kuang, C. Jiang, and Z. Huang, "Dynamic Beam Pattern and Bandwidth Allocation Based on Multi-Agent Deep Reinforcement Learning for Beam Hopping Satellite Systems," *IEEE Transactions on Vehicular Technology*, vol. 71, no. 4, pp. 3917–3930, Apr 2022.

[125] Z. Wang, R. M. Gower, C. Zhang, S. Lyu, Y. Xia, and Y. Huang, "A Statistical Linear Precoding Scheme Based on Random Iterative Method for Massive MIMO Systems," *IEEE Transactions on Wireless Communications*, vol. 21, no. 12, pp. 10 115–10 129, Dec 2022.

[126] G. Yang, J. Sang, X. Zhang, X. He, Y. Liu, and F. Sun, "Sensing Data Aggregation in Mobile Crowd Sensing: A Cloud-Enhanced-Edge-End Framework With DQN-Based Offloading," *IEEE Internet of Things Journal*, pp. 1–1, Jul. 2024.

[127] M. Zhang, Y. Guo, L. Salaün, C. W. Sung, and C. S. Chen, "Proportional Fair Scheduling for Downlink mmWave Multi-User MISO-NOMA Systems," *IEEE Transactions on Vehicular Technology*, vol. 71, no. 6, pp. 6308–6321, Jun. 2022.

[128] T. Zhu, X. Qin, L. Chen, X. Chen, and G. Wei, "wBBR: A Bottleneck Estimation-Based Congestion Control for Multipath TCP," in *2018 IEEE 88th Vehicular Technology Conference (VTC-Fall)*, Aug. 2018, pp. 1–5.

[129] D. Mishra, N. R. Zema, and E. Natalizio, "A High-End IoT Devices Framework to Foster Beyond-Connectivity Capabilities in 5G/B5G Architecture," *IEEE Communications Magazine*, vol. 59, no. 1, pp. 55–61, Jan. 2021.

[130] M. Dazhi, H. Al-Hraishawi, M. R. B. Shankar, and S. Chatzinotas, "Uplink capacity optimization for high throughput satellites using SDN and multi-orbital dual connec-

tivity," in *2022 IEEE International Conference on Communications Workshops (ICC Workshops)*, Jul. 2022, pp. 544–549.

[131] T. A. Khan, X. Lin, S. E. Löwenmark, O. Liberg, S. Euler, J. Sedin, E. A. Yavuz, H. Shokri-Razaghi, and H.-L. Määttänen, "The Internet of Things from Space: Transforming LTE Machine Type Communications for Non-Terrestrial Networks," *IEEE Communications Standards Magazine*, vol. 6, no. 2, pp. 57–63, Jun. 2022.

[132] R. Liu, K. Guo, X. Li, K. Dev, S. A. Khowaja, T. A. Tsiftsis, and H. Song, "RIS-Empowered Satellite-Aerial-Terrestrial Networks With PD-NOMA," *IEEE Communications Surveys & Tutorials*, pp. 1–1, Apr. 2024.

[133] V. Sciancalepore, X. Costa-Perez, and A. Banchs, "RL-NSB: Reinforcement Learning-Based 5G Network Slice Broker," *IEEE/ACM Transactions on Networking*, vol. 27, no. 4, pp. 1543–1557, Aug. 2019.

[134] B. Han, A. DeDomenico, G. Dandachi, A. Drosou, D. Tzovaras, R. Querio, F. Moggio, O. Bulakci, and H. D. Schotten, "Admission and Congestion Control for 5G Network Slicing," in *2018 IEEE Conference on Standards for Communications and Networking (CSCN)*, Dec. 2018, pp. 1–6.

[135] D. Bega, M. Gramaglia, A. Banchs, V. Sciancalepore, K. Samdanis, and X. Costa-Perez, "Optimising 5G infrastructure markets: The business of network slicing," in *IEEE INFOCOM 2017 - IEEE Conference on Computer Communications*, Oct. 2017, pp. 1–9.

[136] J. X. Salvat, L. Zanzi, A. Garcia-Saavedra, V. Sciancalepore, and X. Costa-Perez, "Overbooking Network Slices through Yield-Driven End-to-End Orchestration," ser. CoNEXT '18. Association for Computing Machinery, Dec. 2018, p. 353–365.

[137] M. R. Raza, C. Natalino, P. Öhlen, L. Wosinska, and P. Monti, "Reinforcement Learning for Slicing in a 5G Flexible RAN," *Journal of Lightwave Technology*, vol. 37, no. 20, pp. 5161–5169, Oct. 2019.

[138] G. O. Boateng, D. Ayepah-Mensah, D. M. Doe, A. Mohammed, G. Sun, and G. Liu, "Blockchain-Enabled Resource Trading and Deep Reinforcement Learning-Based Au-

tonomous RAN Slicing in 5G," *IEEE Transactions on Network and Service Management*, vol. 19, no. 1, pp. 216–227, Mar. 2022.

[139] G. O. Boateng, G. Sun, D. A. Mensah, D. M. Doe, R. Ou, and G. Liu, "Consortium Blockchain-Based Spectrum Trading for Network Slicing in 5G RAN: A Multi-Agent Deep Reinforcement Learning Approach," *IEEE Transactions on Mobile Computing*, vol. 22, no. 10, pp. 5801–5815, Oct. 2023.

[140] G. Dandachi, A. De Domenico, D. T. Hoang, and D. Niyato, "An Artificial Intelligence Framework for Slice Deployment and Orchestration in 5G Networks," *IEEE Transactions on Cognitive Communications and Networking*, vol. 6, no. 2, pp. 858–871, Jun. 2020.

[141] T. V. K. Buyakar, H. Agarwal, B. R. Tamma, and A. A. Franklin, "Resource Allocation with Admission Control for GBR and Delay QoS in 5G Network Slices," in *2020 International Conference on COMmunication Systems & NETworkS (COMSNETS)*, Mar. 2020, pp. 213–220.

[142] S. Saxena and K. M. Sivalingam, "Slice admission control using overbooking for enhancing provider revenue in 5g networks," in *NOMS 2022-2022 IEEE/IFIP Network Operations and Management Symposium*, Jun. 2022, pp. 1–7.

[143] M. Sulaiman, A. Moayyedi, M. Ahmadi, M. A. Salahuddin, R. Boutaba, and A. Saleh, "Coordinated slicing and admission control using multi-agent deep reinforcement learning," *IEEE Transactions on Network and Service Management*, pp. 1–1, Nov. 2022.

[144] H. Wu, J. Chen, C. Zhou, J. Li, and X. Shen, "Learning-Based Joint Resource Slicing and Scheduling in Space-Terrestrial Integrated Vehicular Networks," *Journal of Communications and Information Networks*, vol. 6, no. 3, pp. 208–223, Sep. 2021.

[145] Y. Bai, C. Liang, and Q. Chen, "Network Slice Admission Control and Resource Allocation in LEO Satellite Networks: A Robust Optimization Approach," in *2022 27th Asia Pacific Conference on Communications (APCC)*, Nov. 2022, pp. 1–6.

[146] Why Government Networks Need Multi-Orbit SATCOM — SES. (Accessed: Jun. 6, 2024). [Online]. Available: https://www.ses.com/blog/why-government-networks-need-multi-orbit-satcom

[147] Eutelsat and OneWeb combination heralds new era in space connectivity as world's first GEO-LEO operator. (Accessed: Jun. 6, 2024). [Online]. Available: https://oneweb.net/resources/eutelsat-and-oneweb-combination-heralds-new-era-space-connectivity-worlds-first-geo-leo

[148] J. Li, S. Zhang, X. Liu, and R. He, "Multi-objective evolutionary optimization for geostationary orbit satellite mission planning," *Journal of Systems Engineering and Electronics*, vol. 28, no. 5, pp. 934–945, Oct. 2017.

[149] X. Hu, Y. Zhang, X. Liao, Z. Liu, W. Wang, and F. M. Ghannouchi, "Dynamic Beam Hopping Method Based on Multi-Objective Deep Reinforcement Learning for Next Generation Satellite Broadband Systems," *IEEE Transactions on Broadcasting*, vol. 66, no. 3, pp. 630–646, Sep. 2020.

[150] M. N. Dazhi, H. Al-Hraishawi, B. Shankar, and S. Chatzinotas, "Terminal-Aware Multi-Connectivity Scheduler for Uplink Multi-Layer Non-Terrestrial Networks," in *IEEE Globecom Workshops*, Dec. 2022, pp. 1133–1139.

[151] European Telecommunications Standards Institute, "Network Functions Virtualisation (NFV); Architectural Framework." Standard, Dec. 2014, ETSI GS NFV 002.

[152] S. Hochreiter and J. Schmidhuber, "Long Short-Term Memory," *Neural Computation*, vol. 9, no. 8, pp. 1735–1780, Nov. 1997.

[153] F. A. Gers, J. Schmidhuber, and F. Cummins, "Learning to Forget: Continual Prediction with LSTM," *Neural Computation*, vol. 12, no. 10, pp. 2451–2471, Oct. 2000.

[154] A. K. Gizzini and M. Chafii, "A Survey on Deep Learning Based Channel Estimation in Doubly Dispersive Environments," *IEEE Access*, vol. 10, pp. 70 595–70 619, Jul. 2022.

[155] J. Ma, H. Liu, C. Peng, and T. Qiu, "Unauthorized Broadcasting Identification: A Deep LSTM Recurrent Learning Approach," *IEEE Transactions on Instrumentation and Measurement*, vol. 69, no. 9, pp. 5981–5983, Jul. 2020.

[156] S. Wen, Y. Wang, Y. Tang, Y. Xu, P. Li, and T. Zhao, "Real-Time Identification of Power Fluctuations Based on LSTM Recurrent Neural Network: A Case Study on Singapore Power System," *IEEE Transactions on Industrial Informatics*, vol. 15, no. 9, pp. 5266–5275, Sep. 2019.

[157] B. Lindemann, T. Müller, H. Vietz, N. Jazdi, and M. Weyrich, "A survey on long short-term memory networks for time series prediction," *Procedia CIRP*, vol. 99, pp. 650–655, May 2021.

[158] A. K. Gizzini, M. Chafii, S. Ehsanfar, and R. M. Shubair, "Temporal Averaging LSTM-based Channel Estimation Scheme for IEEE 802.11p Standard," in *2021 IEEE Global Communications Conference (GLOBECOM)*, Dec. 2021, pp. 01–07.

[159] X. Ding, L. Feng, Y. Zou, and G. Zhang, "Deep Learning Aided Spectrum Prediction for Satellite Communication Systems," *IEEE Transactions on Vehicular Technology*, vol. 69, no. 12, pp. 16 314–16 319, Dec. 2020.

[160] European Telecommunications Standards Institute, "5G; Service requirements for Video, Imaging and Audio for Professional Applications (VIAPA) (3GPP TS 22.263 version 17.4.0 Release 17)," Standard, May 2022, ETSI TS 122 263.

[161] H. Alves, G.-D. Jo, J. Shin, C. I. Yeh, N. H. Mahmood, C. M. de Lima, C. Yoon, N. Rajatheva, O.-S. Park, S.-K. Kim, E. Kim, V. Niemel, H. W. Lee, A. Pouttu, H. K. Chung, and M. Latva-aho, "Beyond 5G URLLC evolution: New service modes and practical considerations," *ITU Journal on Future and Evolving Technologies*, vol. 3, pp. 545–554, Oct. 2022.

[162] SES, "Viasat 2.4m — SES," (Accessed: Jul. 5, 2023). [Online]. Available: https://www.ses.com/o3b-mpower/o3b-mpower-technology/viasat-24m

[163] SES, "Enterprise via SES-17," (Accessed: Jul. 5, 2023). [Online]. Available: https://www.ses.com/sites/default/files/2023-02/SES-SB-Enterprise-SES-17.pdf

[164] Z. Li, H. Zhang, C. Liu, X. Li, H. Ji, and V. C. M. Leung, "Online Service Deployment on Mega-LEO Satellite Constellations for End-to-End Delay Optimization," *IEEE Transactions on Network Science and Engineering*, vol. 11, no. 1, pp. 1214–1226, Jan. 2024.

[165] R. Deng, B. Di, S. Chen, S. Sun, and L. Song, "Ultra-Dense LEO Satellite Offloading for Terrestrial Networks: How Much to Pay the Satellite Operator," *IEEE Transactions on Wireless Communications*, vol. 19, no. 10, pp. 6240–6254, Oct. 2020.

[166] Z. Fei, B. Li, S. Yang, C. Xing, H. Chen, and L. Hanzo, "A Survey of Multi-Objective Optimization in Wireless Sensor Networks: Metrics, Algorithms, and Open Problems," *IEEE Communications Surveys & Tutorials*, vol. 19, no. 1, pp. 550–586, Feb. 2017.

[167] K. Deb, A. Pratap, S. Agarwal, and T. Meyarivan, "A fast and elitist multiobjective genetic algorithm: NSGA-II," *IEEE Transactions on Evolutionary Computation*, vol. 6, no. 2, pp. 182–197, Apr. 2002.

[168] MathWorks, "gamultiobj Algorithm - MATLAB & Simulink - MathWorks ," (Accessed: Sep. 2, 2023). [Online]. Available: https://nl.mathworks.com/help/gads/gamultiobj-algorithm.html

[169] MathWorks, "Genetic Algorithm Terminology - MATLAB & Simulink - MathWorks," (Accessed: Sep. 4, 2023). [Online]. Available: https://nl.mathworks.com/help/gads/some-genetic-algorithm-terminology.html

[170] P. V. R. Ferreira, R. Paffenroth, A. M. Wyglinski, T. M. Hackett, S. G. Bilén, R. C. Reinhart, and D. J. Mortensen, "Multiobjective Reinforcement Learning for Cognitive Satellite Communications Using Deep Neural Network Ensembles," *IEEE Journal on Selected Areas in Communications*, vol. 36, no. 5, pp. 1030–1041, May 2018.

[171] J. Liu, Z. Shi, S. Zhang, and N. Kato, "Distributed Q-Learning Aided Uplink Grant-Free NOMA for Massive Machine-Type Communications," *IEEE Journal on Selected Areas in Communications*, vol. 39, no. 7, pp. 2029–2041, Jul. 2021.

[172] F. Pasquevich, A. F. Ramirez, J. M. Ayarde, and G. C. Briones, "Adaptive Modulation Using Multi-Objective Reinforcement Learning for LEO Satellites," in *2021 IEEE Cognitive Communications for Aerospace Applications Workshop (CCAAW)*, Sep. 2021, pp. 1–6.

[173] D. Tran, S. K. Sharma, S. Chatzinotas, and I. Woungang, "Learning-Based Multiplexing of Grant-Based and Grant-Free Heterogeneous Services with Short Packets," in *2021 IEEE Global Communications Conference (GLOBECOM)*, Dec. 2021, pp. 01–06.

[174] B. Kruekaew and W. Kimpan, "Multi-Objective Task Scheduling Optimization for Load Balancing in Cloud Computing Environment Using Hybrid Artificial Bee Colony Al-

gorithm With Reinforcement Learning," *IEEE Access*, vol. 10, pp. 17 803–17 818, Feb. 2022.

[175] K. Li, X. Wang, Q. He, M. Yang, M. Huang, and S. Dustdar, "Task Computation Offloading for Multi-Access Edge Computing via Attention Communication Deep Reinforcement Learning," *IEEE Transactions on Services Computing*, vol. 16, no. 4, pp. 2985–2999, Jul. 2023.

[176] M. Monemi, M. Rasti, and E. Hossain, "Low-Complexity SINR Feasibility Checking and Joint Power and Admission Control in Prioritized Multitier Cellular Networks," *IEEE Transactions on Wireless Communications*, vol. 15, no. 3, pp. 2421–2434, Mar. 2016.

[177] F. Conceição, C. H. Antunes, M. Gomes, V. Silva, and R. Dinis, "Max-Min Fairness Optimization in Uplink Cell-Free Massive MIMO Using Meta-Heuristics," *IEEE Transactions on Communications*, vol. 70, no. 3, pp. 1792–1807, Mar. 2022.

[178] J. Song, Z. Wang, Y. Niu, X. Yi, and Q.-L. Han, "Co-Design of Dissipative Deconvolution Filter and Round-Robin Protocol for Networked 2-D Digital Systems: Optimization and Application," *IEEE Transactions on Systems, Man, and Cybernetics: Systems*, vol. 53, no. 10, pp. 6316–6328, Oct. 2023.

[179] H. W. Kuhn, "The Hungarian method for the assignment problem," *Naval Research Logistics (NRL)*, vol. 52, pp. 7–21, Feb. 2005.